Nanocharacterisation of III-Nitride Semiconductors

A thesis presented for the degree of
Doctor of Philosophy

Written By

Douglas Cameron

Physics Department
University of Strathclyde
Scottish Universities Physics Alliance
Date: November 6, 2023

Declaration of Authors Rights

This thesis is the result of the author's original research. It has been composed by the author and has not been previously submitted for examination which has led to the award of a degree.

The copyright of this thesis belongs to the author under the terms of the United Kingdom Copyright Acts as qualified by University of Strathclyde Regulation 3.50. Due acknowledgement must always be made of the use of any material contained in, or derived from, this thesis.

Signed:

Dated: November 6, 2023

Abstract

Scanning electron microscopy allows for the investigation of materials down to the nanometre scale. In this thesis I combine cathodoluminescence spectroscopy with complementary techniques to investigate a range of III-nitride semiconductor heterostructures.

I first describe my investigation of AlGaN-coreshell nanorod UV-LED structures, where I successfully characterised their optical, electrical and structural properties. The electrical measurements were enabled by a nanoprobing system for in-situ contacting within the scanning electron microscope combined with bespoke focused ion beam deposition and milling to create contacts on individual nanorods. I-V measurements and electron beam induced currents confirmed the formation of a *p*-*n* junction and successful doping within the structure. In the same microscope, I measured cathodoluminescence and found optically active quantum wells emitting near 300nm, with some variation in energy and intensity as well as evidence of clustering. Using a pulsed electron gun system, I performed low temperature and time-resolved measurements to find the speed of the recombination in the quantum wells and reveal a reduction in the quantum confined Stark effect within these structures. In a transmission electron microscope, energy dispersive X-ray analysis confirmed the existence of clusters occurring at a-plane nanofacets.

Using this same combination of techniques, I also examined planar UV-LED structures. I found that screw dislocations pinned the position of hexagonal hillocks during growth. In each of the penetrated layers, higher point defect densities and three-dimensional growth enclose the threading dislocations. These point defects can compensate electrical dopants and increase parasitic recombination reducing quantum well emission intensity. I found that during growth, the emergence of multiple facets with distinct incorporation rates leads to alloy composition and doping fluctuations, resulting in hexagonal structures interconnecting and forming a network. I discovered that by changing the alloy compositions present within the LED structure, screw-type threading dislocations can either enhance recombination (non-radiative) or reduced it.

Finally I discuss lateral polarity heterostructures, which contain alternating stripes of Ga- and N-polar material. Electron backscattered diffraction measurements confirmed the stripes were of the intended polarity but found in addition small inclusions of undesirable material in the Ga-polar regions. With cathodoluminescence spectroscopy I investigated the properties of the two distinct domains as well as their interface. I found that the Ga-polar region displayed far greater defect luminescence, consistent with many previous studies.

Acknowledgements

Of course it is essential that I thank my two fantastic supervisors on this project: Professor Robert Martin and Dr Paul Edwards. Rob offered me this opportunity and has guided me along this path remaining encouraging and patient throughout. Paul has been a mentor to me for many years now and his experience and knowledge has been invaluable.

I would also like to mention my office mates throughout the years: James Denholm, Elena Pascal and Daniel Hunter who provided much needed advice and friendship. Of course, the rest of the SSD group have been nothing but welcoming and helpful. In particular I should highlight Jochen Bruckbauer for his assistance in EBSD measurements and discussions regarding this topic.

The collaborations between some wonderful external parties and myself have proven productive and fruitful. Thanks to:

Pierre-Marie Coulon and Philip Shields at CNRS-CRHEA and the University of Bath for their work developing the nanorod structures I describe in the fourth chapter of this thesis and their discussions and encouragement regarding this work;

Simon Fairclough, Gunnar Kusch and Rachel Oliver for their microscopy work and allowing me the privilege of visiting and working along side them at their facilities in the University of Cambridge;

Tim Wernicke, Frank Mehnke and Michael Kneissl from the Technical University of Berlin for providing me with a wealth of UV-LED materials to work with and study.

Publications

D. Cameron, K.P. O'Donnell, P. R. Edwards, M. Peres, K. Lorenz, M. J Kappers and M. Bockowski, "Acceptor State Anchoring in Gallium Nitride", Appl. Phys. Lett. 116, 102105 (2020).

D. Cameron, P. R Edwards, F. Mehnke, G. Kusch, L. Sulmoni, M. Schilling, T. Wernicke, M. Kneissl and R. W. Martin, "The influence of threading dislocations propagating through an AlGaN UVC LED", Appl. Phys. Lett. 120, 162101 (2022)

D. Cameron, P. M. Coulon, S. Fairclough, P. R. Edwards, G. Kusch, T. Wernicke, N. Susilo, R. A. Oliver, P. A. Shields and R. W. Martin, "Coreshell AlGaN Nanorods as Ultraviolet Light Emitting Diodes", In preparation

Previous Publications

P. R. Edwards, K. P. O'Donnell, A. K. Singh, **D. Cameron**, K. Lorenz, M. Yamaga, J. H. Leach, M. J. Kappers, M. Boćkowski, "Hysteretic photochromic switching (HPS) in doubly doped GaN(Mg):Eu—a summary of recent results", Materials. (2018)

A. K. Singh, K. P. O'Donnell, P. R. Edwards, **D. Cameron**, K. Lorenz, M. J. Kappers, M. Boćkowski, M. Yamaga, R. Prakash, "Luminescence of Eu^{3+} in GaN(Mg, Eu): transitions from the $^5D_1$ level", Appl. Phys. Lett. (2017)

List of Acronyms

PL – Photoluminescence

CL – Cathodoluminescence

EL – Electroluminescence

YL – Yellow luminescence

SEM – Scanning electron microscope/microscopy

FEG - Field emission gun

EPMA – Electron probe micro analyser

AFM – Atomic force microscope/microscopy

STM – Scanning tunnelling microscope/microscopy

TEM – Transmission electron microscope/microscopy

FIB – Focused ion beam

BSE – Backscattered electron

SE – Secondary electron

ETD – Everhart-Thornley detector

GSED – Gaseous secondary electron detector

ECCI – Electron channelling contrast imaging

EBSD – Electron backscatter diffraction

WDX – Wavelength dispersive X-ray

EDX – Energy dispersive X-ray

EBIC – Electron beam induced current

REBIC – Remote electron beam induced current

EBAC – Electron beam absorbed current

EBIV – Electron beam induced voltage

EBIRCH – Electron beam induced resistance change

RCI – Resistive contrast imaging

LCMK – Low current measurement kit

HAADF – High angle annular dark field

LT – Low temperature

RT – Room temperature

TR – Time resolved

LV – Low vacuum

SL – Super lattice

QW – Quantum well

SQW – Single quantum well

MQW – Multi quantum well

EBL – Electron blocking layer

TD – Threading dislocation

TDD – Threading dislocation density

IQE – Internal quantum efficiency

EQE – External quantum efficiency

UV – Ultraviolet

IR – Infrared

QCSE – Quantum confined Stark effect

MBE – Molecular beam epitaxy

MOVPE – Metalorganic vapour phase epitaxy

HVPE – Hydride vapour phase epitaxy

ICP – Inductively coupled plasma

HEMT – High electron mobility transistor

PPI – Periodically polarity inversed

LPH – Lateral polarity heterostructure

IDB – Inversion domain boundary

ELO – Epitaxial lateral overgrowth

Contents

Chapter 1

Introduction

We live in the electronic age. Significant global sectors such as transport, lighting, finance, agriculture, entertainment and defence are all now built upon semiconductor technologies. The current silicon chip shortage serves to highlight our dependence. A humble smartphone–a modern everyday essential–may alone contain fifteen billion transistors within its central processing unit, a rather staggering number which is likely to continue to rise for some time. Despite their widespread use there still remains room to improve devices and numerous problems left to solve.

The III-nitride family of semiconductors are the focus of my thesis. Solid-state lighting based on these materials has replaced incandescent bulbs and fluorescent tubes at a remarkable rate due to their high efficiency and low cost. These materials are now also beginning to penetrate the power electronics market with consumer grade fast chargers and power supplies now commercially available. [1]

Energy savings not only impact a consumer's wallet, but also assist in the current battle against global warming. It is estimated that around 15% [2] of electrical power generated globally is wasted through the multiple inefficient power conversion steps taken from source to device. It is hoped that III-nitride based electronics will help reduce this waste.

The present coronavirus global pandemic has highlighted another key area where nitrides could be deployed, with UV-LEDs offering the potential for disinfection and sterilisation, in a non-toxic and portable form. [3] Similar devices could be used for water purification, enabling safe drinking water for regions with poor infrastructure or during national emergencies. [4] This is due to photons with wavelengths below $\approx$300 nm possessing sufficient energies to drive photochemical reactions in DNA and RNA which can inactivate microorganisms and viruses.

The desire for smaller and faster devices with new functionalities creates additional challenges in crystal growth, processing and characterisation. Structures such as nanowires are one potential route to device miniaturisation, and could also enable flexibility when combined with elastomeric materials. [5, 6]

Investigating such small structures becomes a challenge in and of itself. Working within a scanning electron microscope enables high resolution characterisation and investigation. I utilize a nanoprobing system hosted by such a microscope, facilitating both the measurement and manipulation of nanostructures in real time. Understanding variations across devices and small scale structures is key to unlocking the full potential of this material system.

1.1 III-Nitrides

Gallium nitride (GaN) was first synthesised in the 1930's by Johnson [7], Juza and Hahn [8]. It was another thirty years before the group of James Tietjen at the Radio Corporation of America's materials research department pursued the epitaxial growth of this material for blue light emitting devices. Paul Maruska first formed GaN films on sapphire substrates in 1969 using hydride vapour phase epitaxy. Shortly after this in the same research group Jacques Pankove demonstrated the first (inefficient) electroluminescence from a metal-insulator-semiconductor diode. However, the material grown at this time was intrinsically n-type due to unintential incorporation of impurities and attempts at p-type doping proved unsuccessful. By the late 70s Tietjen demanded the group "stop with this garbage." [9]

A resilient team in Nagoya did not give up so easily. While exploring the cathodoluminescence properties of magnesium doped GaN in 1989, Hiroshi Amano noted an increase in luminescence during and after exposure to the low energy electron beam. [10] Here he had accidentally stumbled upon acceptor activation by e-beam irradiation. Isamu Akasaki was the first to utilize this p-type material to form p-n homojunctions with an efficiency of roughly 1%. [11] Shuji Nakamura followed up this work with an alternative method of activation more suitable for commercial applications: high temperature annealing. [12] This trio was awarded the 2014 Nobel Prize in Physics for "the invention of efficient blue light-emitting diodes which has enabled bright and energy-saving white light sources."

Chapter 2

Fundamentals

2.1 Band Gaps

During the formation of a semiconductor crystal, the close proximity and periodicity of the atoms causes the previously distinct energy levels to broaden into bands. Due to the periodic nature of the crystal lattice, only certain energy states are permitted, leaving a forbidden gap in between. [13, 14] These band-gaps are a key feature of semiconductors. The divide between insulators and semiconductors can become hazy, with no definite value where one becomes the other. AlN has a band gap of 6.2 eV and is considered a semiconductor, while sapphire (Al_2O_3) has a bandgap of 8.82 eV and is typically considered an insulator. [15] The band structures are typically not flat and the band gaps may be direct or indirect depending on the material in question. Whether the gap is direct or not impacts the efficiency of radiative transitions within the material, with indirect transitions requiring phonon assistance to conserve momentum during the relaxation process. The energy of the band gap is an extremely important parameter, determining the conductivity, absorption and emission properties of the material. A range of disordering mechanisms in a real semiconductor can allow for transitions below the expected band gap with the density of states increasing deeper into the bands, resulting in an Urbach tail which is commonly observed in the absorption spectrum of materials. [16, 17] Interestingly, the band gap is anisotropic in many materials.

2.2 Crystal Structures

The III-nitrides AlN, GaN and InN and their alloys can appear in many different polytypes including: wurtzite, zinc-blende, hexagonal, haeckelite and rocksalt. Here I focus on wurtzite, the most common and stable form. [18]

The wurtzite crystal structure consists of two overlapping hexagonal closed packed structures offset by 5c/8 with four atoms per unit cell. [19] The tetrahedral symmetry from the sp^3 bonds [20] gives four nearest neighbours of the alternate species leading to a unit cell with two lattice constants c and a.

Epitaxial layers can develop under tensile or compressive stresses which changes atomic spacing in the crystal. When the lattice is deformed in this way, charge distribution is unbalanced, inducing piezoelectric polarisation. In a strained state the electrical and optical properties of a layer will be modified. However, even in strain-free nitrides polarisation effects occur.

The difference in atomic radii and Pauling electronegativity leads to an ionic character of the crystal. Ionicity of the bond demands the charge is not distributed equally between the atoms leading to the formation of a dipole. The lack of inversion symmetry (non-centrosymmetric system (C_{6v}^4) defines the critical direction of the spontaneous polarisation field and gives rise to Ga/Al/In-polar and N-polar crystals. The direction of internal polarisation fields is also influential on the electrical properties of devices. I emphasise that polarity is not defined by surface termination, but by the direction of this bond.

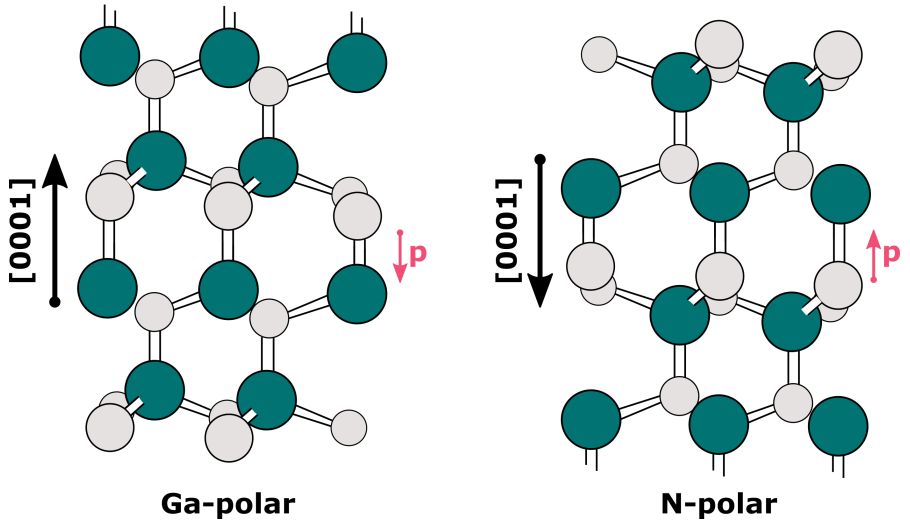

Figure 2.1: **GaN in the wurtzite phase shown in its two polar forms with the c-axis and associated spontaneous polarisation field directions labelled.** Figure redrawn from [21]

If a crystal is Ga(N)-polar and we were to cut along the c-plane through axial bonds exclusively, the exposed top surface would be Ga(N) terminated. [18] The chemical and electrical properties of these surfaces differ, allowing for creative growth and device development. The chemical reactivity of surfaces governs the defect or dopant incorporation rates in the crystal during epitaxy and is also important for the growth of low dimensional nanostructures. [22] These distinct incorporation rates can be a hurdle to producing high quality material, although may be of assistance for certain doping strategies. [23] The different terminating surfaces will also present unique band bendings and surface accumulation layers, changing the contact properties and reflectivity. Polar crystals are the subject of discussion in Chapter 7.

Planes and directions in these crystals are described well by four-digit Miller-Bravais indices. Examples of some common planes and directions are provided in Fig. 2.2. Most standard III-nitride growth occurs in the c-direction leading to polar materials as previously mentioned, however semi-polar and non-polar growth are both possible but create new challenges such as anisotropic lattice constants and the potential implications on strain. The reward is reduced polarisation fields which could bring performance improvements to many devices. [24]

Alloying of the III-nitrides allows for layers with specific lattice constants and bandgaps to be produced. With direct gaps ranging from 0.69 to 6.2 eV, optoelectronic devices could in theory emit from the infrared to the deep UV. Strictly speaking Vegard's law describes a linear relationship between lattice constant and composition. However, similar expressions can be found relating composition and bandgap (Eqn. 2.1). Here, the resultant band gap is a function

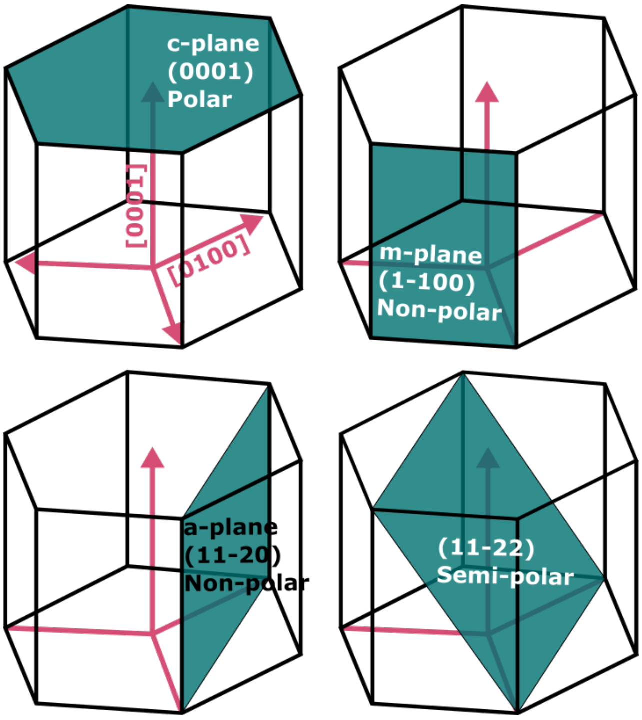

Figure 2.2: **Common crystal planes and directions with their polarisation labelled.** Figure inspired from [25]

of the two binaries and a bowing parameter, "b", [26] which attempts to correct for inaccuracies in these simple empirically derived expressions.

$$E_{g(ab)} = xE_{g(a)} + (1-x)E_{g(b)} - bx(1-x) \tag{2.1}$$

The exact values of these bowing parameters are still debatable but a simple linear fit fails to account for the true complex nature of the system. The difference in atomic bond lengths between the two binary alloys can create strain and local fields which may influence the bandgap. Random alloying and agglomeration may also create regions of high carrier localisation which further effects measured values. A final point is that high carrier densities can cause a Moss-Burnstein energy shift due to a filling of lower lying states. [27, 28, 29]

From Fig. 2.3 we see InAlN as a possible route to UV emission with a better lattice match than AlGaN, however growth of this material is difficult and phase separation may occur. [30]

By stacking alloys with different band gaps we can create localised regions with a narrowed gap, thereby forming quantum wells. These potential wells can trap or confine carriers and enhance radiative recombination efficiency. If the bands are not flat, as is common in the polar III-nitride systems, the quantum confined Stark effect (QCSE) can occur. In this case a separation of electron and hole wavefunctions occurs, red shifting emission and counterproductively reducing radiative recombination efficiency.

By creating repeated structures of quantum wells (multiquantum wells (MQW)) we can further improve the efficiency of luminescent devices allowing more carriers to be confined without increasing their density in the wells. The thickness of the barriers and quantum wells are a critical parameter, affecting strain, recombination efficiency and emission wavelengths. In addition to barriers encasing the individual quantum wells, electron blocking layers (EBL)

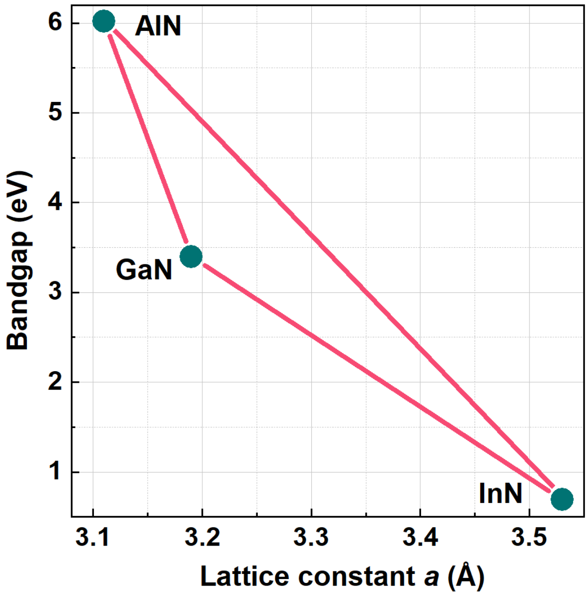

Figure 2.3: **Plot of bandgap energy vs. lattice constant of the III-nitrides with no additional bowing added.**

may be deployed on the p-side of the structure. An EBL is required due to the difference in hole and electron mobilities. For example in AlN the electron mobility is $300\,\mathrm{cm^2V^{-1}s^{-1}}$ and hole mobility $14\,\mathrm{cm^2V^{-1}s^{-1}}$. This can result in electron leakage from the active region. [31, 32] The design of the EBL should strive to keep electrons in MQW regions while having minimal pertubation of the hole injection.

Higher dimensional confinement can create quantum dots. An attractive quality of the III-nitrides is their relatively high exciton binding energies, allowing for quantum dots to function as single photon sources above cryogenic temperatures. [33, 34, 35] For future quantum technologies having reliable single photon sources will be vital.

2.2.1 Doping

By intentionally incorporating impurity atoms into the lattice we can "dope" a semiconductor to modify its properties or enable new functionalities. Some would argue that doping is the defining characteristic of semiconductors. For example, doping GaN with Si should create additional donors and may render the material more conductive and n-type, while doping with Eu would create luminescent defect centres allowing for the generation of red light.

Through defect formation, electrical compensation and self-compensation may occur, an interesting case being Mg-doping in GaN. This should give p-type material, but due to hydrogen unintentionally incorporated during growth the Mg acceptors are compensated/passivated. [36] It was discovered that high temperature annealing or e-beam annealing can remove the hydrogen from the crystal and leave a p-type product. [10, 12] This annealing process is still an active area of research, with ever-increasing percentages of acceptor activation being demonstrated through advanced methods. [37] The hole density is limited through the formation of vacancy defects when the Fermi level reaches a critical point. At high Mg concentrations the hole density actually begins to decrease due to secondary mechanisms. [38] This is also seen when excessive doping of Si no longer increases n-type conductivity and actually rather quickly leads to an insulating layer. [39] Compensating or passivating defects that are removable through annealing can allow for higher doping concentrations to be achieved.

Doping allows for the creation of p-n junction, a fundamental building block in many electronic devices. When a p-layer and n-layer are placed together, a depletion region forms as carriers from each are exchanged. At equilibrium we are left with a p-region, a depletion region (space-charge) and an n-region. This creates a diode and the depletion region can allow for photocurrents to be generated even in the absence of an external field, creating a basic form of passive detector.

2.3 Defects

Defects can influence the structural, optical and electrical properties of the crystal significantly. Their role in device breakdowns and failures is known, but not fully understood. Although different categories of defect are discussed here separately, interaction between the different defects can occur and so in practice they must be all considered collectively.

2.3.1 Point Defects

I will start by discussing the range of point defects which can form in nitrides. Native defects are those which do not contain impurities. This includes vacancies and anti-sites, where a cation or anion are missing or have been exchanged in position. Native interstitials may also form when an ion lies off site. Non-native defects occur when foreign species are deposited into the crystal as a direct substitution or otherwise. When this is intentional we call it doping. A simple illustration showing some of these defects can be seen in Fig. 2.4

Point defects may introduce shallow or deep levels within the gap. The location and charge state of the impurity will affect the position of these levels. These impurities may also affect the local symmetry of the crystal.

Defects like dopants may also influence the electrical conductivity of a material. For instance non-intentionally doped GaN is typically found to be n-type due to oxygen incorporation during growth. [40]

The probability of various point defects forming can be related to their “formation energies”, which describe the cost to form them intentionally or otherwise, typically with respect to the Fermi level of the system. To further reduce their energy, defects may congregate and form complexes. [41] Low formation energies suggest that the defect is very likely to form due to its low cost. Due to being a function of the Fermi level, illumination by above band-gap light during growth has been shown to modify the defect populations present in the final product. [42]

Point defects are not always detrimental; on occasion they can be harnessed or even intentionally produced (known as defect engineering) to create centres with specific properties for applications such as quantum communications. It has already been shown that point defects in III-nitride materials have potential as on-demand single photon sources [43, 44, 45] and solid state qubits [46], both integral components in quantum information systems.

Point defects may also act as carrier traps and aid in energy transfer to colour centres within the crystal host. [47] Overall their effect on luminescence is mixed, as point defects can both facilitate luminescence as well as quench it. In nitrides, defect luminescence typically appears as broad and structureless bands. Despite decades of experimental and theoretical work, the

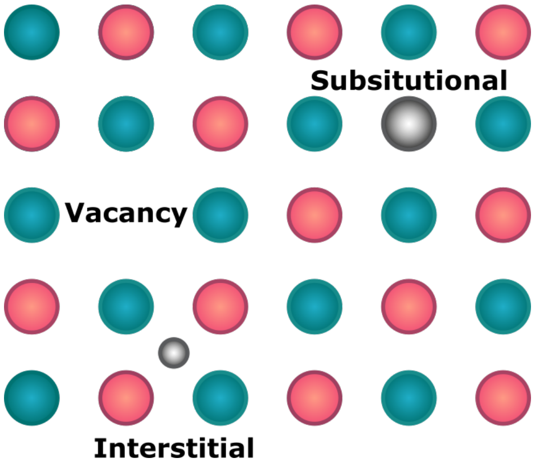

Figure 2.4: **Illustration showing an assortment of point defects that may appear.** Different atomic species are shown by their colours and defect types are labelled.

origin of many common defect bands remain under some debate. [48]

In the special case of rare-earth defects, incredibly sharp luminescence lines related to the multiple optical transitions within the dopant ion may be observed. This is possible thanks to shielding of the inner 4f-electrons by the outer shell, protecting them somewhat from the influence of external crystal fields. [47, 49] These ions can actually be used as spectator ions to study other defects within the material [50], as colour centres for RGB lighting or for quantum technologies [51].

2.3.2 Extended Defects

Extended defects are structural imperfections in a crystal which can be mobilised and modified through the input of energy. [52] They may be introduced by a number of mechanisms, but commonly associated with strain relief at highly mismatched interfaces.

Unlike in Si or Ge where material can be grown with a dislocation density of zero [53], III-nitrides are full of defects, and yet can still effectively function. This is one of the most extraordinary things about this material system, where dislocation densities in excess of $10^9\,\mathrm{cm}^{-2}$ are regularly reported, yet some commercial devices can operate with 95% internal quantum efficiency (IQE). [54]

A common group of extended defects are threading dislocations also known as line defects. There are three types of such defects; edge, screw and mixed. Edge-type are typically the most numerous and occur when there is a missing half plane or additional half plane (depending on your philosophical outlook) present in the lattice. The dislocation line in this case runs along the edge of this half-plane as seen in Fig. 2.5. This can alternatively be thought of as a “slip” of crystal planes, with the magnitude and direction of this slip being described by a Burgers vector. In the edge case the direction of the Burgers vector is perpendicular to the dislocation line. For screw type-threading dislocations the dislocation line is parallel to the Burgers vector.

Mixed dislocations occur when we are at some angle in between the two, where it is neither perfectly parallel or perpendicular to the Burgers vector.

Different dislocation core types have been observed by transmission electron microscopy and studied theoretically. These can create new states, adding levels into the gap and forming new

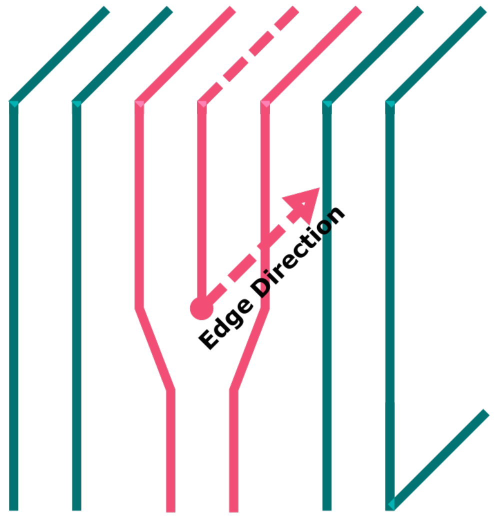

Figure 2.5: **Illustration of an edge dislocation with the direction labelled.**

recombination pathways. [55, 56]

Stacking faults are another common occurrence, where the periodic stacking structure is disrupted briefly. These planar defects can help to release strain in the layers as growth develops. [57] In wurtzite systems they typically appear as basal stacking faults (BSF) or prismatic stacking faults (PSF) which describes along which plane the stacking varies.

If a polycrystalline growth mode occurs, grains coalesce to form the solid. This leads to the formation of domains and grain boundaries, which may present novel properties. In $CuInSe_2$ solar cells for example, strong separation of carriers occurs at these boundaries forming the basis of operation. [58]

Point defects and extended defects both interact and influence one another, producing interesting effects. For example, the Cottrell and Suzuki mechanisms describe enhanced point defect incorporation around threading dislocations and stacking faults, in order to minimise strain and lower their energy. [14] This is sometimes described as a “gettering” effect.

Surface Defects

At a terminating surface of a semiconductor the periodicity of the crystal is disrupted. Bonds may remain dangling, impurities may attach from the air or surface reconstruction may occur. These all lead to new potentially problematic states being introduced. Surface states may be particularly influential in nanowires, where the free surface/volume ratio is far greater, but surface defects may also form at heterointerfaces (e.g Schottky contacts). Surface passivisation may be performed to reduce these effects at free surfaces. [59] The surface states can lead to surface band bending and Fermi level pinning, which additionally influence any potential contacting. [60]

2.4 Growth Methods

There are now many different methods to grow III-nitride heterostructures. The most common approaches include hydride vapour phase epitaxy (HVPE), molecular beam epitaxy (MBE) and metal organic vapour phase epitaxy (MOVPE).

HVPE was the first [61] successful epitaxy technique used for III-V growth. It boasts high growth speeds, and is excellent for depositing thick high quality layers, however interfaces are difficult to control. It is now regularly used for growing thick GaN layers where the substrate is subsequently removed, creating freestanding GaN substrates with extremely low defect densities and impurity concentrations for further epitaxial growth. [62, 63] HVPE is a two stage growth process: first at lower temperatures, Ga interacts with HCl forming GaCl which can then via a carrier gas (H_2,N_2 or Ar) enter into the second stage at a higher temperature (1000-1100°). In this second stage the GaCl reacts with ammonia (NH_3) to form GaN on the seed crystal.

A more precise growth method is MBE. Here, atomic or molecular sources are evaporated in effusion cells and directed at a hot substrate in coincidence with a nitrogen plasma beam where growth develops layer by layer. This leads to highly defined interfaces and layer thickness control, as the layers can be monitored in situ through reflection high-energy electron diffraction or Auger electron spectroscopy. The lack of carrier gasses involved and ultrahigh vacuum chambers required also help to improve the purity of material. However, this is a relatively slow process and does not scale well for industrial applications.

MOVPE, is faster deposition method than MBE and is widely used in large scale commercial applications. In this method precursors such as ammonia (NH_3) and trimethylgallium (TM(Ga/Al/In)) are guided by a carrier gas over a hot substrate. This approach results in interface control superior to HVPE but worse than MBE. [64]

Although uncommon, it is possible to combine these growth methods to take advantage of their individual qualities. This can be seen in the MBE regrowth of contacts layers on top of MOVPE-grown high electron mobility transistors (HEMTs). [65]

The lattice constant is an important parameter to consider in epitaxial growth. Mismatch produces highly strained layers which leads to defective material and potential wafer bowing or cracking. [66] The thermal expansion coefficients must also be considered for the same reasons as above, with growth occuring at various high temperatures followed by cooling which can lead to failures such as the catastrophic cracking of the wafer.

One of the major breakthroughs in the development of GaN based LEDs was the low temperature buffer layers as an initial stage during growth. [67, 68, 69] These layers help to promote effective nucleation sites and lateral growth, while preventing cracks and trapping some surface defects.

Nitridation or other surface treatments can form interesting thin layers such as SiN_x which influence the following growth, changing crystal structure or polarity. These thin transitional layers can significantly influence the electrical and optical properties of the final device.

Each of the III-nitrides alloys present their own unique challenges. The quality of InN is particularly poor due to the low dissociation temperature combined with large lattice mismatch to AlN/GaN buffers. [70] For this reason when working with InGaN low temperature growth is normally required to stop desorption of In atoms. Typically composition is limited to around 35% InN content due to lattice mismatch between GaN and InN (>10%), contributing to the so called “green-gap”, where internal quantum efficiency rapidly decreases with increasing InN content. [71] For this reason, red nitride LEDs are currently not yet commercially utilized and InGaAlP still dominates this market. There are companies trying to remedy this issue through the use of porous GaN. By creating a thick porous layer on top of sapphire subsequent growth will be significantly relaxed. These thick initial layers are often described as “pseudo-substrates”. Both Porotech and work at the University of California Santa Barbara utilize this approach in different ways. [72]

InN rich alloys also have trouble with In agglomeration due to the self affinity. [73] While the use of the term “clustering” may be controversial [74], segregation definitely occurs at step edges and surface features. [75] Note even on a smooth surface some inherent random alloy fluctuations will occur, causing variations in the local potential enhancing carrier localisation and decreasing the diffusion length. [76] This is one of the suggested reasons why, despite high TDD, the nitrides function so well. [77] Composition pulling effects can also influence InN incorporation when growing strained layers, where indium concentration varies with layer thickness. [78, 79]

Different challenges are presented when working with AlGaN emitters for UV applications. A few of the main problems pertain to high activation energies of dopants, high defect densities lowering IQE and the polarisation of emission due to the valence band structure of AlN. [80] Due to the higher ionicity of the Al–N bond a negative crystal field splitting is expected. This influences the ordering of the valence bands, the highest of which being the most impactful for optical transitions. In the case of AlN the uppermost band prohibits recombination perpendicular to c. [81, 82] In the case of GaN the opposite is true, with recombination parallel to c forbidden. In AlGaN alloys the balance of optical polarisation is not only effected by the composition, but also by the strain and confinement of the layer. [83] This can lower the extraction efficiency of a device if the directionality of the light generated internally is not towards the intended face of escape.

With AlGaN the high sticking coefficient of the Al ions on the surfaces can lead to roughened surfaces and challenging selective area growth. The IQE of AlGaN has also been found to be more sensitive to threading dislocation densities compared to InGaN. [84] To counter this problem some groups have instead utilised InAlGaN in the active regions of devices, relying on InN segregation effects caused by In self affinity to enhance localisation of carriers and improve recombination efficiency. [85]

2.4.1 Nanostructuring

Nanostructures come in many different forms such as spheres [86], stripes [87], wires [88], dots [89] and even complex forms resembling plants, flowers and fruits. [90] These structures present potential advantages over traditional planar forms such as reduced defect densities and polarisation fields. However producing such forms can be difficult. Three common epitaxial approaches can be taken: bottom-up growth, top-down etching or a hybrid of the two.

For bottom-up approaches selective area growth is required. This can be done using a mask, with growth continuing through the gaps, allowing for the shapes to be dictated as wires, stripes or more. [91] Another approach involves the deposition of nucleation sites such as gold or nickel which can be scattered over the substrate surface. [92] Self assembly of nanostructures can also occur under certain growth conditions, where the growth mode conveniently forms wires, quantum dots, v-pits or pyramids. [89, 93, 94] A silicon flux during growth has been shown to greatly enhance the vertical growth rate of GaN NWs. [95] These bottom-up growth methods typically lead to the growth of structures with somewhat random pitches and dimensions.

With top-down approaches, the heterostructure stack is grown in the traditional planar way and post-growth etching is carried out. [96] This etching can be performed selectively using masks, or guided by a natural process following some crystallographic directions dependent on the chemistry involved. However this can limit the device architecture, with sidewalls only being exposed post etch.

A hybrid method combining the top-down etching with bottom-up growth can overcome the limitations of the two constituent techniques. [97] We can achieve high uniformity and control and produce structures not possible by the two individual methods. It is this method that is employed in Chapter 4 to produce core-shell nanorods.

2.4.2 Substrates

The substrate employed will significantly impact the qualities of the final device; dictating crystal structure, orientation, defect densities, thermal and optical properties. As devices get smaller, so must heatsinks and so high thermal conductivity of all components is important.

Silicon (Si) is attractive due to its low cost and the potential to expand pre-existing Si production lines. [98] The idea of structures being grown directly onto Si chips is enticing for industry, but the narrow band gap could limit its applications. Furthermore the lattice mismatch between III-nitrides and Si is large and there is also an issue of "meltback" to contend with which can occur when Ga reacts with Si. [99]

Sapphire (corundum Al_2O_3) remains one of the most popular options. It has the advantages of being highly insulating which can be useful for both electronic and optical devices and the lattice match is better than Si. It also has high thermal and chemical stability. However it does possess relatively poor thermal conductivity. [100]

For devices requiring significant heat dissipation such as 5G communication devices [101], 6H-SiC offers superior thermal properties in addition to a closer lattice match, but is more expensive than sapphire and has a relatively narrow band gap of 3.08eV.

Carbon allotropes are another more experimental choice at this time. GaN on diamond is currently being explored as a potential replacement for 6H-SiC in radio-frequency high electron mobility transistors (RF-HEMTs) due to the excellent thermal conductivity of the diamond. Through either direct growth or wafer bonding the diamond offers lower operation temperatures and enables throttle-free operation of a device, as well as longer lifetimes and stability. [102] Another interesting allotrope—graphene—is a 2D material which allows for near lattice matching and avoids thermal expansion issues during growth. In a final device it may also offer transparent contacting which is particularly useful in a UV-emitter. [103, 104]

Freestanding GaN substrates, remain expensive but show extremely low defect densities (10^6cm^{-2}). This allows for increased breakdown voltages which are particularly important for high power electronics. [105, 106] A typical approach to creating these substrates involves an intial growth of very thick HVPE growth GaN on sapphire or GaAs [107] followed by substrate removal. These substrates can be used for c-plane or m-plane growth, with the excellent lattice match in both directions as it can be homoepitxial.

To reduce high threading dislocation densities, epitaxial lateral overgrowth (ELO/ELOG) templates were developed. [108] The dielectric mask used in the process blocks any threading dislocations that are present below, immediately lowering the TDD beyond this point. The growth modes through the gaps are such that TDD will then tend to be bent at 90° reducing vertical propagation as the layer thickness increases and the islands or stripes coalesce. [109] The sapphire is first etched into large ridge structures or a striped mask and is covered in AlN. The etch depth combined with substrate miscut angle [110, 111] and direction [112] influence the

Alloy	Lattice constant a (Å)	Bandgap (eV)
AlN	3.11 [117]	6.2 [118]/6.12 [81]
GaN	3.19 [119, 120]	3.4 [18]
InN	3.53 [121]	0.69 [122, 123, 26]
6H-SiC	3.08	3.0
Diamond	3.57	5.47
Sapphire	4.79	8.82 [124]
Si	5.43	1.12

Table 2.1: **Lattice constants in a-direction indicating lattice matching at 300K.** Note that the bandgap for all III-nitrides in this table are direct gaps in the wurtzite phase.

quality of the final AlGaN layers, affecting the surface morphology, defect density and alloy homogeniety. [113] ELO growth can be combined with other techniques such as high temperature annealing to further reduce TDD. [114] More recently a related technique of nanopatterened sapphire substrates (NPSS [115]) appears to offer enhanced light extraction for deep UV emitters as well as the reduction in TDD. [116]

2.5 Electronic Transitions

In solid state physics we can simplify systems by describing the absence of an electron as a positively charged quasiparticle known as a hole. When an electron is excited to a higher lying electronic state, it leaves behind a hole. If an electron recombines with a hole, it can do so radiatively (producing a photon) or non-radiatively (commonly phonon or energy transfer). The probability of a transition is determined by the selection rules with some being forbidden entirely. Electronic transitions are useful for LEDs and lasers but also for sensors, where the opposite process can occur with the absorption of a photon generating an electrical current (see EBIC). I will discuss a few of the most common recombination processes in the following paragraphs.

Auger recombination involves an electron relaxing and transferring its energy to another particle (electron or hole), exciting it high into the band. Auger recombination occurs more frequently at high carrier densities because of a cubic dependence on carrier concentration. This is why it is commonly associated with the droop phenomena described in section 2.6. Fig. 2.6 shows this process along with a selection of other recombination processes introduced in the following paragraphs.

Schockley Read Hall (SHR) is a defect mediated mechanism where trap states open new recombination and excitation pathways. The theory posits that deep states near the midgap are more efficient recombination pathways than states near the band edges and hence may heavily influence recombination dynamics. [14]

Donor-acceptor pair luminescence is common due to the high impurity levels in our crystals. This occurs where a positively charged donor and a negatively charged acceptor, trap an electron and hole allowing for subsequent radiative recombination. The energy of this emission is dependent upon the physical separation of the two ions, hence broad peaks are expected.

Free carriers and excitons (free or bound) may also recombine between bands and levels. The wavelength of the band-edge emission is modulated by the Fermi level of the specimen. The Moss-Burnstein effect is considered an absorption effect, but the filling of states in the

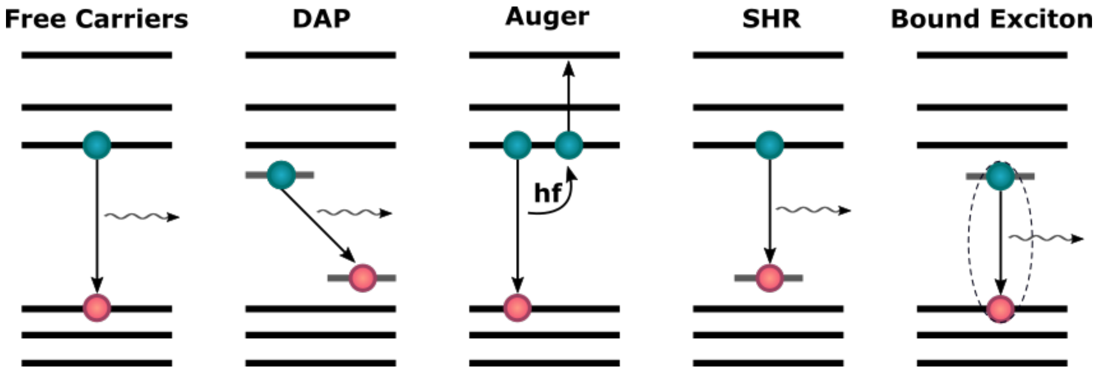

Figure 2.6: **A selection of electronic transitions that may occur within a semiconducting system.** For the purposes of this figure electrons are shown in green and holes in pink.

conduction band also leads to a blueshift in emission and is commonly observed in highly doped layers.

We can attempt to generate luminescence from a semiconductor through a number of methods such as electroluminescence, cathodoluminescence or photoluminesence. The excitation mechanism may affect the emission spectrum and therefore one must be mindful of the method used and its potential influences when interpreting spectral data.

In photoluminescence, an incident photon is absorbed, with the energy exciting an electron from one state to a higher one. This process depends on the wavelength of the excitation source, allowing for above bandgap, below bandgap and resonant excitation to be performed. With adequate optics micro-PL is capable of mapping of materials on micron-scales.

In cathodoluminescence (CL) the electrons have such high energy (keV) that we can excite carriers deep into the bands and across large band gaps with relative ease. Laser sources in the deep UV are still expensive and somewhat sparse. The spatial resolution of CL mapping is also far superior to microPL and is mostly limited by the excitation volume, microscope resolution and collection efficiency. Variation of acceleration voltage also allows for depth resolved measurements. CL is discussed in more detail in the scanning electron microscopy chapter.

Finally in electroluminescence two electrical contacts are made on the material allowing for an electrical current to flow. These contacts are typically placed on the p- and n-regions of a device respectively. Electrons and holes are fed from the two contacts via the conduction band and valence bands respectively and can recombine once they meet. This is discussed more in the in following LED section.

2.6 Light Emitting Diodes

Many of the structures examined in this thesis have been developed with the aim of producing efficient light emitting diodes. The emission wavelength of a device is dictated by many factors including the well composition, width [125, 126], temperature [127, 128], internal fields [129] and carrier density [130].

A basic LED structure will have a quantum well structure sandwiched between n-type and p-type layers. Under a forward bias the depletion regions shrinks and above the turn on voltage, carriers can flow across towards the oppositely doped region. When the electrons and holes interact they may radiatively recombine giving light. The applied current acts to repopulate these carriers ensuring a continuous repetition of this process. This process is illustrated in Fig. 2.7 and this may also help in the understanding of rectification. The *p*-*n* structure obstructs current flow in reverse bias due to the natural barrier that forms. Current that can flow in reverse bias is considered a "leakage" current, which is seen as an adverse effect in many electrical devices.

Past the turn-on voltage of a LED we can enter a somewhat linear region of the I-V relation where heating may become an issue. At even higher voltages and current densities an efficiency droop [131, 132, 133] is observed and increasing the bias no longer continues to increase the current, which is a problem if one wishes to create a high brightness device.

Although droop is still not fully understood, some strategies have been formed to suppress or delay its onset. Current spreading layers can be deployed to help avoid high current densities and their associated problems. Similarly non-polar/semipolar materials may offer additional help as thicker wells can be used which will lower carrier densities in the wells. The use of a *p*-type superlattice may also help. [134] Superlattices can serve multiple purposes. Firstly they can act as improved electron blocking layers, creating substantial barriers to electrons while minimising the reductions in the injection efficiency of holes. They may also help to manage strain and electric fields in the device, further improving performance. [135] Their role in enhancing vertical conduction in devices is somewhat debated. [136]

To further improve the efficiency of devices so called "underlayers" are employed. It has been discovered that by adding an $\mathrm{In}_{(\mathrm{low}x)}\mathrm{Ga}_{1-x}\mathrm{N}$ layer deep in the structure before the active region of visible emitters, non-radiative recombination can be decreased and IQE increased. This underlayer was present in commercial devices far before the mechanism of its effectiveness was truly understood. Chen et al [137] carried out a detailed study on the matter and found that the In atoms capture mobile impurities which occur at the GaN surface. This reduces the concentration of point defects acting as non-radiative recombination centres in the QWs. [138]

In a basic commercial device one can also find mirrors have been added to increase the light output in a specific direction along with encapsulation using an appropriate refractive index to improve light extraction efficiency and decrease total internal reflection. The surfaces of the semiconductor may additionally have been roughened for this goal. [139]

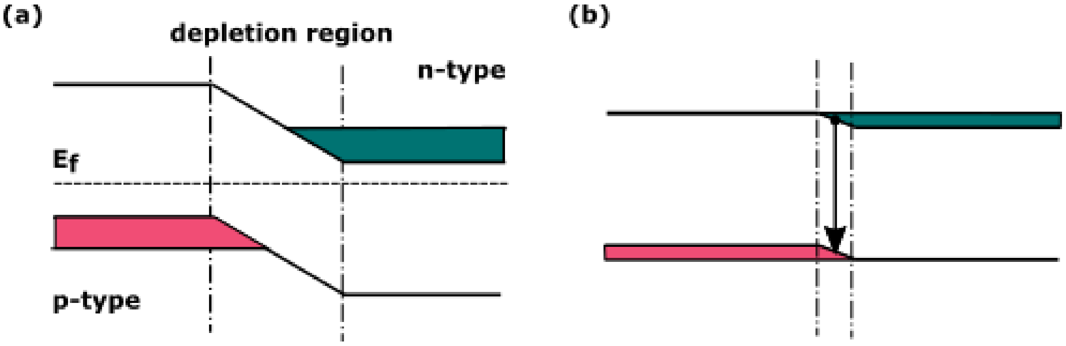

Figure 2.7: **Band structures of a *p*-*n* junction. a,** Shows a *p*-*n* junction with zero applied bias in equiibilibrum. Again holes are shown in pink and electrons in green. **b,** Shows a forward biased diode where current may flow and carriers can recombine in the depletion region (or elsewhere) where they meet.

Chapter 3

Electron Microscopy

Ernst Abbe first described the diffraction limit of a microscope in the iconic form [140]:

$$d = \frac{\lambda}{2n\sin\theta} \tag{3.1}$$

This is a fundamental limitation to conventional microscopy techniques. With de Broglie's revelations in the 1920's, it was realised that by using electrons (or other particles*) in lieu of photons, higher resolution microscopy is possible. The de Broglie wavelength of the particle is given by the following relation:

$$\lambda = \frac{h}{mv} \tag{3.2}$$

with the relativistic electron mass m:

$$m = m_0(1 + \frac{E}{E_0}) \tag{3.3}$$

and velocity v:

$$v = c\left(1 - \frac{1}{(1 + E/E_0)^2}\right)^{\frac{1}{2}} \tag{3.4}$$

$$\boxed{\implies \lambda = \frac{h}{\sqrt{(2m_0E(1 + \frac{E}{(E_0)^2})}}} \tag{3.5}$$

For scanning electron microscopes (SEM) with typical operating conditions ranging from 1→30kV, the full relativistic description may be unnecessary. However, for transmission electron microscopes and their significantly higher acceleration voltages (100→300kV), the full relativistic expression should be considered.

Electron microscopy goes beyond just the imaging of surfaces topographies and nanostructures, numerous processes are triggered by the high energy electron beam in a material, allowing for further information to be extracted.

3.1 The Electron Microscope

Hans Busch invented the first electromagnetic lens in 1926. [141] By 1929 the first description of an electron microscope appears in a patent submitted by Hugo Stintzing. Here he described a system for measuring particles on a surface using a beam of electrons, where external fields could be applied to deflect the beam and scan along a line. [142]

A few years later in 1931 Max Knoll and Ernst Ruska produced the first working electron microscope, however in these early stages the system could not demonstrate a resolution higher than an optical microscope. Ernst's brother Helmut was a medical doctor who played a crucial role in pushing the potential biological imaging applications of such technologies and helped to secure funding and the continuation of Ernst's research.

It was not until 1938 when Manfred von Ardenne created the first electron microscope with a submicron probe. This was a transmission electron microscope (TEM) where images were captured on photographic film, making focusing and alignment extremely challenging. Unfortunately, the emergence of war put an end to his research in this field and his attention was directed toward nuclear projects. His original microscope was destroyed during an air raid on Berlin. [143]

Vladimir Zworykin (assisted by James Hillier, Edward Ramberg, Arthur Vance, George Morton and Richard Snyder at the Radio Corporation of America) developed a new electron detection method in 1942 which set the foundations for modern scanning electron microscopes (SEM). They paired a phosphor and a photomultiplier with a slow scanning speed to create their images. Although their images were poor, this was the forefather of the detection system that Everhart and Thornley produced much later. [144]

In 1948 Charles Oatley began working on SEM development at the University of Cambridge. Despite many expecting their failure he and his PhD student Dennis McMullen produced "SEM1" in 1951. [145] With further time, students and staff (including Ken Smith, Oliver Wells, Tom Everhart and Richard Thornley) the group produced a total of five scanning electron microscopes and this work eventually led to the production of the world's first commercial SEM the "Cambridge Instrument Company Stereoscan" in 1965.

3.1.1 Guns

Modern electron microscope designs take varying forms, but there are fundamental principles common to all. Everything begins with the generation of the primary electron beam. This occurs at the electron gun, which can take one of three forms: thermionic, Schottky or cold field emission.

Thermionic Gun

Electrons can be thermally excited from the Fermi level to overcome the work function of a source material. The source itself can be a piece of tungsten wire, either sharpened to a point or bent into a hairpin, which thanks to the use of a Wehnelt cup allows for highly localised emission. Alternative materials such as LaB_6 with lower work functions can also be used.[146]

Regardless of the source's constitution, it will be held in high vacuum in order to prevent degradation from ion bombardment or oxidation layer formation. For tungsten, temperatures just below the melting point ($\approx 3000\,\mathrm{K}$) are commonplace. Nevertheless, over time, even in high vacuum conditions, the evaporation of source material will occur, limiting the lifetime of the cathode.

The electrons generated are accelerated towards an anode and into the column, with the current generated by this process being described by Richardson's law (Eqn. 3.6). The current can be seen to be a function of the Richardson constant (A), cathode temperature (T_c) and work function (Φ_w). [147]

$$J = AT_c^2 exp(\frac{\Phi_w}{kT_c}) \tag{3.6}$$

Cold Field Emission Gun

An alternative to the thermionic gun is the field emission gun (FEG) as seen in Figure 3.1. Exposing a source tip to a strong potential can decrease the width of the barrier, allowing for electrons to escape the metal through tunneling. The current generated through such a process can be approximated from Fowler-Nordheim theory, where the current density no longer depends on temperature and only on the strength of the applied electric field (E), the work function of the material (Φ_w) and some constants B and a. [148]

$$J = aE^2 exp(-B\Phi^{3/2}E) \tag{3.7}$$

In a FEG there are two anodes, the first creates tunneling compatible conditions and the second accelerates the current into the column. With this two layer system the first anode could absorb some of the generated current. To avoid this, the tip is orientated along a specific crystallographic axis as the work function is dependant upon the orientation. This gives the added benefit of forming a smaller probe size than is possible with a thermionic gun.

Unlike its thermionic brethren, the working principle of the FEG is functional at room temperatures, but operation above 1000K can help to prevent contaminant adsorption on the tip. The main advantages of the FEG over the thermionic gun are the smaller probe size, higher brightness and longer average cathode lifetime. [141]

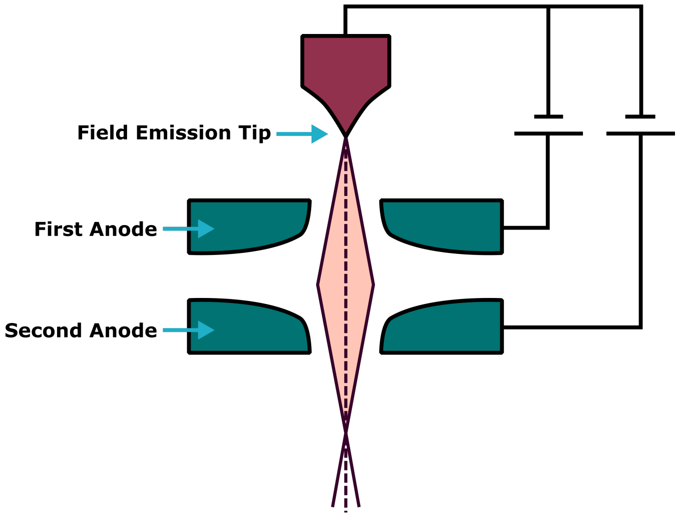

Figure 3.1: **Schematic of a field emission gun. Here we can see the two anodes involved.** The first anode controls the current while the second controls the voltage. Modified from [147]

.

Schottky Field Emission Gun

Schottky field emission guns are rather similar to the cold FEG. A potential can be applied to manipulate the barrier, but instead of narrowing the barrier to allow tunneling, it is lowered by the Schottky effect, allowing for electron emission at lower temperatures than in the standard thermionic gun. This can be described by adjusting the previously shown Richardson's Law to include an effective work function.

$$J = AT_{\mathrm{c}}^2 \exp(\frac{\Phi_{\mathrm{eff}}}{kT_{\mathrm{c}}}) \tag{3.8}$$

where

$$\Phi_{\mathrm{eff}} = \Phi_{\mathrm{w}} - \sqrt{\frac{q^3 E}{4\pi\epsilon_0}} \tag{3.9}$$

3.1.2 Lenses

Electron lenses are typically capacitors (electrostatic) or magnetic coils (electromagnetic), which through Lorentz forces can deviate the paths of nearby electrons. Condenser lenses collimate the beam emitted from gun and adjustment of the objective lens varies the focal length, reducing or increasing the probe size. The depth of field varies as a function of working distance, but will ordinarily exceed that of an standard optical system due to the smaller numerical apertures.

When electrons pass through a lens, numerous detrimental effects can occur. For example, the focal length of a lens has a dependence upon electron energies and since there will always be a small range of energies emitted from the gun, chromatic aberrations will occur. The lens current itself may also vary and modulate the focal length accordingly. When the focal length in the sagittal and meridonal planes differ, astigmatism occurs. There can be many causes of an asymmetric focus such as imperfections of the polepiece or apertures. Stigmator coils can be employed to compensate for this, with their currents and hence field strengths modified.

Towards the edge of the lens the beam may focus tighter, preventing a single focal point forming. This effect can be caused by anisotropic field strengths within the lens and is known as spherical aberration. The disk of least confusion is the point at which the tightest accumulative "focus" lies.

When a specimen under the beam is tilted and a large area is examined, the regions at extremes of the frame which lie at different heights may be out of focus. In order to compensate for this, modern SEMs have a dynamic focus function which approximates this difference and adjusts the conditions accordingly.

One final effect to mention is the Fraunhofer diffraction that occurs at the diaphragms in objective lenses, causing airy disc formation at the focal length.

Scanning and Blanking

To form an image, the beam is scanned in a raster and the signal of choice at each pixel recorded. The scanning is typically controlled by two pairs of magnetic coils, each controlling a single axis. Magnification is also defined by the angles of deflection incurred here. The angle of incidence can also be changed by rocking the beam, which is extremely useful for diffraction based techniques such as electron channeling contrast imaging (ECCI). [149]

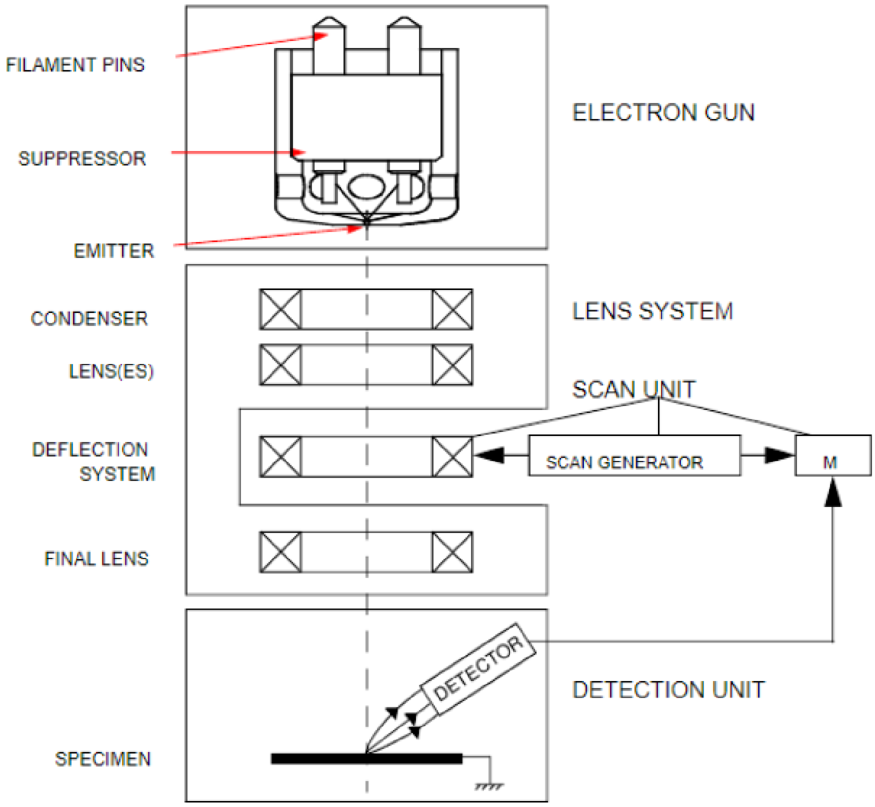

Figure 3.2: **Schematic of a FEI Quanta 250 (one of our microscopes) from the FEI manual.** Here you can see the various stages in the microscope.

Beam blanking is similar to scanning as it relies on deviating the beam away from the emitting path with the use of applied fields. This can be done by biasing the Wehnelt or alternatively by deflecting the beam across an aperture. Beam blanking can also be done periodically to chop the beam with frequency limitations imposed by self inductance in the coils or capacitance. This can allow for certain time resolved or stroboscopic measurements to be done with the addition of other tools such as a lock-in amplifier to separate signals. [150]

3.2 Interaction

When a primary electron hits a semiconductor, multiple processes are set in motion, a selection of which can be seen in Figure 3.3. As an electron navigates a material it will undergo multiple elastic and inelastic scattering events, transferring some of its energy and progressively slowing before halting or exiting the material. By changing the acceleration voltage (and hence energy) of the primary electrons, we can modify these volumes, enabling depth resolved measurements with variable penetration depths or increase the spatial resolution by optimising the excitation spread. [151] Figures such as the aforementioned 3.3 do fail to capture the true complexity of the mechanisms at play, where effects such as self absorption of photons and diffusion of carriers significantly change the information volumes. They do however demonstrate the idea of excitation volumes and how they are different for each process.

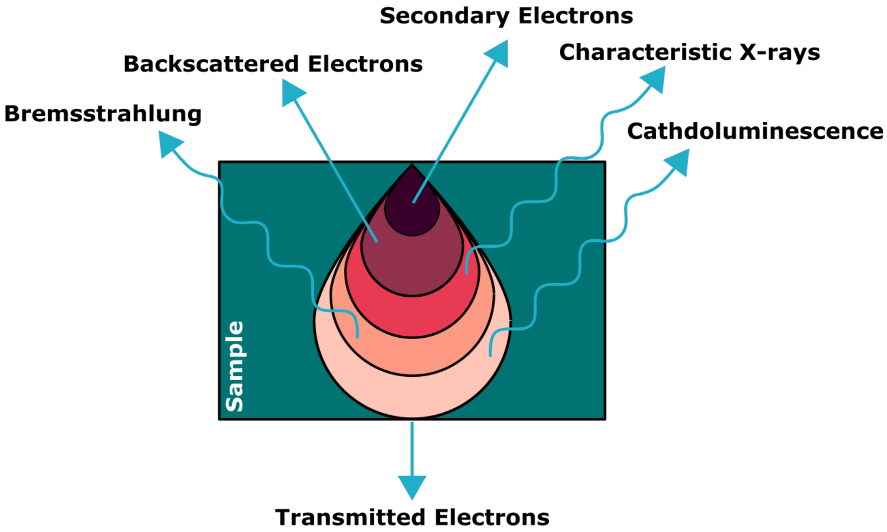

Figure 3.3: **Depiction showing information volumes for a selection of processes that may occur during electron beam-material interactions.**

Secondary Electrons (SE)

Of the thousands of electrons liberated within a specimen under electron beam excitation, only those with energies below (50eV) are considered to be secondary electrons (SE). The majority of secondary electrons are generated through a cascade of inelastic and elastic scattering events as well as plasmon decay. [152] Due to their relatively low kinetic energy, they will struggle to escape when generated deep within a material, and for this reason we only observe those generated near the surface, with enough energy to escape the barrier.

There are three commonly discussed subclasses of secondary electrons: SE1 are generated from the primary electron beam; SE2 are generated just below the surface of the sample by backscattered electrons; SE3 are generated at the walls of the chamber from backscattered electrons (BSE). [153]

SE contrast is cultivated through a myriad of interconnected mechanisms. Topographic features will be observed due to excitation differences, escape efficiency (edge effect) and the directional dependencies of detectors. The crystallographic and Z-contrast of backscattered electrons can be inherited by the SEs they generate, giving compositional and structural information. Voltage contrast can also be observed due to doping and variations in charging. [154] This is particularly useful when examining structures such as pn-junctions, where it is suggested that differences in the escape barrier height between the n and p regions cause the observed contrast. [155, 156] Similar effects can be seen with variations in work function across a specimen. [157] The final effect I will mention in this non-exhaustive list is the contrast produced by internal, external and surface magnetic fields. [158]

SEs are typically collected by an Everhart-Thornley detector (ETD) [144] and form one of the most standard imaging channels in a modern SEM. This particular detector consists of a scintillator paired with a photomultiplier which is encapsulated by a Faraday cage and will collect a mixture of SE1, SE2 and SE3 type electrons. The cage can be biased to enhance collection by pulling in lower energy electrons, or repel them and isolate high energy collection only. Alternatively an in-lens detector can be used which favours SE1 electrons. Such detectors are less sensitive to changes in morphology but can reach higher resolution, operating at shorter working distances. When operating in low vacuum, ETD detectors can no longer function due to the high voltages on the detector and instead gaseous SE detectors (GSED) are utilised. In these detectors the ionisation of the gas itself produces the signal. The pressure and gas species within the chamber therefore become a highly important parameter for optimised operation. [159]

Backscattered Electrons

An alternative imaging channel captures the backscattered electrons (BSE). These are higher energy electrons, and as such travel in straighter paths which can better capture topographical information. However, the larger excitation volume can lower spatial resolution.

A larger nucleus in a specimen increases the probability of electron scattering collisions, producing a strong correlation between atomic number and BSE imaging contrast. This allows for the extraction of some compositional data from such images and is referred to as "Z-contrast". The diffraction of these electrons either on their way in or out of a crystal gives crystallographic information and will be discussed shortly in electron channeling contrast imaging and electron backscatter diffraction sections. As previously mentioned each BSE can generate multiple SEs (SE2), and in doing so their compositional and crystallographic information will be transferred to their progeny.

BSEs can be measured with a quadrant silicon detector which allows for an improved topographic imaging mode. In this detector incident BSEs generate e-h pairs in doped Si and a current can be measured proportional to the number of BSE hitting the detector.

X-ray Analysis

Ejection of a core electron leads to the formation of a highly unstable hole (10^{-15}s). [160] Subsequent relaxation of an outer shell electron via an Auger or fluorescence process produces characteristic radiation which we can then analyse. [161] Here, we focus on the X-ray emission, which is unique to the elemental species and internal transition that transpired. Hence, by monitoring the X-ray spectrum we can identify the elemental composition of our sample. There are two methods we utilise for analysing these X-rays: wavelength dispersive X-ray (WDX) and energy dispersive X-ray (EDX) analysis. Although these methods measure the same radiation, they do so in different manners, leading to advantages and disadvantages of each. In both cases, a minimum acceleration voltage will be required to trigger the transitions of interest. [162]

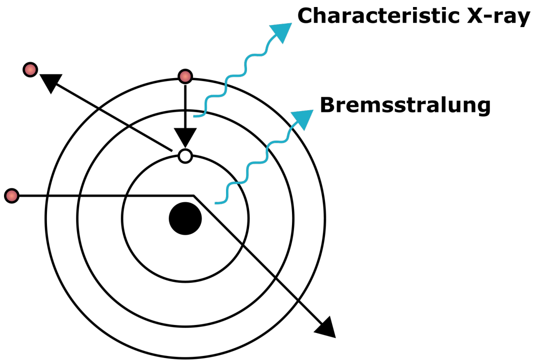

Figure 3.4: **Two examples of X-ray radiation from an atom.** The Bremsstralung radiation is emitted when a passing electron is deflected by the positively charged nucleus. Characteristic radiation arises when a core electron is ejected following a collision and an outer electron relaxes, emitting an X-ray in the process.

Energy Dispersive X-ray Analysis (EDX)

In energy dispersive X-ray analysis, we measure the entire X-ray spectrum, enabling all elemental peaks to contribute and potentially be identified. On these spectra the characteristic X-ray peaks will be overlaid on a continuum background known as the Bremsstrahlung. This is the braking radiation emitted when electrons are slowed or redirected. The form of this broad hump shifts in relation to charging and can be a useful parameter to monitor.

To measure the X-ray spectrum a silicon drift detector is used. In this detector an incident X-ray generates an electron cloud with a charge proportional to its energy. A bias is applied, drawing the electrons to an anode where the charge can be measured. A pulse processor then takes the electronic output of the detector and calculates the energy of the detector X-rays. Increasing the processing time here can help to improve spectral resolution, but peak overlap can still be a problem. Using the scan of a microscope we can map the X-ray spectra of a specimen to investigate elemental and compositional variations across a surface, with spatial resolution likely limited by the minimum acceleration voltages and currents. The standard approach to Quantatative EDX involves comparison between the peak heights of the specimen and a standard of known composition. [163] Standardless methods are possible, but have reduced accuracy and reliability. This approach relies on stored libraries of known values under specific experimental conditions called “remote standards” to estimate the composition in the specimen. [164]

Wavelength Dispersive X-ray Analysis (WDX)

Wavelength dispersive X-ray (WDX) analysis is an alternative approach to detecting and analysing X-ray radiation. It has superior spectral resolution to EDX and is therefore less susceptible to overlap problems, but typically takes longer to measure. In WDX we do not measure the entire X-ray spectrum at each point, instead X-ray spectrometers investigate specific windows of the spectrum. This allows for very sensitive measurements on specific transitions, but will not give a full elemental description of a specimen.

There are many different X-ray spectrometers based on Bragg reflections (Von Hamos, Johann or Johansson) or transmission (Laue-type) each with their own benefits and shortcomings. [165] Here I describe only the reflection type in detail, as that is what is used in measurements shown later.

For a reflection type spectrometer, a single crystal with a specific lattice spacing reflects a single specific wavelength as described by Bragg’s law.

$$2d \sin \theta_B = n\lambda_x \tag{3.10}$$

Where d is the lattice spacing, θ_B is the angle of incidence, n is the diffraction order and λ_x the wavelength of the X-ray involved.

When an X ray of a specific wavelength hits a crystal, it can pass onto the detector via a Bragg reflection. This relation also shows that by changing the angle we can tune the system to select the wavelength of interest. However, this also forces us to change the angle of collection, and so the entire system must evolve around a Rowland circle in order to remain functional.

There is a limited range of wavelengths a crystal can inspect. For this reason in our system, multiple crystals such as thallium acid phthalate (TAP) and pentaerythritol (PET) each with different lattice spacings are stored in turrets to allow for easy exchange.

X-ray detection is performed by gas proportional sensors, three of our four have a constant flow of P10 gas (90% argon and 10% methane). The fourth has a sealed xenon cell which is useful for measuring low energy X-rays. The incident X-rays ionise the medium, generating free electrons which can be collected by a potential in the sensor.

WDX can be quantitative when used with a standard of known composition for comparison and some “ZAF” correction. The Z correction contains two components, the first is the Bethe stopping power of the material and the second is the backscattering coefficient. Due to generated X-rays being absorbed (A) by the material there will be an attenuation of signals which must also be accounted for. The self absorption of energy can also result in fluorescence (F) processes which can change the ratios detected.

This technique is typically performed in a specialist piece of equipment known as the electron probe microanalyser (EPMA), but can be done in a SEM with the required spectrometers and detectors. When using WDX in an EPMA trace elements can be detected at around 10 parts per million ($\approx 10^{18} cm^{-3}$), depending on the element and sample in question. [166] Beyond that, destructive techniques such as secondary ion mass spectroscopy would likely be required. [167]

Cathodoluminescence (CL)

Through inelastic scattering a high energy primary electron can create thousands of electron-hole pairs. If carriers recombine, relaxation energy will be released either radiatively and/or non-radiatively. In the radiative case, the photons emitted can be collected and carry a wealth of information on the specimen’s composition, defect population, strain, carrier dynamics and more. [168] Variants on this technique such as temperature dependant cathodoluminescence (TDCL), time resolved CL (TRCL) or polarisation resolved CL can help to extract even more information. [169]

Cathodoluminescence has certain advantages over other luminescence spectroscopy methods. For example, the large energy of the primary electrons can excite wide-bandgap semiconductors such as AlN and Ga_2O_3 with ease. Another advantage is the small probe sizes possible with both SEM and TEM enabling high spatial measurements to be done. In such electron microscopes it is also possible to carry out complementary techniques simultaneously, allowing for easier interpretation of the spectral information. Scanning of the electron beam allows for spectra to be recorded at each point of the scan and hyperspectral maps to be produced.

Electron Beam Absorbed Current (EBAC)/ Specimen Current

SEM specimens are commonly connected to ground to prevent charging. By measuring the current that travels this path we can extract a quantity known as the “specimen current” or electron beam absorbed current (EBAC). The intensity of the EBAC will reflect the conductivity of a specimen between the excitation spot and the contact point. The current may not exceed the probe current and losses will occur due to SE and BSE emission. EBAC is the simplest of the “charge collection measurements” and is commonly used to detect open circuit failures in ICs [170]. Mapping the EBAC signal can reveal conductive lines at various depths within a sample. Breaks or “opens” in these lines will be visible as little current will be able to flow beyond the broken point. The specimen current can also reveal material inhomogeneity and crystal diffraction patterns. [171]

Restive contrast imaging (RCI)

Restive contrast imaging (RCI) is a related charge collection technique also known as "two probe EBAC" or "remote EBIC (REBIC)". Here, a second contact is made to earth, giving an alternative path for charge to escape. This results in the specimen acting as a current divider between the two points. [172] RCI is commonly employed in the failure analysis of integrated circuits, where the beam conditions are carefully tuned to ensure the excitation volume includes buried metallic contact rails. [173] Breaks or shorts in these rails can then be identified from the changes in contrast. The technique can also be used to study defects within a material such as grain boundaries, which strongly influence the electrical properties in local regions. [174] Materials with homogeneous resistivity will show an intensity gradient radiating from the probe which is measuring. [175]

Electron Beam Induced Current (EBIC)

A specific form of EBAC is known as the "electron beam induced current" (EBIC). [176] This only occurs in materials or devices with built in fields large enough to produce electron gain effects such as p-n junctions or Schottky diodes. Following electron and hole generation by the primary beam, the carriers may not recombine at all, with internal and/or applied fields separating carriers and creating a flow of charge which we can then measure, this is referred to as the EBIC. EBIC signals can be thousands/hundreds times larger than EBAC due to this gain effect.

By mapping the EBIC using the raster of the microscope, we gain insight into the carrier dynamics of the material and can extract many parameters such as the diffusion length, surface recombination rate as well as junction dimensions and location. Contrast in such a map is also generated by changes in doping, composition or crystal structure. EBIC is measured through a low current, low impedance amplifier, and the microscope scan rate will need to be harmonious with the sensitivity.

Electron Beam Induced Voltage (EBIV)

When using a low impedance circuit, EBIC reflects the short circuit current (I_{sc}). By adding in and increasing the resistance we slide down the IV curve towards the open circuit voltage (V_{oc}). By using an infinite resistance voltmeter, we can measure what is known as the electron beam induced voltage (EBIV) also known as voltage distribution contrast. [177]

Electron Beam Induced Resistance Change (EBIRCH)

Another charge collection variation is known as β-conductivity measurement.[178] In these measurements either a constant current or bias is applied to the material in question. If an applied voltage is kept constant, a scanning electron beam will modulate the collected current by generating carriers within the excitation volume which will increase the conductivity. Alternatively, a constant current can be applied and variations in voltage measured. In this manner local variations in resistivity can be found. [172] For this reason these measurements are often also called electron beam induced resistance change (EBIRCH) studies. [175]

Current Imaging (CI)

For this technique, the beam is only required for target identification and navigation. The measurement itself is done using only a nanoprobe tip, which is biased then brushed/scanned across the sample to map current. For this entire process the beam can be blanked, reducing contamination and potential sample damage. [179]

Electron Backscattered Diffraction (EBSD)

Following excitation by a primary electron beam, generated electrons can diffract on their path out of a crystal producing distinctive patterns. [180] These patterns consist of overlapping Kikuchi bands, corresponding to each set of lattice planes, allowing us to identify phases and orientations and map them across a surface. Both positional and intensity variations can be measured indicating different phases and orientations. To perform these measurements the sample is typically tilted at 70° to the beam and electrons are scattered onto the detector. [181] This detector normally contains a phosphor screen which generates light when electrons strike, and this light is then imaged by a CCD. Direct electron detectors can alternatively be used.

Electron Channeling Contrast Imaging (ECCI)

Electron channeling contrast imaging (ECCI) can be performed when the incident electrons diffract into and through an appropriately orientated crystal, with small changes in strain and crystal orientation creating contrast in the backscattered signal (can be imposed on SE also). [182] Due to this, the technique is ideal for identifying extended defect types and densities, as well as grain boundaries and atomic steps. An electron channeling pattern (ECP) can be acquired at low magnifications where the change in angle of the incident electron beam can help identify the lattice planes responsible for the contrast observed. Importantly this technique can be considered non-destructive due to being compatible with bulk samples, unlike TEM based methods which require electron transparent specimens to be prepared. [183]

3.2.1 Detrimental Electron-Matter Interactions

Charging

Exciting a material of insufficient conductivity with an electron beam may result in a build up of charge. Each primary electron can mobilise thousands of secondaries and can potentially lead to large charge disparities.

Samples are commonly mounted on metal stubs with conductive silver paint, and through the grounded microscope stage charge, can find a path to earth. In situations where this is not possible or effective, a wire may be bonded or metal probe may be used to discharge the sample. Low vacuum (LVSEM) or environmental (ESEM) conditions should also help to reduce charging but may cause other unwanted effects. A common method to reduce charging involves coating the sample in a highly conductive layer: gold, platinum and chromium all have suitable grain sizes. However, this layer can obscure details and attenuate signal channels through absorption.

Charging can result in strong, dynamic and highly irregular electric fields within, without and along the surface of a specimen. These fields will deviate any charged particle within their reach, causing image distortions in both contrast and form. Lower energy secondary electrons will be more susceptible to the field and for this reason BSE detectors show superior imaging of charging samples. In extreme cases, the charge build up is so significant that the electric field at the surface becomes larger than the energy of the primary electron, reflecting it back into the chamber. The resultant image is then that of the chamber itself. This so called ”electron mirroring” can actually be useful when studying the properties of dielectric materials. [184]

The effects of charging are also particularly problematic in contact dependant processes. Carrying out a pick and place procedure in the midst of a strong electric field is likely impossible, unless the adhesive forces are strong enough to overcome the field. In this case, this likely also means that depositing the object will be very difficult as the object is so strongly bonded to the probe. Violent events may also occur when a sample discharges while being contacting by a metal probe, causing catastrophic damage to both sample and tip, an example of which can be seen in Fig. 3.5 which occurred during my own experimentation.

Damage and Defect Generation

Organic materials are particularly susceptible to electron beam induced damage. The energy provided by the beam can break existing bonds and assist in forming new ones. Of particular importance are the carbon double bonds which enable crosslinking to form polymers. This can be accompanied by the ejection of ions from the sample which can result in the formation of bubbles on the surface. The loss of mass also changes the density of the sample, enabling the beam to penetrate deeper and deeper into the material.

Although generally more resilient to damage, inorganic samples are not immune to the electron beam irradiation and there are many examples showing this. As previously mentioned the revelation of p-type GaN was thanks to electron beam annealing releasing compensating hydrogen from the crystal. [10] An interesting study by Yakimov et al shows the mobility of dislocations in GaN under electron beam excitation. [52] Work by Smeeton et al (controversial at the time) showed the strain introduced in InGaN QW during TEM measurements. [74] The detrimental effect of a high energy electron beam on the oxide layer in integrated circuits has also been well documented. [185]

A significant portion of the beam power will heat the sample. Either directly through trapped electron avalanches or as an secondary effect of processes such as cathodoluminescence where phonons are often generated. The local temperatures achieved can be approximated to be a function of the incident beam power and the thermal conductivity of the sample. The susceptibility and volatility of certain materials with respect to temperature should be kept in mind.

Edge Effect

When examining a rough or three-dimensional specimen, edges may display bright SE contrast relative to the surroundings. This is due to the excitation volume overlapping with the edge of the material resulting in high SE emission from the sidewall. This is known as the edge effect.

Contamination

It is inevitable that samples will be contaminated in SEM. The extent of which will be dictated by variables such as beam conditions, chamber pressures and cleanliness as well as the specimens constitution and history. All materials entering in and around the chamber must also be handled with gloves.

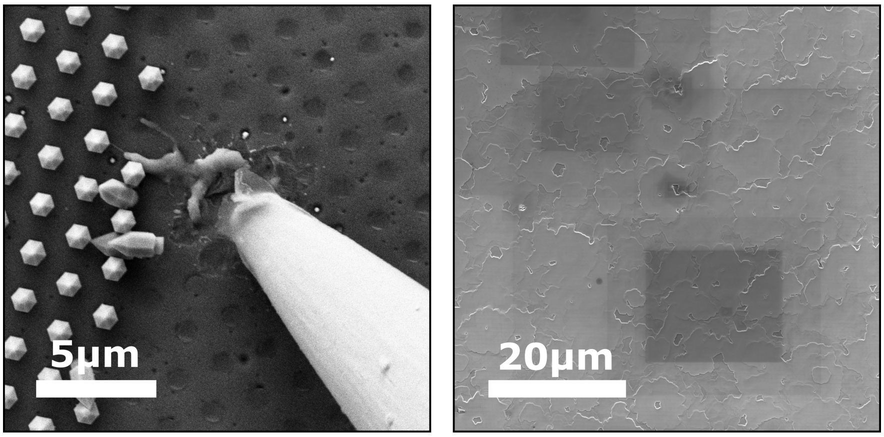

Figure 3.5: **SE images of two detrimental interactions. a,** Aftermath of contacting where discharging has caused calamitous damage. Crater formation in the sample and melting of the tungsten probe tip can both be observed. **b,** The effect of SEM investigations on the surface of *p*-GaN. Multiple dark squares and rectangles of contamination can be seen to apparate following electron beam scanning at various magnifications. The higher magnifications concentrate the beam dose resulting in faster deposition.

Samples that have not been specifically treated and are stored in air will likely already be coated in hydrocarbon molecules. Even in the vacuum chamber of an SEM, hydrocarbons and silicon compounds from grease and oils in the machine will be present. The electron beam provides the energy to break and form new bonds with these atomic and molecular components and this cracking process results in a polymerisation of the hydrocarbons, causing a film to develop when the beam is active. In an SE image this can appear as a dark (or light) patch where the beam has been scanned, although if prolonged exposure occurs and the film becomes thick enough, changes in surface morphology can also be observed. If a point measurement is being performed then stalagmite like features can begin to grow. Measuring the growth rate of such features can indicate how clean the sample/chamber truly are. These stalagmites and films grow quickly due to the high surface mobilities of constituent hydrocarbons. By cooling samples it is possible to lower the mobilities and decrease the rate of contamination, it is also possible to saturate these growth rates at high currents. Cold fingers can be deployed to further reduce contamination by adsorbing contaminants on their surface. Exposing a larger area than is required for imaging or measurements may also help to reduce contamination by reducing the local population of mobile contaminants.

3.2.2 Simulations

Casino

When using any of the aforementioned electron microscopy techniques, It is important to understand what we are actually measuring. The excitation volumes I previously discussed are a function of the acceleration voltage and we can model these volumes them using Monte-Carlo simulations to obtain approximate values. Simulations can also advise optimum beam conditions for measurements, allowing microscopists to target specific layers within a heterostructure or regions in a sample. They can also help to explain aberrant or unexpected observations made during experimentation.

"CASINO" is a free and user friendly family of software designed specifically for this purpose. [186, 187] These ballistic simulations operate as a function of the material densities present in a specimen. The original program has been refined and improved over many years by its creators, delivering fast and fairly accurate simulations in two dimensions. However when working with samples with complex morphologies or nanostructures, the related program "CASINO 3D" is more appropriate. These more advanced simulations are more computationally intense and may require significantly longer run times.

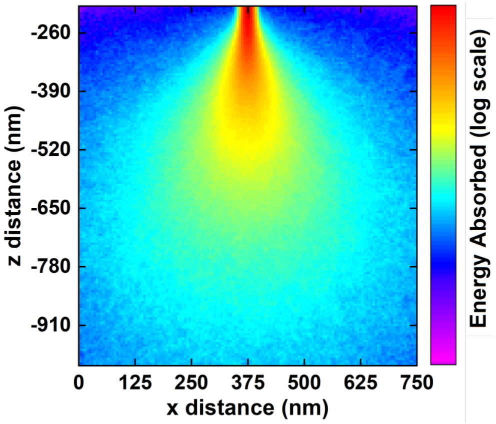

Figure 3.6: **Example of a CASINO simulation on a block of GaN.** We can see the levels of energy deposition at various points of the sample.

CASINO simulations are limited in their accuracy as they do not account for diffusion effects within materials. Recent work by Lähnemann et al [188, 189, 190] compares the excitation volumes predicted by CASINO simulations and experimentally determined values. They find that the experimental CL intensity profiles were larger at all temperatures than were predicted by the simulations. This lead into interesting discussion of the mechanisms of both CL and the general diffusion of carriers in a QW structure. They find that electron-phonon scattering reduces the generation volume and hence at lower temperatures the volume increases. This however contradicts work by Solowan [191] and Weatherly et al [138] demonstrating the complexities of diffusion.

3.2.3 Experimental Setups

FEI Quanta 250 FEG

The FEI Quanta 250 FEG is my electron microscopy multitool. It can be equipped with an array of detectors allowing for simultaneous and complementary measurements to be performed.

This machine is capable of measuring SE, BSE/forward scattered electrons (FSE), CL, EBSD, ECCI, EDX, housing a nanoprobing system and has low vacuum (0.1→3mbar) capabilities. Low vacuum SEM or environmental SEM as previously mentioned may be necessary when working with charging materials. For this reason many instruments over time have congregated on this particular machine.

Some of these techniques can be performed simultaneously such as EBIC and CL mappings. Others would require multiple measurements due to experimental limitations. For example the EBSD and CL detectors are on opposite sides of the chamber and normally require a sample tilted towards them.

Our home-built CL system collects light perpendicular to the beam through a reflecting objective. The light is then fed into a f/4 spectrometer with exchangeable gratings and slits which project into a cooled electron multiplying CCD. [192, 193] These parameters define the maximum field of view of the light collection. The "Chimp" software written by P. R. Edwards controls both the beam scan and data acquisition, and with hyperspectral mapping we can record a spectrum at each pixel of the scan. "Chimp" also contains some analysis tools such as peak fitting, principal component analysis [194] and cross correlation examination. [195]

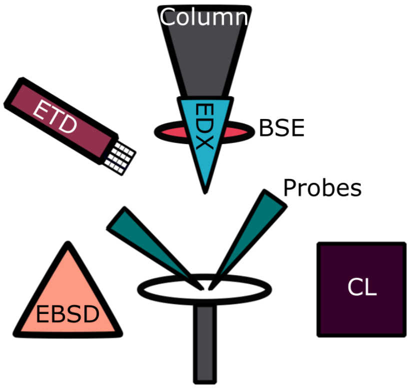

Figure 3.7: Schematic showing the chamber of our FEI Quanta 250 FEG SEM, including SE, BSE, EDX, CL, NP and EBSD detectors.

FEI Sirion 200 FEG

Thanks to having the same chamber as our FEI Quanta, many of the tools compatible with that machine can be attached to the FEI Sirion 200 FEG. The disadvantage of this microscope being the lack of low vacuum capabilities and potential problems with transporting and installing sensitive equipment. The Sirion does have some advantages over its younger sibling, such as its semi-in-Lens detector which in theory can allow for higher resolution imaging than is possible with the Quanta. The Sirion is also equipped with some home built and experimental detectors for diffraction based techniques.

JEOL Electron Probe Microanalyser

This machine serves two major purposes, accurate compositional analysis and large area cathodoluminescence mappings. It is equipped with four WDX spectrometers allowing for four possible elements to be mapped or quantified simultaneously. There is a caveat, in that each arm only has a certain selection of crystals limiting the operational capabilities of each arm. I list the crystals stored in each of the four turrets in Table 3.1

This machine is also exceptional for large scale cathdoluminescence mapping, with the high accuracy and precision of the stage, large area scans can be done using the stage while keeping the beam centered and using drift correction software. Although, some optical components in this system currently absorb in the UV limiting its operation. The EPMA also places greater emphasis on beam stability and monitoring compaired to standard SEMs.

Port Number	1	2	3	4
Crystal 1	TAPH	LDE1L	PETJ	PETHS
Crystal 2	LDE2H	TAPL	TAPJ	LIFHS

Table 3.1: List of the four EPMA arms and their respective crystals.

3.3 Transmission Electron Microscopy (TEM)

Although I did not practice transmission electron microscopy (TEM) myself, the work done by collaborators using this technique became pivotal to understanding the behaviour of nanostructures discussed in Chapter 4. and in the investigation of defects in planar AlGaN LEDs in Chapter 5. For this reason I briefly introduce transmission electron microscopy operation in order to give context and understand the data shown.

Although transmission electron microscopy is possible with samples that are electron transparent in a standard SEM with appropriate detectors in place, transmission electron microscopes designed specifically for this purpose can far exceed their capabilities thanks to significantly higher acceleration voltages, additional lenses and advanced aberration correction. [196] These transmission electron microscopes can apply similar techniques to SEM such as CL and EDX, but can do so on far smaller scales with images on the scale of nanometers commonplace. This approach also opens the door to new TEM specific techniques not possible in an SEM. Imaging with atomic resolution is possible with high resolution TEM (HRTEM).

TEM is excellent for investigating small regions but it can be difficult to say whether what is observed remains true across an entire sample. The destructive sample preparation necessary can also be a problem. [197]

3.4 Focussed Ion Beam (FIB)

Our collaborators use a focussed ion beam - SEM (FIB-SEM) which has the imaging advantages of a SEM (less damage than FIB, greater resolution and the usual SEM contrast mechanisms [198]) allowing for easy navigation and identification of regions of interest, while retaining the FIB capabilities.

A FIB-SEM has the ability to either mill or deposit conducting or insulating materials such as tungsten, platinum or carbon. My collaborators have used both of these functions in our work to create electron transparent sections from large samples, etch through layers in a heterostructure and to deposit metal contacts on nanostructures.

Deposition begins with the introduction of organometallic gas species which can adsorb on the surface. Subsequent interaction with the ion beam results in standing bonds breaking and new bond being made, with further adsorption resulting in the growth of material in the desired area. [199] This process is capable of producing complex structures and patterns on the nanometer scale. [200]

Milling occurs when the incident ions provide enough energy to the atoms in the specimen to overcome their surface binding energies. During this process some ions will be implanted, while a greater number are ejected along with secondary electrons.

3.5 Nanoprobing

In this thesis, nanoprobing is a term used to describe the act of making physical contact to a sample with nanoscale precision within an SEM. The technologies involved in performing such an operation have evolved from the pioneering scanning probe techniques developed in the late 70's and early 80's of scanning tunneling microscopy (STM) and atomic force microscopy (AFM), both of which rely on dictating the position of a fine probe accurately on a surface. [201]

It could be said that the first nanomanipulation experiments were carried out inside of scanning tunneling microscopes (STM), where molecules and single atoms could be manipulated and positioned at the behest of man. [202, 203] Performing probing experiments inside an STM has some shortcomings; due to the images being formed by the raster scan of a needle, it is not possible to both image and manipulate a structure simultaneously in a STM system. This in conjunction with the specific operating conditions STM normally requires and the scales over which they operate, restricts the applications of STM based nanomaniupulation. AFM similarly to STM, is hamstrung by the inconvenience of requiring the needle for observation. This of course has not stopped experiments demonstrating suitable applications for the technique. [204]

Dynamic electrical probing can be done under an optical microscope, but the resolution of the microscope will be a limiting factor to the size of structures examinable and repeatability of measurements. Alternatively electrical characterisation can be done with wirebonded or deposited contacts which are static connections.

The precision and stability of modern probing systems is possible thanks to piezoelectric crystals, which by definition, have the useful property of deforming under an applied bias. These crystals can be integrated into motors or actuators allowing for deterministic motions on sub nanometer length scales. It is therefore natural to integrate such devices into scanning electron microscopes, where we can observe such fine motions in real time. On such small scales vibrations must be limited and most commercial nanomanipulation setups combat this problem well through damping and shortening of limbs. The large field of view, depth of field and range of magnifications possible in an SEM all add the flexibility of this combination. Another major benefit, is in the ability to manipulate structures under live observation. The electron based imaging also enables other techniques not possible in optical systems such as electron beam induced currents. (OBIC is possible but a distinctive technique in its own right)

The development of SEM based nanomanipulators has facilitated interactive and dynamic experimentation on the smallest of scales and has found particularly strong applications in the examination of semiconductor materials and devices. Inside an SEM, the small metal needles provide much needed dexterity and tactility, analogous to the lumps of meat and bone we call hands, enabling rapid characterisation of the electrical, mechanical and optical properties of nanostructured materials as well as the creation of novel device architectures and experimental configurations. [205, 206]

Within a FIB-SEM, probes are also now used regularly in TEM sample processing, where they can extract thin lamella and mount them on grids. However, the small specimen chambers and relative complexity of operation has limited the use of nanoprobing systems inside the TEM itself to more niche procedures. [207, 208]

The motivation within my group for acquiring such a setup was to enable effective electrical characterisation of semiconductor nanostructures without additional and restrictive processing steps and also to explore elastomeric polymer deformation.

3.5.1 Kleindiek Nanoprobe System

My research group recently acquired a pair of Kleindiek MM3A nanomanipulators, with an example setup shown in Fig. 3.8. The base MM3A system has two rotational axis and a third prismatic axis. The "x" and z axis are equivalent in performance and have a minimum 0.5nm step size. The "y" axis is driven and retracted via a prismatic joint and thanks to this, has a finer resolution of (0.2 nm). The different joints also result in differing limits in terms of fine ranges of motion.

Figure 3.8: **Photograph of an example two probe configuration located in our FEI Quanta 250.** Here you also see the triaxial cables for our low current measurements.

The rotational movement of the manipulator in the x/y and z axes result in quasi-Cartesian motion on small scales which can be controlled through the use of a remapped PlayStation "joypad" controller. The probes can alternatively be steered via their control boxes however the joypad controller is far more intuitive and once comfortable, operators can perform complex tasks in rapid times (I transplanted 16 nanorods in a single day). The low drift (approx 1nm/min) and low vibrational susceptibility of our system is ideal for the particular applications we have in mind, which requires contacting small features for extended periods of time.

In order for the manipulators to function effectively the amplitude of the bias applied to each piezo may need to be adjusted. To find the optimal value I vary the bias between 1-80V until I find the minimum bias required to step the motor. If the amplitude of the bias has not been tuned well the coarse movement can become erratic.

Another parameter that may need fine tuning is the reversal correction. Due to a accumulation of mechanical tension, if I change direction on one of the axis, the initial coarse steps will be larger than intended. This parameter deliberately lowers the first few step sizes by reducing the bias applied to the piezo to compensate.

3.6 Operation

I begin operation by mapping the axis via the control box to match the probe configuration in the chamber. A typical mapping can be seen in Fig. 3.9. This is done to avoid any unintentional crashes from user error. Manipulators are mounted in a custom made plate with multiple possible mounting positions that attaches to the microscope stage. This means any stage tilt also tilts the probes. I use coarse, high speed adjustments to move the probes roughly into the center of the microscope's field of view with zero beamshift. Then, ensuring the probes remain

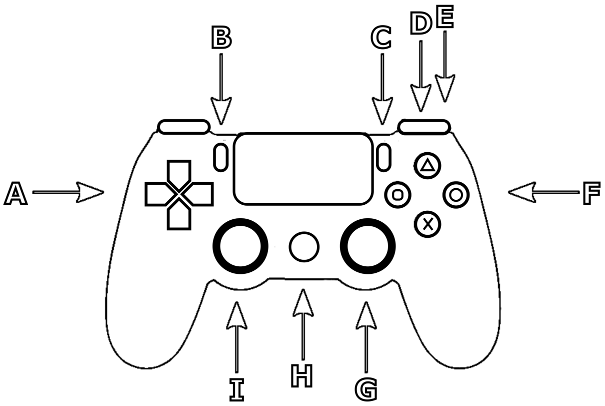

Figure 3.9: **Example joypad mapping for probe operation.** (A) X/Y step. (B) Slow speed. (C) Increase speed). (D)/(E) Probe Switch. (F) Z step. (G) Analogue Z. (H) Safety. (I) Analogue X/Y.

a safe distance from the sample, I move the microscope stage to bring the area of interest on the sample to the centre. This becomes more challenging when the sample is tilted.

I use the working distance of the microscope to continuously assess the height of both the probe tips and sample as I descend upon the target. The directional dependence of the Everhart-Thornley detector (ETD) means that if I position the probes appropriately, shadowing will appear as the tips near the sample surface as can be seen in fig. 3.10. The shadowing is the simplest indicator of probe proximity to the sample surface. Unfortunately when in our luminescence collection configuration, shadowing will not be present due to the tilted sample surface. Instead it is possible (depending on the constitution of the surface) to observe a small local brightening of the sample as we near the surface with the probes. This effect only occurs when in very close proximity and demands a cautious landing. This brightening likely occurs due to electrons both scattering from the sample face then scattering once again off the tip.

While descending to a surface I have also observed charge related changes in contrast, such as a full frame darkening upon approach and a brightening upon contact or vice versa. However, contacting a charged surface is generally a bad idea unless discharging is intentional, as electrical discharging can be violent and destroy both tips and specimens alike. This effect depends entirely on the samples constitution and preparation.

A sure sign of contact will be a tip sliding across the surface. However, this could cause unintentional damage to both tip and sample and cannot really be seen when contacting something like a nanowire, although in this case the structure itself can be seen to move under contact. Alternatively, when performing electrical measurements I can monitor the strength of a signal that is very dependent on the amount of separation or contact.

As previously discussed the CL/EL measurements typically involve a sample pretilted at 45° relative to the beam for optimal light collection. The variable sample height caused by a pretilted stub (not stage) requires careful operation and the tilt away from the ETD can also lower SE image quality obscuring visibility.

I typically carry out the final approach in a fine movement mode to ensure both sample and tip survive the mechanical impact. It should be said there are circumstances where it can be useful to aggressively contact a surface, such as to penetrate or scrape off any oxide or contaminated layers which could improve the electrical contact.

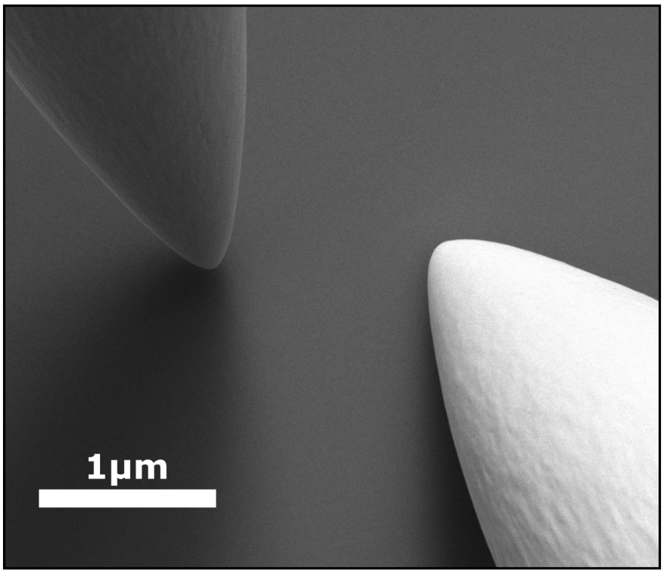

Figure 3.10: **SE image showing two large probes on a GaN surface displaying the directionality of shadowing.** I can use this to assess the distance between tip and sample.

Many commercial setups feature alternative methods of approaching a surface safely (a luxury we do not have). The Kleindiek safetip approach essentially performs continuous low voltage IV sweeps and detects a change upon contact. A Klocke system may contain a built in MEMS device which senses a change in the resonance of the tip due to surface potentials in the near contact regime.

In addition to the obvious electrical experiments possible with probes, I can also measure the forces applied by their pressure. Our force measurement system relies on some simple physics combined with high precision measurements. I mount samples on a spring table with a known spring constant, apply a force to the object using a nanomanipulator and the spring will bend proportional to its spring constant. We record a video or series of images of this process and then through Hooke's law I can calculate the force being applied. To extract a force-distance or force-time curve, I use software that tracks features in each frame in the series and notes their position and converts this displacement to a force.

Chapter 4

Nanorods

The work in this chapter would not be possible without my collaborators. Dr. Tim Wernicke and his colleagues at the Technical University of Berlin in the group of Prof. Michael Kneissl provided high quality AlN and AlGaN templates which act as our starting materials. The nanostructuring and subsequent overgrowth was carried out at the University of Bath by Dr. Pierre-Marie Coulon and Dr. Philip Shields. Transmission electron microscopy and focused ion beam work was done by Dr. Simon Fairclough within the group of Prof. Rachel Oliver at the University of Cambridge. With Dr. Gunnar Kusch from this same group I spent a week measuring low-temperature and time-resolved CL on their system. I performed the electrical and RTCL measurements at Strathclyde.

4.1 Introduction

Over the past few decades III-nitride LEDs have revolutionised visible lighting, forming remarkably efficient and compact devices. However, the material system offers further potential, including tuneable emission from the infrared through to the deep ultraviolet (UV). [209, 3] UV light emitters have a multitude of motivating applications such as water purification [4], skin-safe disinfection [210, 211] and the curing of resins [212]. By increasing the AlN content in our LEDs we open a pathway to deep UV emission (down to 205nm), but performance is currently hampered by an array of deleterious compounding factors.

Conventional nitride LEDs are grown as polar *c*-plane layers, in the stable wurtzite crystal structure. The resulting quantum wells contain a high degree of spontaneous and piezoelectric polarisation and through the quantum confined Stark effect (QCSE), these strong electric fields separate electron and hole wave functions and lower the recombination efficiency. [213] The QCSE can also cause a significant red-shift in emission, which is particularly problematic when growing short wavelength emitters. The growth of nanostructures such as nanorods allows for active regions to instead be deposited radially on non-polar m or a-planes, circumventing the QCSE and improving internal quantum efficiency. [214]

Core-shell nanorods (where some core has been encapsulated by subsequent layers) will also have greater quantum well and junction areas relative to footprint and this can improve current spreading and reduce the efficiency droop at high current densities. [215, 32, 216] The larger surface area of a nanorod may additionally lead to lower strain due to the increased free surface. [217, 218]

The geometry offers further potential advantages in regards to doping. The high activation energy and hence low hole density of Mg-dopants in AlN consistently results in the poor conductivity of p-AlN or p-AlGaN. For this reason p-GaN contact layers are commonly used in UV LED structures resulting in the counterproductive absorption of light generated in the active regions. Core-shell structures may help alleviate this problem and avoid the use of GaN thanks to surface doping enhancement. [219] The lower strain present in the nanowire has been shown to increase Si dopant solubility limit beyond expected values. [220] In the case of Mg doping, a hydrogen assisted mechanism can result in improved incorporation on the m-plane under certain growth conditions. [221, 222]

Heteroepixtaially grown material with a high AlN content also typically displays significant densities of threading dislocations which can cause current leakage and/or act as non-radiative recombination centres. [223] Nanowires created through both top-down etching and bottom-up growth methods have been shown to reduce threading dislocation densities through filtering and bending. [224, 225, 226, 227, 228, 229]

GaN and AlN have two distinct anisotropic valence band structures due to differences in crystal field splitting. This affects the optical polarisation from AlGaN quantum wells, with AlN rich alloys having strong emission perpendicular to the c-axis. Light extraction from the top surface of c-plane quantum wells therefore becomes problematic. Although with m-plane AlGaN on AlGaN quantum wells the polarisation of emission will also be perpendicular to the c-axis [129], with nanorods the light can escape the surface with greater ease and even be preferentially redirected along the c-direction with some specific configuration of the array (e.g pitch, height and diameter). [230, 231]

To unlock the full potential of such technology, advanced production techniques must be adopted to create regular and well-defined nanostructures. Whereas the selective area growth of GaN nanorod arrays and the subsequent growth of InGaN shells has already been demonstrated by MOVPE [232, 233], such growth of AlN and AlGaN rods remains elusive due to the very high sticking coefficient and the low diffusion length of Al atoms.

Currently most AlGaN nanorods are grown by molecular beam epitaxy (MBE), which possesses a limited throughput in comparison to metal organic vapour phase epitaxy (MOVPE). Furthermore, MBE AlGaN-based nanorods require a GaN pedestal grown on silicon to initiate their nucleation. The bandgaps of these materials result in the detrimental absorption of UVB/UVC light. A solution to this problem is the combination of top-down etching of planar materials to form a uniform array of nanorod cores followed by MOVPE overgrowth of the active material. [234] This approach combines the benefits of conventional core-shell structures whilst introducing flexibility. The core material can be formed from a range of 2D planar materials and the configuration of the nanorod array can be tuned through advanced patterning techniques and controlled top-down etching. With this hybrid approach, my collaborators recently demonstrated the synthesis of highly uniform and organized AlN nanorods on sapphire substrates [235] and the successful fabrication of deep UV AlN/AlGaN core-shell structures. [97]

In this chapter I detail how we seek to advance these structures. Due to the increased ionization energy of the Si donor combined with self-compensation effects, AlN is found to be highly resistive. [236] In order to achieve electrical injection, it is necessary to create a n-doped core with a reasonably low resistivity upon which the subsequent shells tack can be grown. Of course we also require a p-type capping layer to form the p-n junction for an electroluminescent device.

The final structure studied combines etched n-AlGaN cores with the MOVPE overgrowth of an AlGaN QW and a p-AlGaN capping layer, all this being obtained on a sapphire substrate. This design should improve lattice matching between layers and allow better light extraction while still maintaining the high conductivity required for an effective electrically driven device. The UV-transparent sapphire substrate also enables backside light extraction, which is impossible with alternative candidates such as GaN or Si [237, 238] which would absorb such short wavelengths

4.2 Core Fabrication

A 3 μm thick n-$Al_{0.76}Ga_{0.24}N$ layer with a Si doping concentration of 2.1×10^{19}cm^{-3} was grown atop a AlN/sapphire template by MOVPE at the Technical University of Berlin (TUB).

This template was then sent to the University of Bath where they deposited a metal mask on the template using a technique known as Talbot displacement lithography. [239] This exploits the Talbot effect by using monochromatic illumination through a grating, exposing a photo resist in a periodic pattern as the sample is moved through one Talbot period. This avoids the typical shallow depth of field associated with the Talbot effect. This technique can produce repeated patterns down to 75-100 nm feature sizes over entire wafers. [240] The resolution is slightly worse than extreme UV or e-beam lithography but is cheaper and faster.

Using an inductively coupled plasma (ICP) etch the surface deposited mask is transferred onto the template, which allows for the subsequent dry and wet etching to produce the core structures in a highly consistent manner with diameters of 210 nm and heights of 1.7 μm. Etching conditions were optimised over a previous set of experiments by my collaborators. [97, 235, 241] This highly flexible technique allows for widths, heights and pitch of the array to be tuned to the desired specifications.

In my SE image of the etched cores shown in Fig. 4.1a some roughness is visible on the their sidewalls. At this early stage this did not seem too concerning, as typically facets are recovered on these cores through an initial metalorganic vapour phase epitaxy (MOVPE) overgrowth stage before depositing any active layers which can be seen in Fig. 4.1b. This step does creates challenges of its own as we will see further in this chapter.

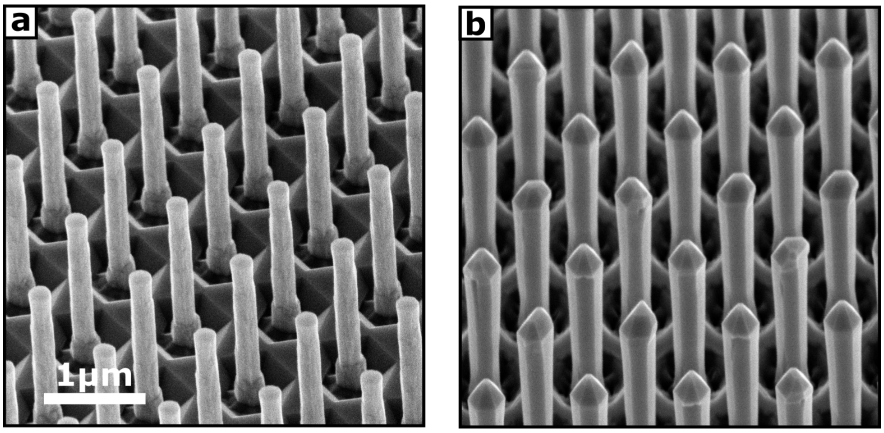

Figure 4.1: **SE images of the etched cores (a) and refaceted structures (b) showing the rod dimensions and surface morphologies.**

4.3 Structural Development

4.3.1 *p*-Contact Layers

Previous iterations of AlGaN core-shell structures grown by my collaborators lacked *p*-type capping layers which are necessary for an electrically driven LED. As an initial step, three different recipes for this capping layer were trialled. The specimens produced were simply refaceted AlN rods capped with a Mg-doped layer with different compositions. The three options explored were p-GaN, p-AlGaN (GaN rich) and p-AlGaN (AlN rich). I examined the three structures through energy dispersive X-ray analysis (EDX) and cathodoluminescence (CL) and looked for differences in their properties.

SE imaging found clear morphological differences between the three. The p-GaN deposition had resulted in the infilling of the etched trenches that typically surround the cores, with very little of the material being deposited on the rod sidewalls. This is confirmed by EDX mapping seen in Fig. 4.2c where we can see the large Ga mounds at the base of the rods. A general lack of faceting is also apparent.

The Ga-rich-AlGaN alloy appeared similar to the p-GaN case, with infilled pits but to a slightly lesser extent and leaving a rough surface texture. The final overgrowth option of an AlN-rich AlGaN alloy had preserved the faceted pit left behind from core etching and appeared to leave a relatively good surface. My EDX measurements found that the AlGaN alloys were deposited on the sidewalls of the rods and not just on the sample "floor", with the high AlN content being the more uniform of the two.

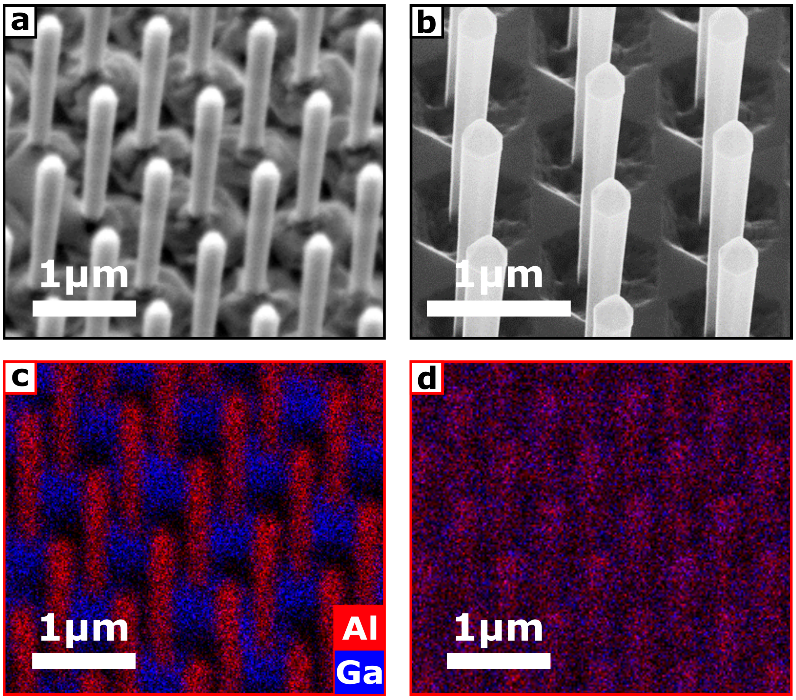

Figure 4.2: **Investigation of p-type capping layers. a,** SE image of the p-GaN capped sample, with clear infilling in the first at the base of the rods. **b,** SE image of the AlN rich p-AlGaN sample with distinct facets still clearly visible on the sample floor as well as the rods themselves. **c,** EDX map of the p-GaN capped sample showing the mounds at the base of the rods to be GaN with little deposition on the rods. **d,** EDX map of the AlN rich p-AlGaN capped sample with far more uniform deposition of the alloy on the rods as intended.

I also acquired CL maps of each of the samples. I had hoped to see band-edge emission from each of the p-layers in addition to the potential luminescence band from the Mg doping; This was not the case. The lack of BE accompanied by significant defect luminescence could indicate a poor crystal quality. Although, highly Mg doped material can lack luminescence and still have excellent electrical properties. The AlN-rich sample did show significantly lower defect luminescence which could indicate an improved product. Due to the adherence to well defined crystal planes combined with the possible light extraction advantages of a more AlN-rich cap, this recipe was used for subsequent experiments.

4.3.2 UV Quantum Wells

Using knowledge gained from the aforementioned experiments in conjunction with previous work by my group and collaborators, Dr. Pierre-Marie Coulon prepaired a systematic series for investigation, with the aim of producing the best UV core-shell structure yet. I received samples with the basic core-shell structure of *n*-AlGaN core, regrowth layer, quantum well/s and a *p*-AlGaN capping layer (seen in Fig. 4.3a). Within this series quantum well compositions, widths and numbers were varied. I was also sent examples of the dry/wet etched cores and rods following the initial facet recovery step for comparison.

The samples with GaN QWs were found to have poor morphologies and no QW luminescence, so were discounted early on. This left the thick AlGaN SQW, thin AlGaN SQW and AlGaN MQW samples. All three were found to have optically active QWs, emitting at similar wavelengths around 300 nm as shown in Fig. 4.5a. This was somewhat surprising given that the thick QW was deposited for over double the time of the thin one, although at this early stage we had no idea how thick or thin these quantum wells really were. The CL intensity from the three samples were found to be of a similar magnitude, but it was not possible to reliably say which specimen had most intense luminescence. This is due to the way that our CL measurements are taken, (alignment and voltage dependant) but we could see which samples had more uniform emission. For this reason I selected the thick AlGaN SQW sample for further more detailed structural, optical and electrical characterisation. The CL spectra seen in Fig. 4.5 is skewed also by the difference in layer thickness affecting the normalisation to band edge, which may make our choice of sample look rather flattering. It is this sample that is described in the following sections.

4.4 Transmission Electron Microscopy

Using a transmission electron microscope and energy dispersive X-ray spectroscopy (EDS) the composition and structure of the nanorods was investigated. Two suitably electron transparent lamellae were prepared using a focused ion beam in order to examine rods in two planes visualised in Fig. 4.3b. The first cut was along the *c*-plane near the top of the nanorods, just below where the semipolar and non-polar facets intersect. The second cut ran the length of the rods along the bisecting *m*-plane.

Looking through the *c*-plane section shown in Fig. 4.4(e,f and g) we observe the formation of distinct *m* and nano-*a*-facets. The nano-*a* planes are most distinct where the single quantum well growth was initiated and lose their definition as the layers develop. This can be explained through growth rate disparities on different facets competing towards the extinction of the

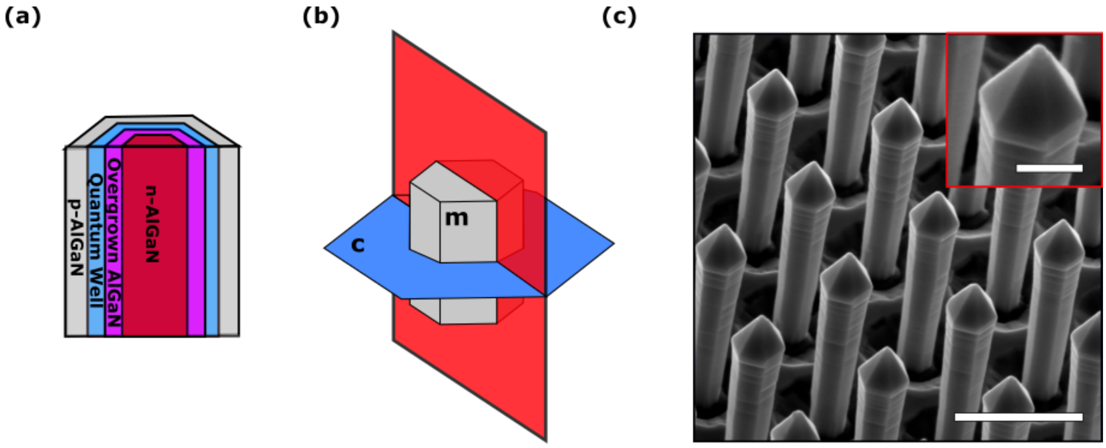

Figure 4.3: **Nanorod core-shell architecture.** **a,** Schematic of core-shell structures employed in this work, with n-AlGaN cores, quantum wells and p-AlGaN shells forming a basic full LED structure. **b,** Labelled crystal planes also showing the orientation of our TEM cuts. **c,** SE image of the nanorod array with clear uniformity in pitch and rod dimensions, scale bar is 1μm. Higher magnification inset shows a spherical feature at the tip of a rod. Scale bar is 250nm in this inset.

faster growing a-plane. Preferential incorporation of GaN on these planes has led to thickness and compositional variations in the quantum well, with 7 nm on the m-plane facet vs 12 nm on the a-plane.

Previous microscopy of InGaN [242, 243] and hexagonal InGaAlAs [244] nanorods found similar compositional fluctuations. A commonly suggested cause relates to inhomogeneous strain relaxation within the rod structures. [245] In the structures investigated here, the regrown AlGaN layer has a slightly higher AlN% content than the initial $Al_{0.76}Ga_{0.24}N$ core and thus, is in tension. In that case, to better match the lattice of the core, any excess of Al will be preferentially incorporated in the relaxed area. Conversely, the quantum well has a lower composition compared to the regrown AlGaN layer and is thus in compression. As a result, the behaviour is now reversed with the excess of Ga being preferentially incorporated at the relaxed area in order to match the lattice of the underlying layer. Differences in the sticking coefficients of Al and Ga ions on the distinct atomic structures of the a- and m-planes will also play a role, along with the growth conditions for each layer influencing the favourability of each ion on the different facets. [246]

The terminating p-AlGaN capping layer is observed to be more homogenous than the previous layers due to the elimination of a-planes at this stage, with both the layer thickness and composition fairly uniform. At the surface of the rods a thin heavily oxidised and AlN rich layer appears to form.

The second cut, looking through the m-plane, reveals multiple complex features. Compositional clusters are clear in the quantum wells in both Fig. 4.4j and k. I ascribe this effect to the wet etching of the n-AlGaN cores imparting a slight taper with an undercut inclination angle of around $2 \pm 0.01°$ and the formation of small surface steps. Through a step-bunching process, these surface steps become larger and more exaggerated as growth progresses. Under the QW growth conditions (more Ga, lower temperature and higher pressure) these steps become substantial enough to drive significant semipolar growth, resulting in clusters of distinct composition being incorporated into our quantum wells. [111, 247] The steps are visible on the

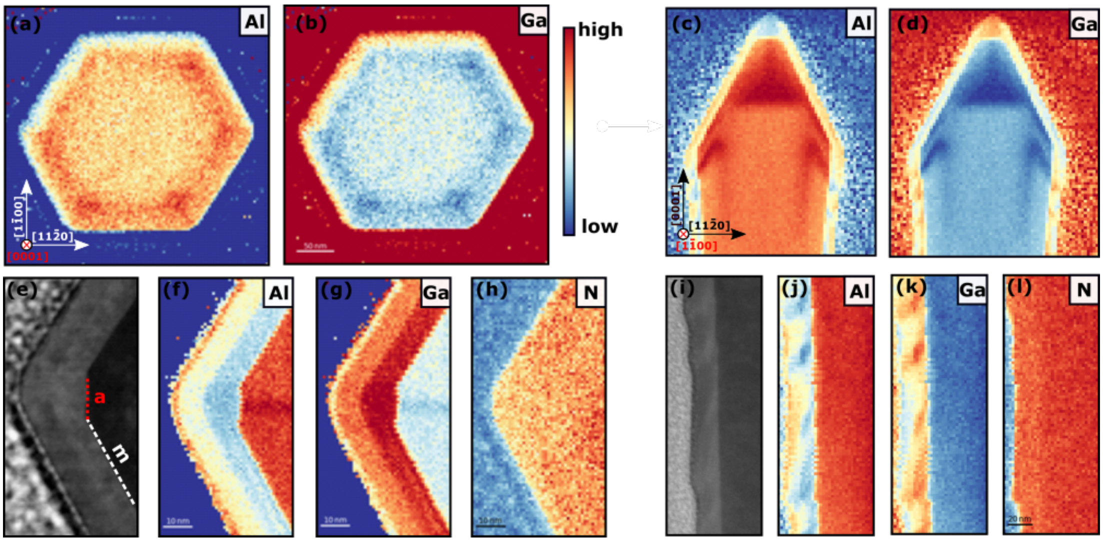

Figure 4.4: **TEM-EDS elemental composition maps. a,** Low magnification map of the first cut looking through the c-direction. The Al X-ray peak intensity variation within the core reveals increased Al incorporation on the a-axes. **b,** Ga K and L line X-ray peak intensities within the core showing the inverse of the previous Al map as expected. **e,** Higher magnification high-angle annular dark-field (HAADF) image focusing at one of the corners of the hexagonal structure. Z-contrast in the images reveals the location of the core, quantum well and capping layer. The formation of a distinct a-plane at the edge of the core is clear. **f,** Al X-ray peak intensity showing both the increased Al incorporation when moving from the core centre along the a-direction, but decreased Al in the quantum well on the a-plane facet. **g,** Ga X-ray peak intensity with the core again showing the inverse of the previous Al map as expected. **h,** N X-ray peak intensity showing uniform behaviour.**c,d,** Low magnification map of the second cut looking through the m-direction. The formation of the "broadhead" can be seen here. **i,** Higher magnification HAADF TEM image focusing along one of the a-planes. Here we can see the exacerbation of surface roughness as growth progresses outwards. **j,k,** Al and Ga X-ray peak intensities over the same area, showing alloy fluctuations along the quantum well. The Ga rich composition develops in a semipolar direction from the a-plane. **l,**N X-ray peak intensity showing uniform distribution.

surface of the rods in Fig. 4.3c as well as Fig. 4.4i. Although less pronounced and with a reduced miscut, these steps have already been observed in GaN/InGaN core-shell nanorods obtained with the a similar approach. [248]

The imperfect etch also leaves behind a slightly bulbous tip to the nanorod with multiple semipolar facets. During the initial refaceting step, these facets trigger the formation of AlN rich regions, tracing the form of a broadhead arrow which can be seen in Fig. 4.4(c,d). At this stage of growth the surface roughness on the sidewalls is not yet significant enough to trigger any other clusters to form.

A final feature visible in this orientation is a GaN-rich sphere which is also visible in SE images on top of the structures' c-plane facets. It is possible that there is no step or free surfaces nearby, leading to an elastic relaxation and the formation of a droplet during the QW growth.

4.5 Room Temperature Cathodoluminescence

I assessed the optical qualities of the structures by cathodoluminescence (CL) hyperspectral imaging inside a scanning electron microscope (SEM). [192] In addition to the full core-shell

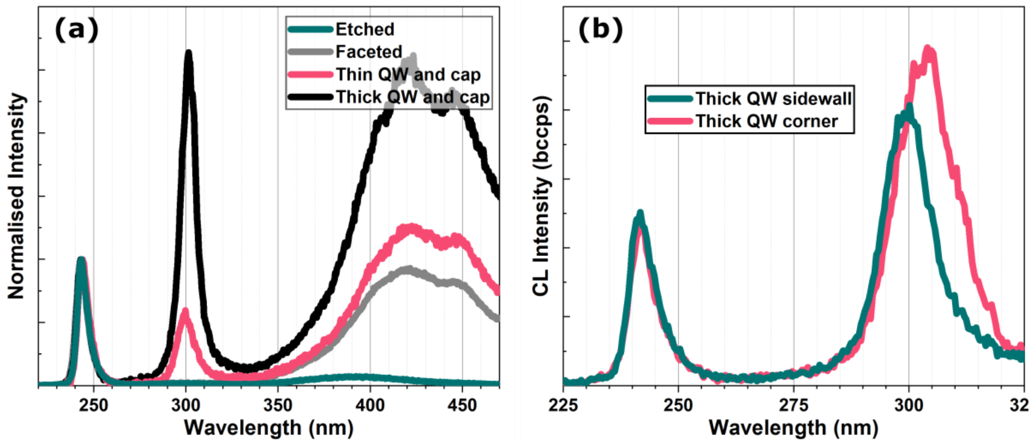

Figure 4.5: **Cathdoluminescence spectra from different nanorod samples and specific regions of the focus sample with thick quantum wells.a,**Cathodoluminescence spectra from the four samples: the etched cores; the etched cores following refaceting; following thin QW and cap growth and finally thin QW and cap growth . Each spectrum was taken by averaging a number of pixels from maps of each sample (taking care to avoid regions where the “substrate” was scanned directly) and was then normalised to the core band-edge emission peak. **b,** Spectra from the sidewall of the thick QW rods compared to the emission from the corners, showing a red shift in this region.

LED structure, I compared the examples of $Al_{0.76}Ga_{0.24}N$ dry/wet etched cores along with rods following the initial facet recovering overgrowth to explore the systematic effects of these processing steps.

The etched cores display strong band-edge emission at 243 nm and very low defect luminescence (peaking around 392 nm) as seen in Fig. 4.5. The optical quality of this core is a significant improvement over the AlN core previously employed to create AlN/AlGaN core-shell structures. [97]

The initial overgrowth and faceting step can clearly be seen to introduce a significant point defect population, resulting in multiple luminescence bands in the range of 360–470 nm. These defect bands are ascribed to cation vacancy complexes and are commonly seen in AlGaN alloys. [249, 250, 251] The lack of a band-edge emission peak from this layer could be due to the close compositional match to the core combined with this high defect population. Regardless of these defective facets, the full core-shell LED structure with quantum well and *p*-capping layer was found to be optically active with sharp peaks around 300 nm (fluctuating by around 10 nm). By varying the acceleration voltage and hence excitation volumes, I performed depth resolved CL measurements (not shown) on the full structures, finding that the majority of defect luminescence does indeed originate from the initial overgrown layer. Note the reactor employed for these overgrowth stages had not been optimised for high-temperature growth which could explain the incorporation of a high concentration of point defects.

Multiple overlapping emission peaks from the quantum wells limit fitting accuracy, and so band pass maps are a preferable method to show the intensities of different spectral regions which are shown in Fig. 4.6 along with a centroid energy plot. The core emission (242 nm) is uniform as expected, with any variation caused by the excitation/collection geometry. Interestingly the quantum well emission (284–314 nm) can be seen to be relatively uniform from rod to rod, but along each of these rods emission is strongest at specific spots on *m*-plane intersections. These correlate to the clusters seen forming at the internal nano-a planes in TEM. [243] A contributing factor to these intensity variations could be the striated surface itself which may slightly increase the light extraction efficiency and beam energy absorption. The effect of the compositional fluctuations is clear in the centroid map (Fig. 4.6c). Thicker wells would result in a redshift due to lower confinement [126], as would higher GaN incorporation since the effective band gap of the resultant AlGaN alloy would be lower. I am likely seeing a combination of the two effects, but with the significant compositional changes dominating. The high intensity emission of the clusters is likely enhanced through localisation effects due to the compositional changes. There is no evidence of increased defect luminescence from these clusters.

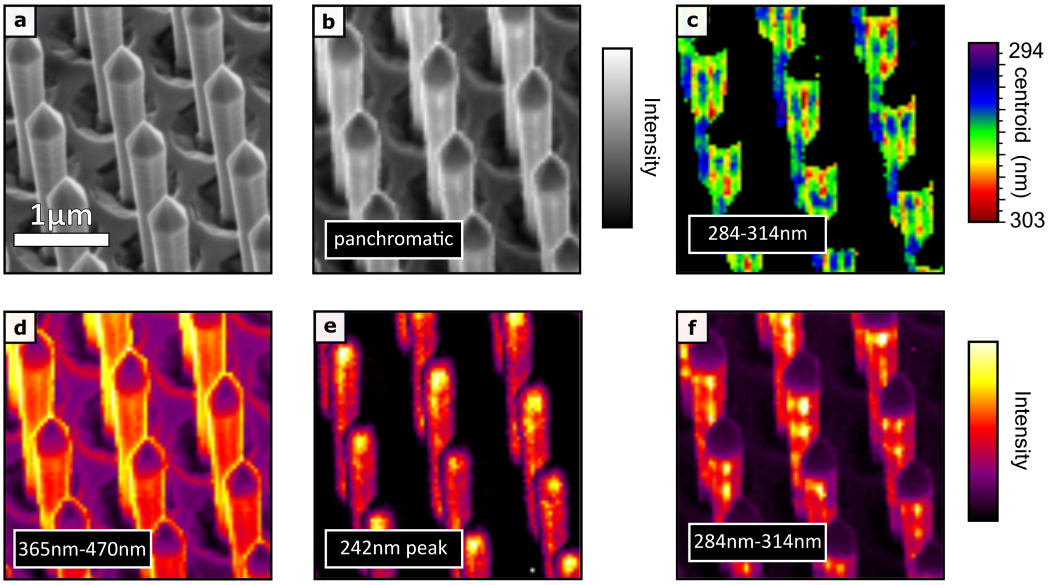

Figure 4.6: **Results extracted from a single SEM-CL hyperspectral image. a,** Secondary electron (SE) image of the area mapped. **b,** Panchromatic CL intensity map showing bright rod sidewalls and dark tops. **c,** Map showing the shift in centroid energy of the quantum well emission, with red shifts at the m-plane intersections (a-plane). The noise-dominated centroid in the substrate region has been masked in this map for clarity. **d,** Map showing the intensity of the defect luminescence increasing around the shell of the structure. **e,** Map showing the uniform band edge emission intensity from the core. **f,** CL intensity of the quantum well emission showing distinct high intensity clusters at the a-plane along with lower intensity emission from the rest of the sidewalls. Emission from the top semipolar facets is notably absent.

Despite TEM measurements indicating the presence of a thinner (7 nm) quantum well on top of the sloping semipolar facets of the rods, our CL measurements show a notable lack of luminescence from these regions. I suggest this to be due to a significant increase in the population of point defects acting as non-radiative recombination centres incorporated on these secondary facets under our growth conditions. [252] EDS measurements support this interpretation, showing significantly increased oxygen incorporation on these facets and demonstrating the ease at which some impurities may incorporate here. The radiative recombination rate would also be lower in this plane due to the QCSE further attenuating any QW luminescence from this region.

4.6 Low Temperature and Time-Resolved Cathodoluminescence

Low temperature (80K) measurements allow for the multiple components in the quantum well luminescence to be examined with greater ease. The compositional clusters observed in these structures could potentially behave as unintentional quantum dot like structures and measuring at low temperature can increase the chances of seeing distinctive luminescence from such features.

The data acquired reveals the complexity of our structures, with many distinct emission peaks visible across each structure with an example spectrum provided in Fig. 4.7a. At multiple points in the structure ultra-fine spectral lines can be seen, with full width half maxima of less than 1 nm. These extremely narrow linewidths suggesting highly confined states within some of our clusters.

On the rod sidewalls, two distinct peaks corresponding to a- and m-planes can be expected. The clusters, with their distribution of dimensions and likely compositions creates an additional sporadic spread of emission peaks. With this said, a general trend of higher energy emission near the tops of the rods and lower energy near the bottom can be seen. To visualise this I filtered three spectral regions 285–295 nm, 300–305 nm and 305–320 nm and arranged the composite image in Fig. 4.7 b.

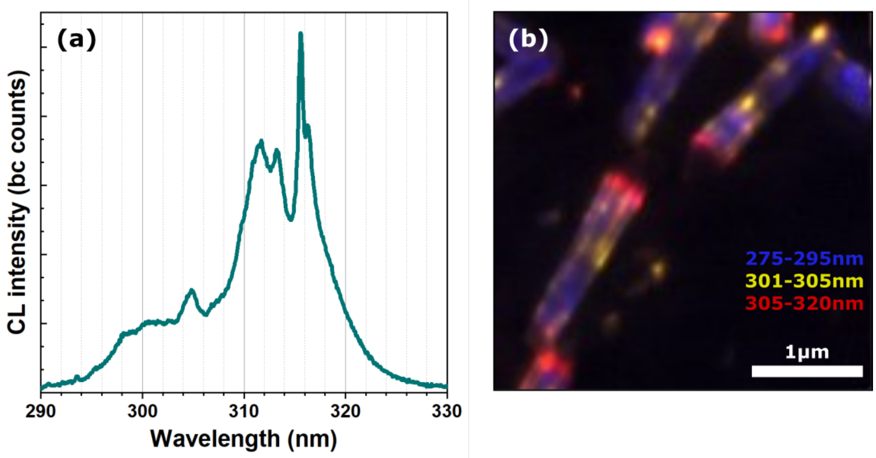

Figure 4.7: **Low temperature CL measurements on dispersed nanorods a,** Shows a spectrum from a point from a CW CL scan near the top corner of a rod with extremely bright and narrow red shifted emission. **b,** Composite image of dispersed rods showing different spectral regions in blue (285–295 nm), yellow (300–305 nm) and red (305–320 nm).

Due to the imperfect structure of the quantum well region, the electric fields strengths are unknown, and the layer may deviate away from true field free m-planes. Time resolved (TR) measurements can assist in investigating this matter.

Using a a short pulse of the electron beam, we can rapidly create an excited population and observe the speed of relaxation in our system using a streak camera. Carrier lifetimes will be extended in the presence of internal electric fields due to separation of electrons and holes. [253]

In my measurements I find that the lifetimes of our “m-plane” transitions are remarkably short even at 80 K. Depending on the mechanisms at play, different fits such as single, double and stretched exponentials can be used to model these systems. As seen in Fig. 4.8 I can fit a

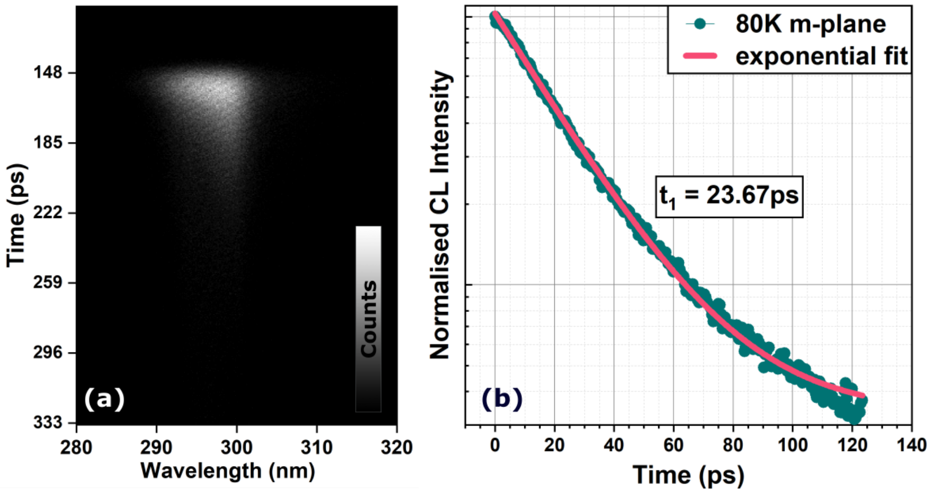

Figure 4.8: **Time resolved CL measurement of the m-plane region of a single nanorod at 80K. a,** The streak image from which we extract the data used to plot the figure on the right. **b,** Fitted monoexponential decay of the m-plane quantum well emission. The "zero" time here corresponds to the end of the risetime where CL intensity is a maximum.

simple monoexponential decay to the curve with good accuracy and find a carrier lifetime of 23.7ps. This value can be compared to data measured on c-plane AlGaN **at RT** supplied by Dr. Gunnar Kusch (AlGaN always has shorter times than InGaN so need to compare like to like). I fitted single exponentials to his data and extracted the lifetimes shown in table 4.1.

Emission wavelength (nm)	Composition (%AlN)	t_1 (ps)	QW plane
300	x	23.67	m
255	56	295.2	c
245	65	223.7	c
235	73	157.0	c

Table 4.1: **Lifetimes of AlGaN QW emission extracted from monoexponential fits of TRCL data**

If we extrapolate 300 nm emission from the c-plane values, one would expect a lifetime well in excess of 300 ps, however our 300 nm m-plane value measured is only 23.7 ps. Of course other factors such as well width and point defect densities will modulate these times, but I expect such a significant difference can only be explained by the absence or reduction of internal electric fields.

Attempts at delving deeper into the carrier dynamics proved challenging. Interpretation and analysis of the data acquired was further complicated by the point spread function of the measurement system which convoluted the signal measured by the streak. I did measure TR-CL at six points on a single rod at multiple temperatures. However, at each point the unavoidable excitation of multiple clusters with their own unique emission energies, temperature AND time dependencies. I expect this to be caused by the variable dimensions, compositions and strain state of clusters creating thousands of small unique emitters.

4.7 Electrical Characterisation

To check for the successful formation of a p-n junction, I make use of the charge-separating behaviour of a depletion region. Electrons and holes generated by the beam will be swept to opposite sides of the junction by any built-in electric field; if the p and n contacts are connected via an external circuit, this will result in a current flow analogous to the photovoltaic effect. The resultant electron beam induced current (EBIC) can be used as the image-forming signal.

I discovered that contacting these structures using oxide free tungsten probes directly was insufficient to create a good contact. This can be seen in Fig. 4.9e. With this in mind a bespoke contacting scheme was developed. In a clearing among the nanorod forest, a common n-contact was fabricated by milling down into the "substrate" by approximately 750 nm over a $2\,\mu\mathrm{m}^2$ region and then depositing 500 nm of Pt via focused ion beam (Ga) deposition (as described in Section 3.4). A further slightly deeper trench was then milled around the contact to prevent shorting. Nanorod p-contacts were made using two different methods. For "single" rod contacts both e-beam and Ga-beam deposition were trialed with beam current of 0.48 nA. For the block contact, the array of nanorods was first cleaved just below the hexagonal pyramid to expose the non-polar junctions. Ga beam deposition was then used to infill the array with Pt.

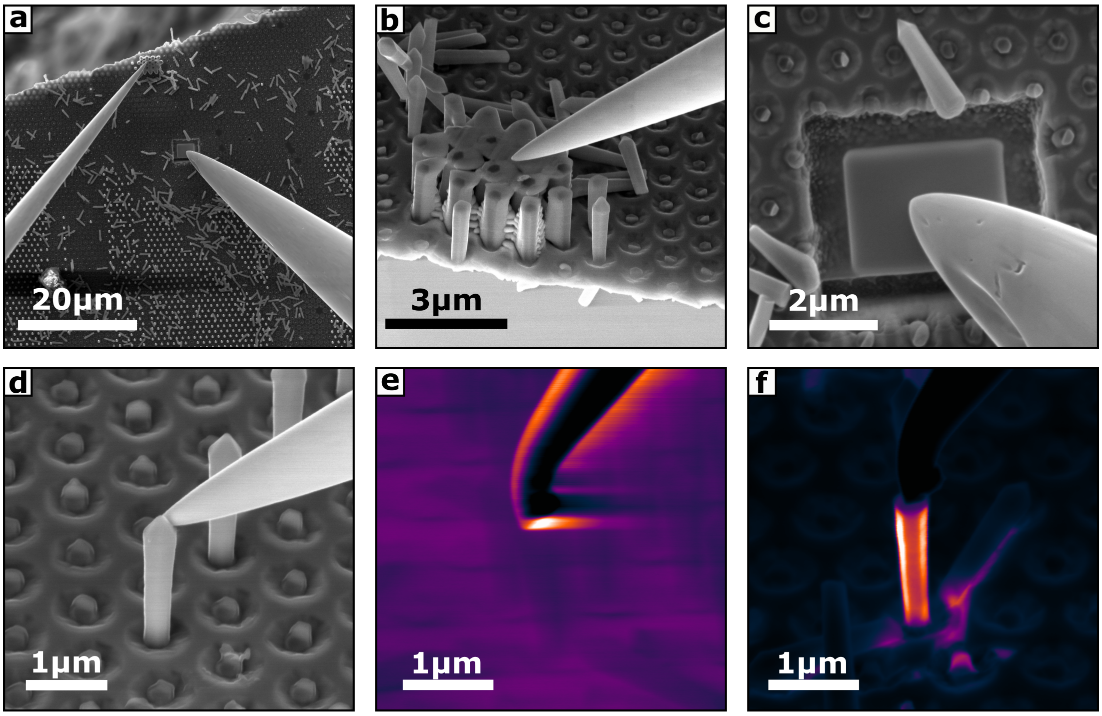

Figure 4.9: **SE (greyscale) and EBIC images showing the different contact types and the importance of metal deposition.** **(a)** Low magnification image showing the region where contacts were fabricated. **(b)** shows the small array of rods which was cleaved using FIB and then infilled with "Pt" to create contacts suitable for observing the cross sectional junction. **(c)** The n-contact formed through etching down into the n-layer again using FIB. **(d)** Shows our single rod contacts created by EBID and FIB deposition of "Pt" although this is not particular visible due to being such a thin layer. **(e)** Attempt at contacting a rod with no metal resulting in no real EBIC being measured. The contrast visible is likely due to electrons scattering off the samples morphology and back onto the tip. **(f)** A good single rod contact with metalisation showing EBIC contrast at the junctions.

Over multiple measurements over multiple weeks, I found the quality of the contact degraded significantly due to interaction with the air and the relatively low purity of the “Pt” deposited by FIB. Vacuum storage was found to prevent such degradation and samples could be measured multiple times.

The EBIC measurements on the cleaved block detailed in Fig. 4.10d show a strong uninterrupted *p*-*n* junction around all six of each rod’s non-polar *m*-plane sidewalls. Using our single rod contacts I checked the quality of these junctions along the length of our rods (Fig. 4.10c). From this perspective we can see the homogeneity of the junctions, with only some minor contrast variation visible which relates to the previously described striations.

Analogous to our CL measurements, the pyramidal semipolar facets appear dark in EBIC maps, indicating low current collection and therefore the lack of functional junctions. Similar to the case of CL, non-radiative recombination centres acting as carrier sinks would lower any collection current measured. The incorporation of compensating impurities during growth or the contact deposition method may additionally contribute to the low EBIC signal here.

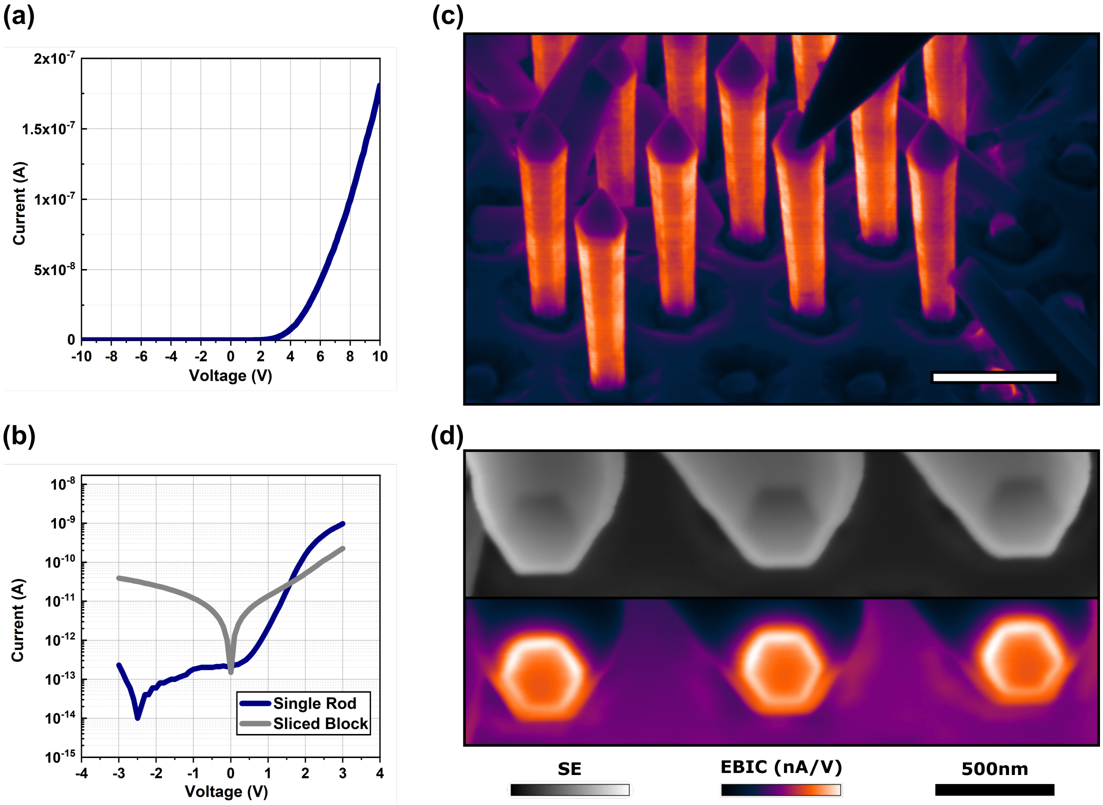

Figure 4.10: **Electrical characterisation of our core-shell LED structures.** **a,** *I*-*V* curves for a single rod contact. **b,** *I*-*V* curves for our two contacting schemes at lower voltages. The cleaved block contact shows a low rectification ratio and high leakage current, while the“single rod” contact shows strong rectification, indicating the successful formation of a p-n junction. **c,** EBIC image of a single rod contact, with the nanoprobe contacting from above. **d,** SE (greyscale) and EBIC images of the cleaved block contact viewed from above, showing the presence of the junction around the entire circumference of the rods as intended.

Rectification is the defining property of diodes and can be seen in the exponential behaviour of our current-voltage (*I*-*V*) curves plotted in Fig. 4.10a and b. This, combined with the EBIC maps, confirms not only the existence but also the quality of the junction. The block contact has a significant leakage current and a poor rectification ratio at ± 3 V of only 5.8. This is merely an effect of the Pt deposition coating over a large area and forming alternative pathways for carriers to flow. The block contact was prepared specifically for EBIC measurements using a technique which would not be used for optimal device fabrication, and so the poor *I-V* performance could be expected. I extended the measurement range further on single rod contacts up to ± 12 V and found a turn on voltage around 4.5 V indicating high doping efficiency and a rectification ratio of 10^5 post turn on at ± 5 V.

Despite multiple attempts, the focused ion beam deposition was found to deteriorate the quantum well luminescence and for this reason electroluminescence measurements using our single wire contacting scheme was not possible. Both the e-beam and Ga-beam deposition decreased CL emission, with Ga-beam being the worse of the two, quenching all luminescence due to implantation damage.

4.8 Conclusion

I have demonstrated that the AlGaN on AlGaN UV LED core-shell structure has active quantum wells and *p-n* junctions. I confirm that doping has been successfully achieved, evidenced by rectification in *I-V* measurements and EBIC imaging contrast. TEM measurements found compositional variations in multiple layers of the heterostructure including clustering in the quantum wells which is explained in relation to the initial etching of the n-AlGaN cores. I examined the quantum wells using cathodoluminescence spectroscopy and found strong emission near 300 nm with some red-shifting from these clusters.

This investigation suggests that further optimisation of the initial growth facets following etching and improvements in the initial overgrown material quality could lead to a highly effective architecture. Future iterations could include additional layers found to improve conventional LED performance such as electron blocking layers and MQW structures. The nanostructuring of AlGaN based LEDs may be key to overcoming the current barriers to efficient deep UV emission in solid state devices.

Chapter 5

Experimental Considerations for Nanorods

5.1 Single Rod Measurements

Traditional measurements of single rods from arrays such as those described in the previous chapter, involve rather primitive and brutal methods of detachment. A razor may be ran across the surface in the hope that some rods will be deposited over a suitable substrate, completely destroying the original array in the process. [254] Nanomaniprobes allow for a more elegant approach, where I can select an individual rod to break off, pick up and then place on a separate substrate or move to a desirable location. This process enabled me to position rods from multiple samples to be placed nanometers from one another, and be measured in the same maps together, allowing for more accurate comparisons between specimens. An example of this process can be seen in Fig. 5.1, where I placed rods with both thick and thin quantum wells side by side in the same orientation.

I soon discovered that contamination was a significant problem in our system when mapping single rods. During the acquisition of a CL map, the luminescence intensity could be seen to decrease as the scan progressed. Upon completion of the map, the rods appeared to have swollen in size. SE images acquired before and after mapping the rods on a Si substrate are shown in Fig. 5.1g and h. From these images I measure an increase in diameter ≈100 nm. I investigated this bloating effect using the EDX detector and found that it was due to carbon contamination. This contamination shell developed rapidly and was clearly detrimental to CL measurements. In an attempt to reduce this contamination, I measured rods deposited on a different material (copper) in case this process was enhanced by charging, allowed the microscope to pump down to the highest vacuum possible over a weekend and acquired a map over a quicker time. This resulted in some improvement but was still not perfect. Even after the time resolved measurements described in the previous chapter, growths could be seen on the rods where the electron spot was focused for prolonged periods, despite the low temperatures and higher vacuum used during these experiments.

Working with these rods may be so challenging due to their size and material properties, with charging possibly enhancing the rate at which contaminants are incorporated onto the surface.

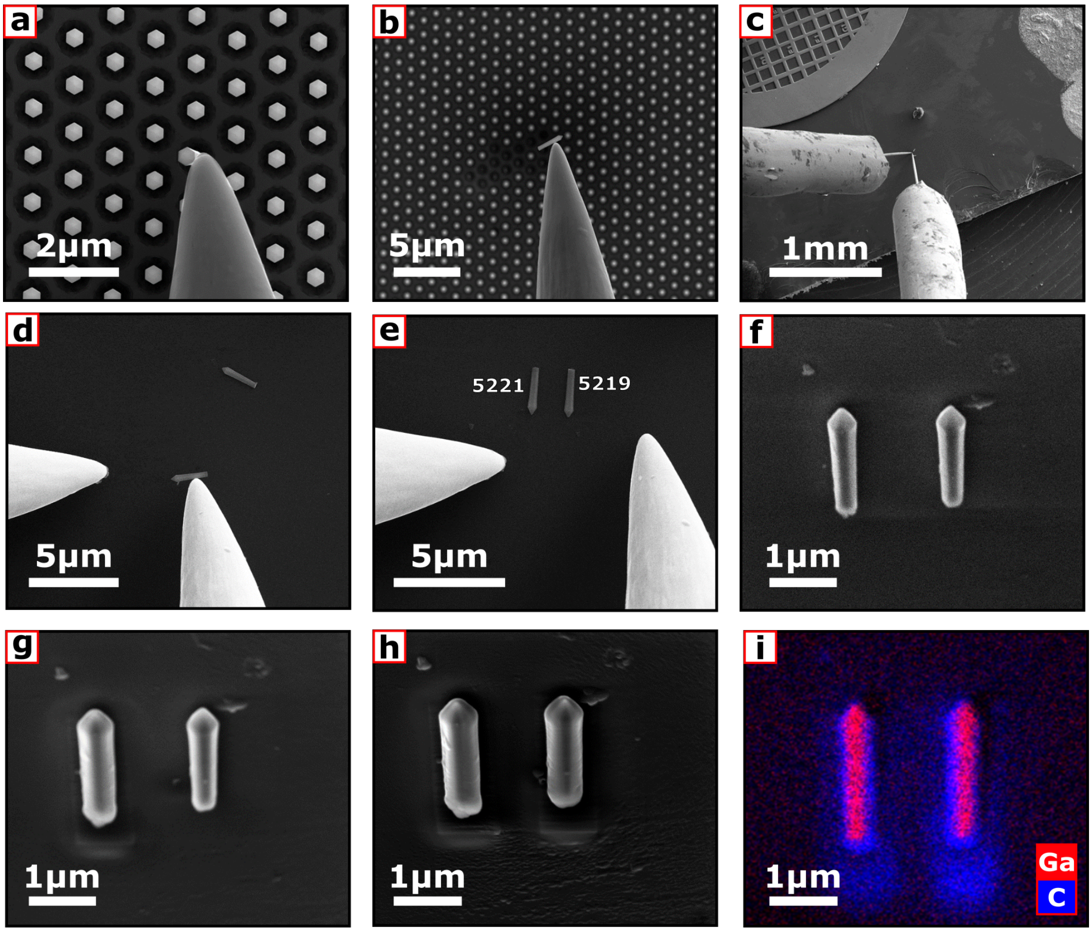

Figure 5.1: **The pick and place process of single nanorods using nanomanipulators.** **(a)** Breaking of rods from the array. **(b)** Rod lift out, held only through electrostatic attraction. **(c)** New substrate for deposition. **(d)** Rods deposited safely on Si. **(e and f)** Alignment of rods to ensure no geometric effects during CL or other measurements. **(g)** SE image showing the bloating of the first rod after scanning during CL mapping. **(h)** SE image showing the bloating of both rods after they have both been scanned during CL mapping. **(i)** EDX measurements showing a carbon rich shell has formed around the rods due to contamination.

5.2 Low Vacuum Measurements

I trialed CL measurements of nanorods in low-vacuum (LV) conditions (1 mbar) and found it disadvantageous. In addition to accelerated deposition of contamination I found that the quantum well luminescence measured was dramatically lower in LV when compared to measurements in high-vacuum (HV) under the same experimental conditions (Fig. 5.2). This is likely the result of two effects; Firstly the LV conditions cause an electron beam skirt to form, which diffuses the beam and lowers the carrier density within the specimen. [255, 256] This may prevent saturation of various population limited point defect luminescence processes, which reduce the number of carriers available to recombine in the QW and lowers the observed QW luminescence intensity. Additional scattering of both emitted light and electrons may occur due to interaction with particles in the chamber. This would lower the overall luminescence produced and collected, reducing our signal to noise for a set beam current. For these reasons I opted to operate in HV as much as possible, even at the expense of some drifting effects during mapping.

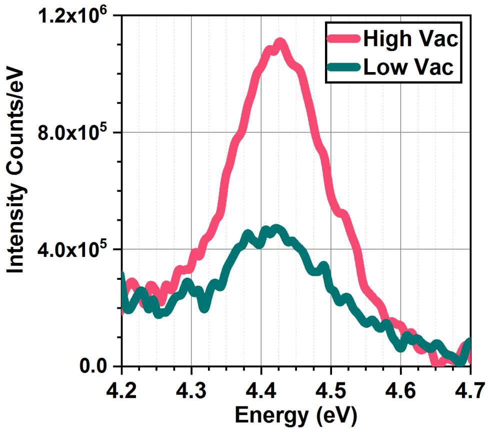

Figure 5.2: **Effect of chamber conditions on CL spectra measured.** Low vacuum measurements can be seen to make the quantum well seem dimmer while all other conditions were kept constant.

5.3 Bath Monte-Carlo Simulations

Monte-Carlo simulations using CASINO [186, 187] were initially performed to estimate penetration depths and excitation volumes when working with nanorods, but they revealed more and help explain some experimentally observed phenomena.

I created a simplified model of a real nanorod array using CASINO 3D. The rods simulated had a 1.8 μm long hexagonal body with a 125 nm radius with a 230 nm cone and were laid out with a 500 nm pitch. Positioning the rods such that their length lies orthogonal to the incident beam. We can see that at even at 5kV and scanning over a single rod, other rods multiple rows down and along are also excited. The regions of free space between rods allow electrons to travel freely without collisions and energy losses. This leads to geometric patterns forming, dictated by the array dimensions. Interestingly the SE image shown in Fig. 5.3b presents similar patterns in contamination following CL mapping. The average energy of electrons hitting these surrounding structures will also be lower which is important when working with core-shell structures. We can also see that within a scanned rod certain areas receive a higher dose due to the hexagonal shape of the structures, with corners and edges effecting electron scattering.

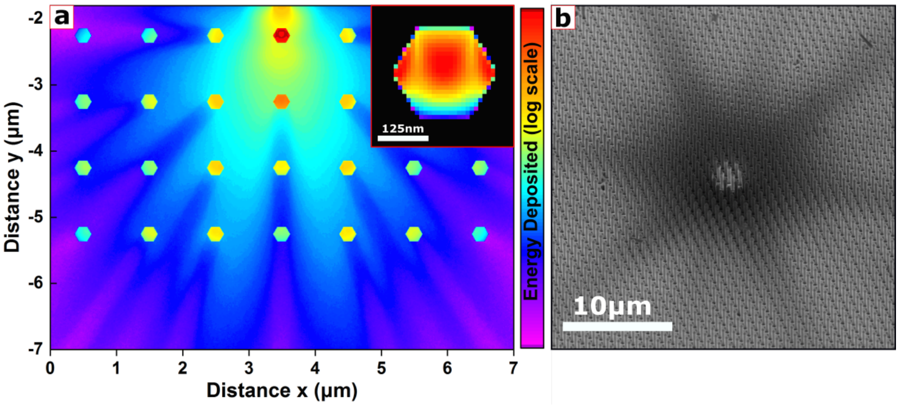

Figure 5.3: **Nanorod array simulations and observations**. **a,** Shows energy deposition in the array after exciting a single rod on a log scale. The inset shows excitation of a single rod leading to non uniform energy deposition in more detail. **b,** SE image with similar pattern.

5.4 Grenoble Simulations

I have already discussed the multitude of barriers that arise when attempting to develop effective deep UV emitting devices, many of which pertain to the challenges of p-type doping and contacting in AlGaN devices. By pumping the system optically or by e-beam we no longer have need for pesky *p*-layers or contacts making this approach very appealing indeed.

In this section I focus on an e-beam pumped UV laser structures developed by Prof. Eva Monroy's group. I perform Monte-Carlo simulations again using CASINO [186, 187] in three-dimensions in order to asses how the excitation of such a structure changes as a function of acceleration voltage.

Simple simulations of graded-index separate confinement heterostructures based off Monte-Carlo methods had been performed previously, but not in three-dimensions or on accurate geometries. [257] For my simulations I approximate the structure of a real specimen in both bulk and nanowire forms and compare the differences between the two.

The nanowire geometry is used due to the potential for improved light extraction, but how efficiently such structures can be pumped with an electron beam needs to be calculated. The true experimental structure which I approximate here is grown on Si(111), where a 7 nm thin AlN buffer precedes 850 nm of GaN:Si. The active region of the device consists of 88×3 nm AlN barriers and $Al_{0.05}Ga_{0.95}N$ quantum wells. From SE imaging I could see the wires' diameters are somewhat varied and even coalesce at certain points. For simplicity's sake, these random variations will not be accounted for in my simulations.

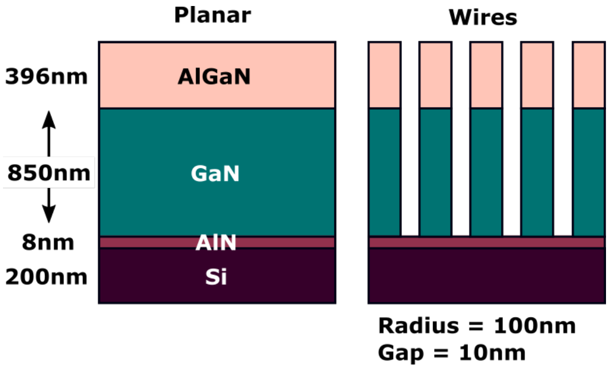

Figure 5.4: **Schematics of the two structures simulated.** the first being a planar specimen and the second a nanowire array.

I defined the wires as simple cylinders with diameters of 100 nm arranged on a grid with 10 nm separation between nearest neighbours. The array was 9×10 rods. I also approximated the MQW structure as a single block with an average density $\rho_{\mathrm{AlGaN}} = 5.13\,\mathrm{gcm}^{-3}$, although in practice more energy would be deposited in the QW than in the barriers. A schematic of the two structures simulated is shown in Fig. 5.4

For the beam conditions I setup a 5 nm probe diameter and a 5 nm step size completing a square raster over 105 nm^2. On each of these scan points 10,000 incident electrons will interact with the specimen.

I collected data over a $100 \times 100 \times 170$ mesh corresponding to 1000 nm×1000 nm×1700 nm volume. This resolution could have been increased but would have resulted in longer run times. I then use this data to produce two dimensional plots which show the average energy absorbed in the X-Y (Fig. 5.5) and X-Z planes (Fig. 5.6).

In the X-Y plane it is immediately apparent that the total excitation area is noticeably larger in the wire geometry. This is due to the large volume of free space in the structure allowing electrons to travel significant distances unobstructed. The array structure dictates the intricate patterns that emerge. It is worth clarifying that the majority of excitation in both geometries is still within a narrow region.

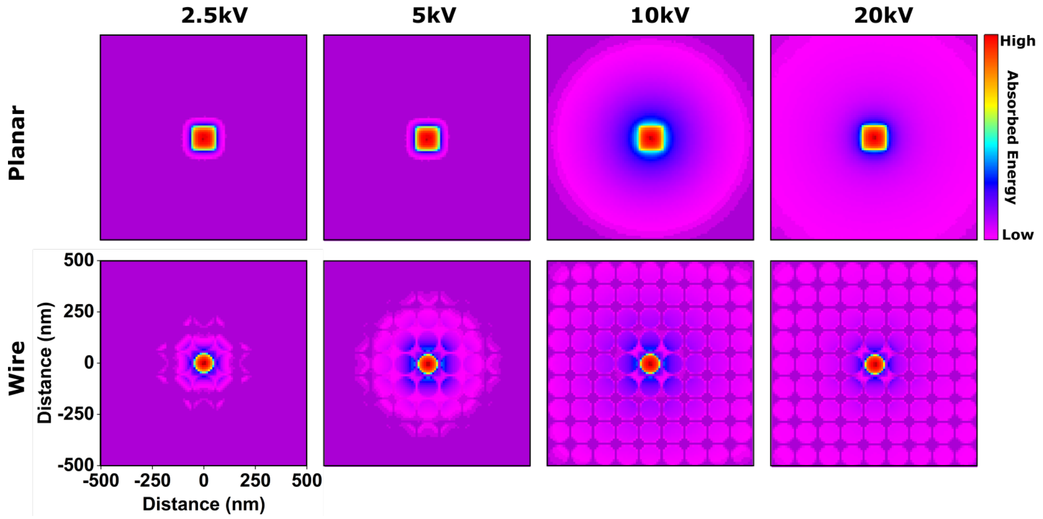

Figure 5.5: **Absorbed energy distributions.** Plotted for both the planar and nanowire structures X-Y planes at various acceleration voltages from Monte-Carlo simulations.

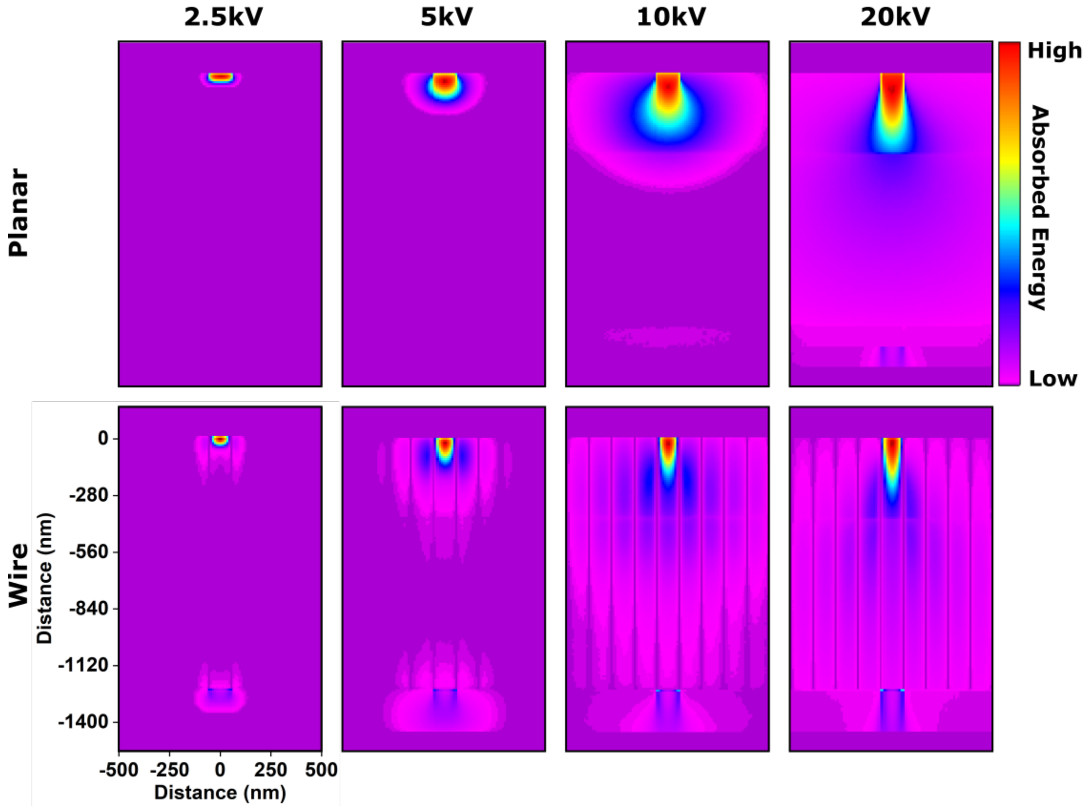

Figure 5.6: **Absorbed energy distributions.** Plotted for both the planar and nanowire structures X-Z planes at various acceleration voltages as predicted by Monte-Carlo simulations.

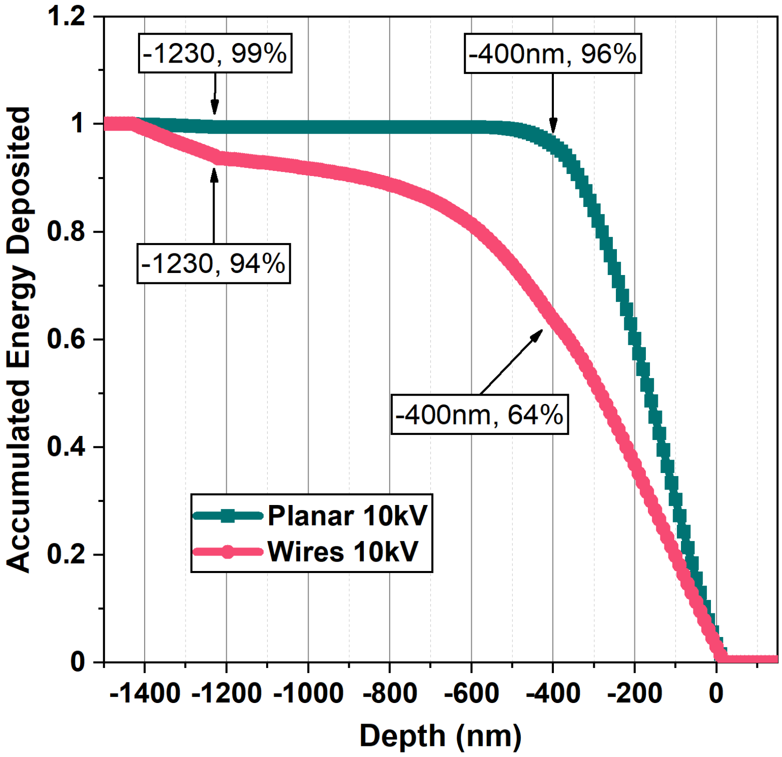

Figure 5.7: **Accumulated energy as a function of depth in both the nanowires and planar structures.** This plot is produced using the plots shown in Fig.5.8

Examination of the penetration depths and what layers are excited efficiently are most important for electron beam pumped devices. This can be seen in Fig. 5.6. In this plot it can be seen that the electrons penetrate deeper in the wire array than in the bulk, potentially leading to wasted energy during device operation.

In these simulations I excite straight down, hence channeling effects are significant. Angling of the beam during the simulated scan would reduce these. In a true device employing a scanning cathode, the angular incidence of the electrons would reduce channeling and keep a larger proportion of excitation in the MQW region.

Electron channeling also leads to back excitation due to electrons entering the sample floor being redirected through scattering back up into the base of the rods.

As you can see from Fig. 5.7, for a 10 kV beam only ≈64% of the energy is deposited in the MQWs region of the wire sample under my simulated excitation conditions. However, due to the scanning of the simulation only 71% of the beam is initially directed at the rod with the vertical excitation leading to significant channelling. Even accounting for this there is a significant discrepancy between the wires sample and the planar equivalent. Fig 5.8 shows the data from which this figure was constructed, along with equivalent data for 2.5, 5, 10 and 20 kV for comparrison.

My conclusion from these simulations is that although the nanowires may offer improvements in regards to LEE, reduced TDD and more, the losses in excitation efficiency due to channeling and scattering effects must be considered when assessing the effectiveness of these devices.

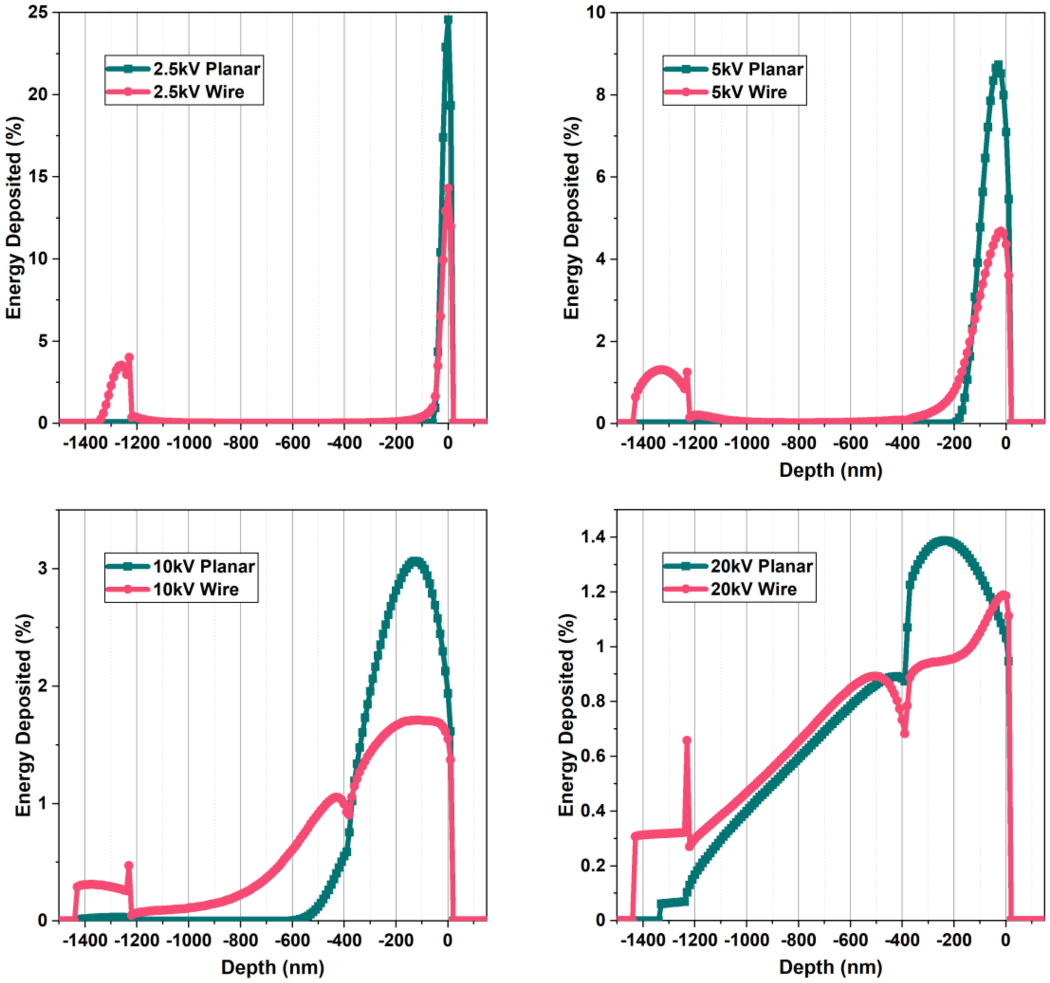

Figure 5.8: **Monte-Carlo simulations with the beam travelling down through the various layers of different structures.** Simulations were ran at 2.5, 5, 10 and 20 kV

Chapter 6

UV-LED structures

This chapter focuses on planar UV-LED structures prepared by Drs. Frank Mehnke, Tim Wernicke, Praphat Sonka and their colleagues at the Technical University of Berlin in the group of Prof. Michael Kneissl. The ELO AlN/sapphire substrates were fabricated by Drs. Sylvia Hagedorn and Markus Weyers at the Ferdinand-Braun-Institut. I investigated these structures using a range of scanning electron microscopy techniques. Transmission electron microscopy was performed by Dr. Simon Fairclough at the University of Cambridge. Thanks must also be given to Dr. Gunnar Kusch for initiating this collaboration and his involvement during the discussion of subsequent results.

6.1 Introduction

As previously discussed in Chapter 3, it has proved challenging to produce short wavelength emitters, as their external quantum efficiencies dramatically decrease with increasing AlN content due to reductions in radiative recombination efficiency, carrier injection efficiency and light extraction efficiency. [209, 258]

During the epitaxy of AlGaN on sapphire for deep UV emitters, significant lattice mismatch leads to highly strained heterojunctions and the formation of threading dislocations. The influence of threading dislocations as well as the cumulative effects of surface imperfections in the various epitaxial layers of a UV LED result in lateral variations. How these inhomogeneities impact overall device performance remains unclear.

Here I examine a series of planar UVC LED structures with quantum well emission wavelengths ranging from 263nm–217nm. [259] The full LED structures were grown by metalorganic vapor-phase epitaxy on an epitaxially laterally overgrown sapphire/AlN template with an average edge type threading dislocation density of $1.5 \times 10^{9}\,\mathrm{cm}^{-2}$ and screw type threading dislocation density of $3 \times 10^{7}\,\mathrm{cm}^{-2}$. [260] The complete heterostructure stacks are detailed in Table. 6.1. For the two highest AlN% samples the thick n-layer was changed to 95% AlN due to the composition of the active region. This change turns out to be very important and is needed to prevent absorption effects with backside collection

To begin my investigation I focused my efforts on the sample labelled "TS4777" which contained the lowest AlN content as it was expected to be the easiest to measure. When working with high AlN content samples the low conductivity makes SEM and electrical measurements difficult; The polarisation of the emission also creates difficulties in luminescence studies due to the decreased counts collected.

The metal contacts deposited are not described here and were not discussed with the growers as it was not the focus of our study. I did measure some EDX from the region which gave some insight into the metals involved; Nickel, gold, aluminium, titanium and vanadium could all be found to some extent, with the composition of the *n* and *p*-contacts clearly distinct. These metals are all fairly standard when working with AlGaN/GaN. [80]

Layer	Material	x (%)	d (nm)
Cap	GaN:Mg	0	40
Superlattice 1 (×15)	AlGaN:Mg	37/20	75 (2.5/2.5)
Superlattice 2 (×14)	AlGaN:Mg	80/70	25 (0.9/0.9)
Electron Blocking layer	AlN	100	6
Barriers (1/2 delta doped)	AlGaN	**B**	5
QWs (×3)	AlGaN	**A**	1
First barrier	AlGaN:Si	88	40
Current spreading layer	AlGaN:Si	**C**	1200
Transition layer	AlGaN	**C**	100
Graded layer	AlN to AlGaN	100 to **C**	25
Buffer	AlN	100	400
ELO Template			

Table 6.1: **The complete heterostructure stack from growers best estimates**

Specimen	Composition **A** (%)	**B** (%)	**C** (%)	Wavelength (nm)
TS4777	47	59.5	90	263
TS4780	59	71	90	249
TS4782	68	79.5	90	239
TS4774	74	85	90	234
TS4769	77	88	90	230
TS4808	82	93	95	222
TS4803	86	97	95	217

Table 6.2: **Layer compositions present in the different specimens.**

6.2 Electron Beam Induced Currents

For EBIC measurements I examined the initial specimen (TS4777) in both plan-view and cross-sectional geometries. In the planar orientation, multiple effects combine to produce the EBIC images seen in Fig. 6.1. Large scale contrast features are due to the inhomogeneity of the *p*-GaN capping layer thickness (visible in the SE image Fig. 6.1a), vertically displacing carrier generation volumes relative to the junction position. The thickness of this layer varies due to inhomogeneous step bunching processes. [261] The largest current will be induced when the generation volume has greatest overlap with the space charge region. For this reason, the contrast related to capping layer thickness is inverted when I vary the acceleration voltage from 5 kV to 20 kV and is minimized at around 10 kV when the energy deposition best matches the 140 nm depth of the QWs. Generally, higher acceleration voltages decrease spatial resolution in thick samples due to the larger volume of excess carriers generated. However, here relatively high resolution is maintained due to the EBIC signal being dominated by carriers generated in, or diffusing into, the junction volume.

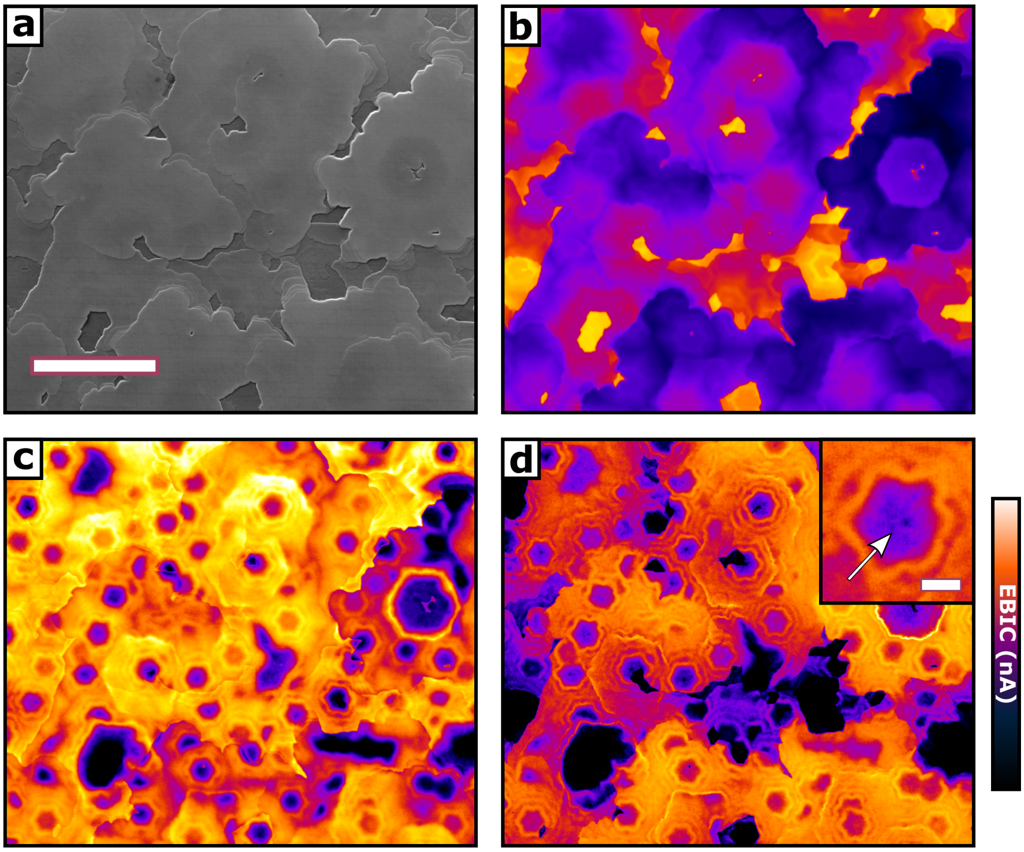

Figure 6.1: **Electron beam induced current measurements on the same area acquired at multiple acceleration voltages.** **(a)** Secondary electron image of the area with 5 μm scale bar. EBIC images at **(b)** 5 kV, **c** 10 kV and **(d)** 20 kV, including an inset with 500 nm scale bar to highlight an extended defect.

At the higher acceleration voltages, a network of small hexagonal and dodecagonal rings is apparent in the EBIC contrast across the entire sample. This is evidence of an asymmetric junction, caused by the complex multilayer structure of our device. Results of a band profile simulation [262] of this specimen by Dr Martin Guttmann can be seen in Fig. 6.2. This figure displays that the electric field strengths are dramatically different depending on depth.

The fields on both sides of the junction can also change somewhat independently due to pinning in intermediate layers. Our depth resolved measurement therefore implies that the origins of the hexagonal ring structure lie within the thick n-contact layer. The presence of these crystallographically aligned rings indicates local variations in electric field strengths and/or recombination efficiency. The presence of multiple tiers in these rings suggests a three dimensional growth mode of hillocks, with the inclined slopes of these features influencing the aluminum nitride mole fraction as well as doping concentrations. [263]

Dark spots near the centre of these rings are consistent with threading dislocations acting as recombination centres. [190, 264] I anticipate these extended defects to be screw type threading dislocations, based on previous electron channelling contrast imaging by Kusch et al. on polar n-AlGaN layers. [265, 266, 267] By counting the number of spots in each image I can calculate a density of $3 \times 10^{7}\text{cm}^{-2}$ matching the growers estimation for screw dislocation density previously stated exactly. The absence of dark spots in the low kV EBIC images is somewhat unexpected

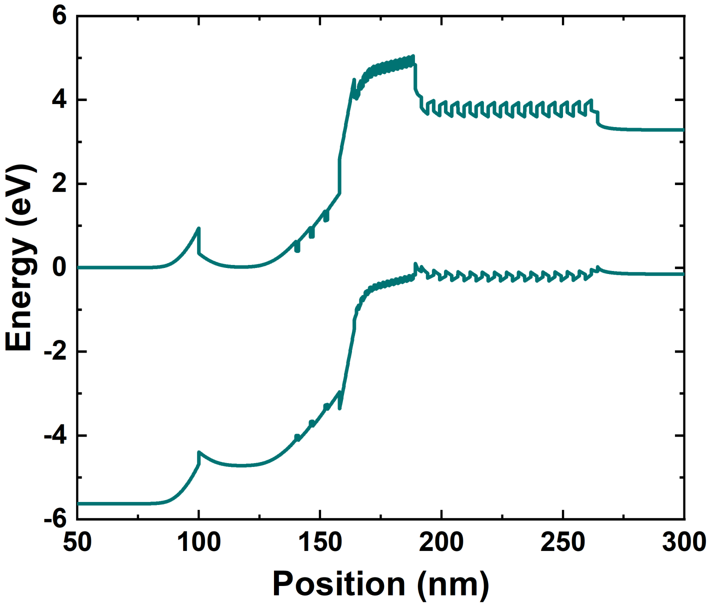

Figure 6.2: **Simulated band profile for TS4777 (263nm emitting) LED structure**. This profile is plotted with the n-region on the left hand side and the p-region on the right, with the superlattices clearly visible.

as the dislocations should move through the whole structure. This could be related to the different layer thicknesses on the *p*- and *n*-sides. The thicker n-contact layer would allow for more lateral diffusion of carriers when they are generated here and the size of the dark spots will depend on this. The p-layer is thin, giving a lower chance of carriers diffusing laterally to the TD before being collected by the junction.

Cross-sectional EBIC (see Fig. 6.3) reveals the presence of a secondary weaker junction at the AlN/AlGaN heterojunction near the substrate when contrast is exaggerated. This is caused by the bandgap discontinuity and polarization fields forming an additional depletion region. [268] A similar effect should occur at the the top of the sample which I cannot resolve due to the close proximity of the main junction.

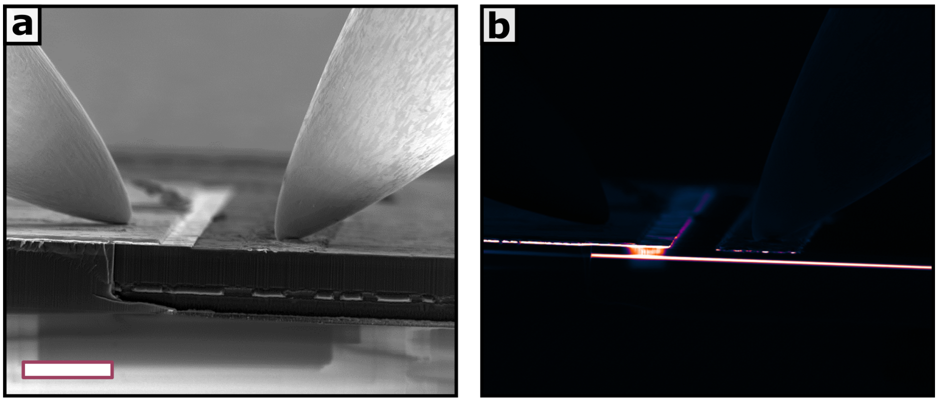

Figure 6.3: **Electron beam induced current measurements performed in cross section with exaggerated contrast.** **(a)** SE image with 10 μm scale bar displaying the orientation of the measurements, with large probes used to establish contact. **(b)** Exaggerated EBIC signal showing not only the main junction, but also signal due to the slight Schottky nature of the contact and the second depletion region near the substrate interface.

6.3 Cathodoluminescence and X-ray analysis

To assist in explaining my EBIC observations, I performed complementary CL measurements. The selective plasma etching enables the study of the full heterostructure as well as the n-contact layer in isolation. First I discuss CL measurements on the n-contact region where the emission spectrum is dominated by the band edge emission (≈ 222 nm). I fit a Gaussian function to this peak and then map out the fitted peak intensity and centre wavelength as seen in Fig. 6.4. Hexagonal features with bright edges can clearly be distinguished, and the energy of the emission here is significantly red shifted (≈ 60 meV) relative to the centre of the hexagons due to changing alloy composition. Another notable feature in the band edge emission is the presence of darker six-fold symmetric lines, intersecting slightly offset from centre of these hexagons. These are an additional consequence of the growth modes and subsequent preferential incorporation on distinct facets. [252, 269, 270]

In addition to the band-edge emission, two broad low intensity defect bands are observed. These are known transitions between shallow donors and two distinct deep acceptors. [271, 272, 250] The intensity of the first band lying between 250–310 nm follows that of the band edge emission. The second band (≈ 350–420 nm) shows brightest emission from clusters which align precisely with the intersection of the sixfold lines where I expect a threading dislocation to be located. The density of the defect clusters observed in the n-layer (Fig. 6.4c) matches well with the hexagons observed in the EBIC image and the formation of compensating defects may contribute to the decrease in the EBIC inside the small hexagons.

When measuring the full LED structure, I find the intensity of CL collected from the QWs is significantly modulated by variation in the absorbing capping layer, with increasing cap thick-

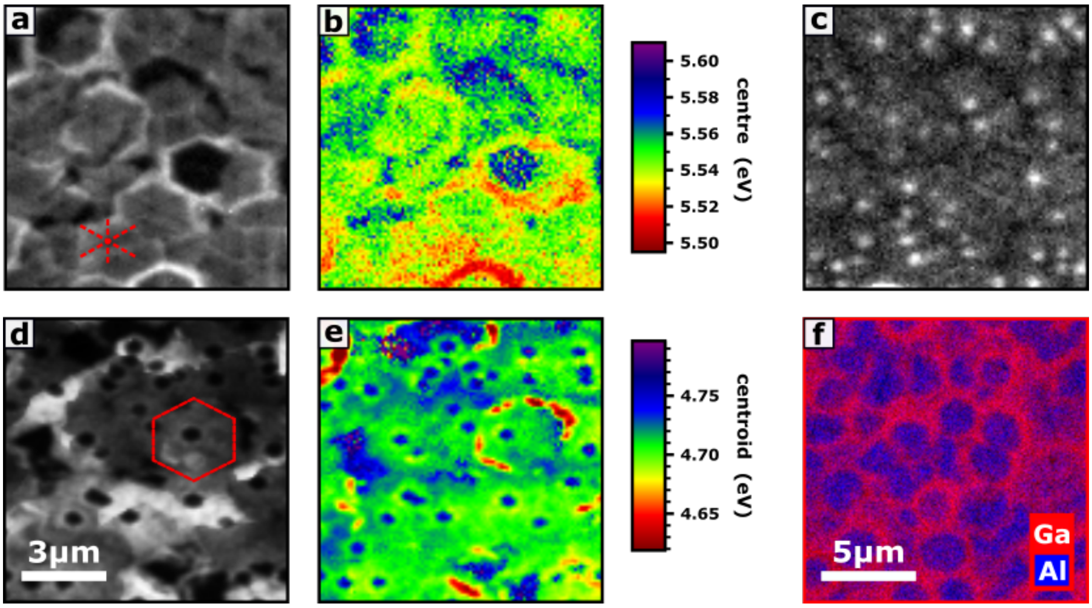

Figure 6.4: **CL and characteristic X-ray images.** CL was mapped over 10×10 μm areas across both n-contact layer (a–c) and p-contact layer (d–e) using 6 kV. **(a)** The fitted intensity and **(b)** centre energy of the band-edge (222 nm) luminescence. **(c)** Defect luminescence band intensity (360–425 nm) in the n-contact layer. **(d)** Quantum well emission intensity (262 nm) and **(e)** emission energy maps. **(f)** Characteristic X-ray map of a 15×15 μm area of the n-contact layer, with Ga shown in red, and Al in blue.

ness decreasing the luminescence intensity due to absorption in this lower bandgap layer. A *p*-GaN layer is employed due to the high resistivity of *p*-AlGaN and in a final device electroluminescence can freely escape via the sapphire substrate. [273] Despite this obscuration one can still discern some larger hexagonal features with similar dimensions to those seen in the *n*-layers, relating to the GaN-rich regions. These appear with greater clarity in the centroid map, due to the redshift of the emission here. In addition, I find smaller hexagonal spots with low emission intensity and blue shifted energies. When compared with simultaneous EBIC data, these more numerous spots can be seen to align precisely with the ring structures previously described. The coincidence of low signals in both EBIC and CL confirms an increase in non-radiative recombination at the extended defects. [274]

I have also mapped the characteristic X-rays through the two surfaces. Note that although it is possible to quantify dopant concentrations using WDX [166, 275], mapping such small fluctuations is precluded by the X-ray count statistics. It also would fail to capture which of these dopants are actually electrically active.

My measurements through the *p*-capping layer showed no significant variation. However, the X-ray maps of the *n*-contact layer (shown in Fig.6.4f) uncover clear Ga-rich rings and Al-rich spots, confirming that the red-shifted, high intensity luminescence I observed in the hyperspectral CL is related to changes in the alloy composition. Our results are consistent with previous works [166, 276, 223, 277] where it has been shown that hexagonal platelets with Ga-rich extremities develop during polar AlGaN growth due to the differences in mobilities between the Al and Ga ions. [112, 111]

Combining the cathodoluminescence, electron beam induced current and X-ray microanalysis reveals that dislocations with a screw component permeate through the heterostructure into the active region and perturb their local environment in each layer as growth progresses. In addition to acting as non-radiative recombination centres, it appears that these dislocations encourage high point defect densities and three-dimensional growth within their vicinity. In this specimen I find that these point defects can add parasitic recombination pathways and may compensate intentional dopants.

6.4 Impact of Varying Composition

To investigate the effect of varying the composition of various layers in devices, I proceeded to map the EBIC from the full sample series. The resultant EBIC images from each of the samples can be seen in Fig. 6.5. It is immediately apparent that the compositions in the active region have a dramatic effect on the internal fields within the junction. The changes are such that they cannot be explained by the alloy variation alone, indicating the different growth conditions modulate the layer morphology and defect populations. There seems to be distinct shifts above 50%, 70% and 80% but without specimens who possess intermediate values it is difficult to describe this evolution. The samples with 59% and 68% show less of the defined hillocks and ring features, while presenting a high density of threading dislocations. These dislocations are still acting as non radiative recombination centres at this point, and showing some showing some ill-defined features in their surroundings. Above 70% the dislocations become less clear, but the platelets and rings are very distinct but with wavy facets. Interestingly they appear brighter than their surroundings in contrast to the original case seen in TS4777. The scale of the features are fairly consistent in all samples but their effect on the EBIC differs.

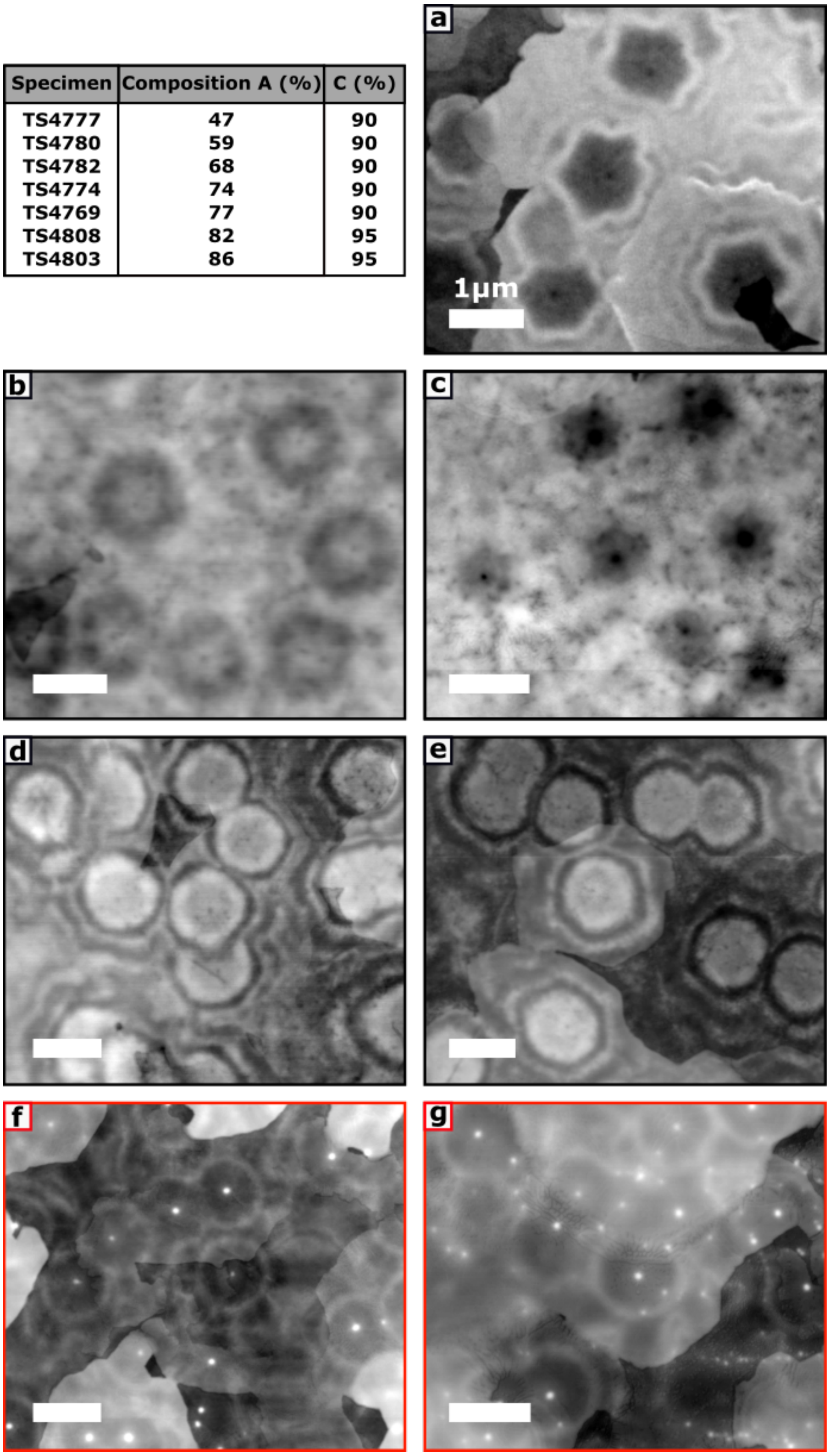

Specimen	Composition A (%)	C (%)
TS4777	47	90
TS4780	59	90
TS4782	68	90
TS4774	74	90
TS4769	77	90
TS4808	82	95
TS4803	86	95

Figure 6.5: **EBIC images from the full sample series with 1 μm scale bars showing similar sized features, but with different properties. (a–e) contain 90% AlN *n*-layers and (e–f) contain 95% AlN *n*-layers (a)** TS4777 (47% AlN in the QW) **(b)** TS4780 (59%) **(c)** TS4782 (68%) **(d)** TS4774 (74%) **(e)** TS4769 (77%) **(f)** TS4808 (82%) **(g)** 4803 (86%)

The most remarkable finding can be seen within the 82% and 86% AlN samples with the $Al_{0.95}Ga_{0.05}N$ n-layers. Here, the screw-type dislocations themselves appear as bright spots, and en masse resemble a starry night's sky. Explaining this is not trivial and is the subject of my ongoing research.

Bright spots in EBIC contrast related to dislocations have previously been seen in InGaN quantum well systems, [278, 279] although in general it is far more common to observe threading dislocations as dark spots.

Local band bending at grain boundaries have previously provided bright and dark REBIC signals by modifying the band structure to create the profiles found in Fig. 6.6. [174] Similar could occur in our samples with the contrast in EBIC dictated by band bending direction and the minority carrier concentration. The saddle or sink like features could modulate the collected current by increasing or reducing the separation of carriers. If the dislocation acted as a region for charge to congregate, it could create such a local potential distortion along the dislocation line.

Although not specifically discussing III-nitride systems, descriptions of charged line defects are given in works by both Holt and Joy [172] as well as Wiltshaw [280]. There are however photoelectrochemical etching experiments in GaN which have indicated that the dislocations can influence the distribution of charge. [281] The caveat of this explanation coming with the defects being more visible on the n-side of the junction, therefore this mechanism might only explain observations in one of the two specimens since the doping type should be fixed.

Previous TEM measurements have also shown that dislocations in AlGaN can have increased metal concentrations in their structures, which would also modify the bands locally and affect localisation. [282]

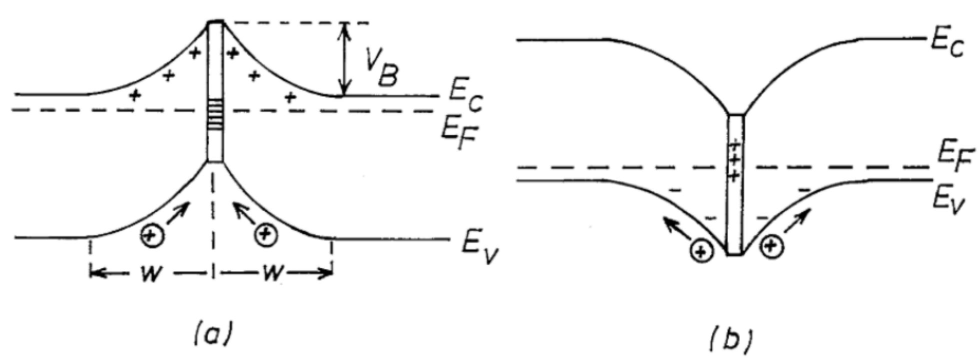

Figure 6.6: **Simple explanations of bright/dark contrast in EBIC. (a)** Shows a region where a grain boundary or extended defect locally creates bandbending which increases separation of electrons in its grasp. **(b)** shows the opposite case where an electron sink forms allowing for either radiative or non radiative recombination can occur. Figure taken from [174]

A further important factor to consider are the various different states introduced by the threading dislocations. The specific states present will depend on the core type, decoration and composition. [283, 55] These states could enhance the non-radiative recombination rate in the case of black spots in EBIC. They could also act an enhanced carrier pathway, which would lead to them appearing white. For example, metallic like behaviour in a filled core dislocation may lead to quantum wire like behaviour. [284, 285] These enhanced carrier pathways could explain why TDs are commonly related to leakage currents in many devices. [286] The areas surrounding the defects will also be affected, with the incorporation of point defects and changes in strain. These could also contribute to the effects I observe.

The wide ranging predictions from theory and observations from experimentation involving threading dislocations has now lead to significant research being conducted in so called "dislocation technologies", where dislocations with specific properties are intentionally formed in attempts to exploit their extraordinary properties. [55]

Whilst examples of dark and light spots in EBIC each being found individually exist in the literature, studies presenting and comparing both are hitherto non-existent. In order to better understand and explain what was observed in the EBIC measurements subsequent CL measurements were attempted. The samples with quantum well compositions up to 68% could all be seen to show similar behaviours to the original sample studied, with blue shifted spots and increased intensity around their perimeter. An example is shown in Fig. 6.7 which shows data from a sample with 59% AlN in the quantum well and is emitting near 249nm.

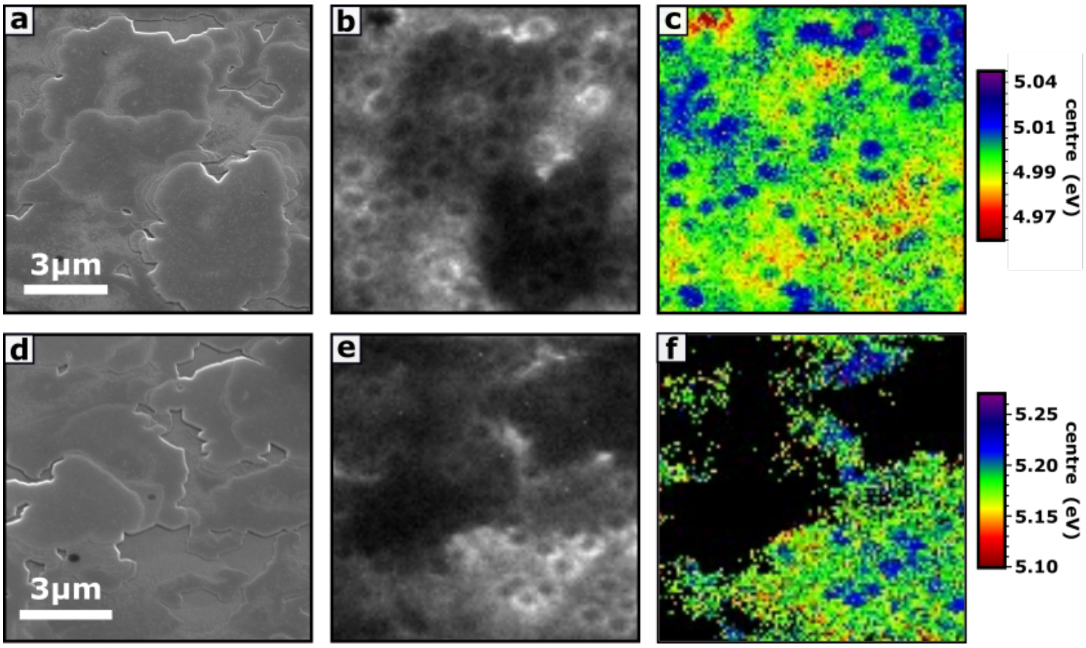

Figure 6.7: **CL measurements on TS 4780 (59% AlN) a–c and TS4782 (68% AlN) d–f. a,** SE image of the mapped area showing the thickness variations in the p-GaN. **b,** Fitted QW emission from the $Al_{0.59}Ga_{0.41}N$ layer with higher intensity seen to form rings as previously described. The areas with increased cap thickness lowering the intensity.**c,** Centre energy map of the QW peak showing blue shifts in the centre of the rings. **d,** SE image of the mapped area on TS4782. **e,** Fitted QW emission intensity shows similar behaviour to the the previous samples. **f,** Centre energy map of the QW peak. The signal from this sample is notably lower so a mask is applied to hide noisy regions and improve clarity where peak fitting has failed due to the low signal.

I found that mapping the QW emission from all of the samples was not possible due to the intensity no longer being of a measurable level above 70% AlN. The mean spectra from some of the samples are plotted in Fig. 6.8, demonstrating both the shift in emission wavelength and the rapid decrease in intensity of the QW emission as the AlN% increases. This plot does show an apparent increase in defect luminescence, but this is not the case, merely an effect of the normalisation and acquisition of the data. The lack of QW emission measured above 70% could be related to the decrease in TE component and increase in TM component of emission in this region. I was hesitant to use extreme beam currents as I did not wish to irreversibly damage the samples. Acquisition times could also not be indefinitely increased as then mapping at a useful resolution would not be feasible due to drifting and time.

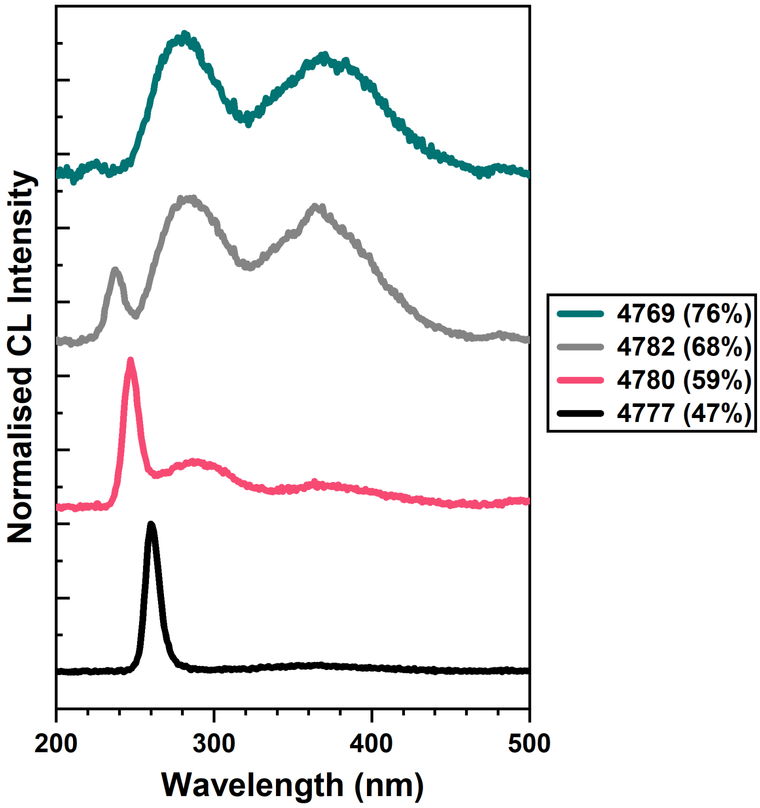

Figure 6.8: **Mean CL spectra from the samples with increasing AlN content in the active region.** The QW intensity decreases rapidly and the defect luminescence becomes more apparent.

Since CL could not be measured I attempted to measure EL from the full series. This was done to confirm if CL will be measurable or not as EL produces much more light than CL as the light is generated over such large areas. The lowest AlN% sample (TS4777) was extremely bright. So much so that concerns were raised about potential damage to various pieces of equipment within the microscope chamber. Due to the high output of light, previous EL measurements within the SEMs have been known to damage the SE detectors. However, I once again failed to measure any QW light output from the higher AlN content samples. These specimens are known from previous experiments in Berlin to be far dimmer, and the bias applied here (12 V) may have been too conservative. Some low levels of luminescence at 270 nm could be observed which are likely related to the superlatttice structure.

Since luminescence studies could not assist my investigation of the dislocation contrast in the high AlN specimens, I measured characteristic X-ray emission in the EPMA to look for the differences in the n-layers. Comparison of the X-ray maps from two n-layers shown in Fig. 6.9 finds extreme differences. The large rings have completely disappeared and a more homogeneous distribution found. The only localised increase in GaN concentration lies in small pits dotted about the surface. A more uniform material could be expected with less Ga present and closing towards a pure AlN alloy, but to this extent is surprising.

To further investigate this, AFM measurements by Marcel Schilling on two similar *n*-layers found that in the $Al_{0.95}Ga_{0.05}N$ layer that hillocks were still present, and of the same diameter but not as tall as in the $Al_{0.90}Ga_{0.1}N$ case, with the mounds being 15 nm tall compared to 25 nm tall.

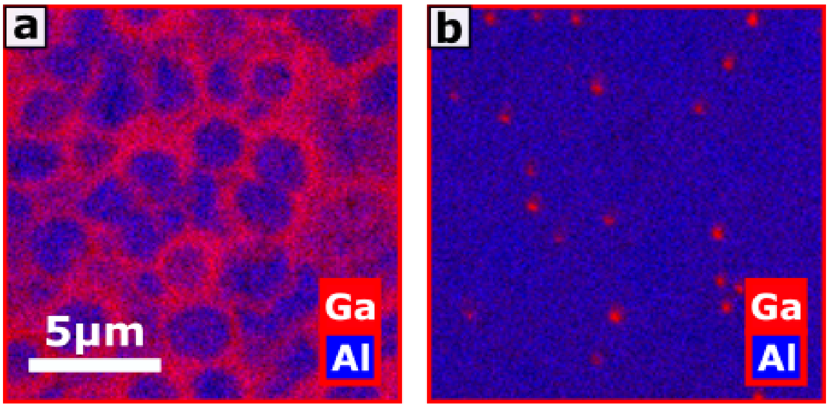

Figure 6.9: **Compositional investigation into the n-AlGaN contact layer over 15×15 μm areas. a,** Combined X-ray map from $Al_{0.9}Ga_{0.1}N$ n-contact layer showing the previously described hexagonal platelets. **b,** Combined X-ray map from $Al_{0.95}Ga_{0.05}N$ n-contact layer showing a lack of platelets but a scattering of Ga-rich spots related to surface pits instead.

6.5 Future/Present Work

Although nitrides are more resilient than other materials to the effects of threading dislocations thanks to small minority carrier diffusion lengths and random alloy localisation, my work indicates they still play a key factor in reducing device performance. [223] My results also show that the properties of the defects can be influenced depending on the composition of the heterostructure. As to why this occurs requires further investigation

I planned a set of experiments with Dr. Simon Fairclough for investigating this black/white contrast using TEM. I would map out a section of the samples (4777 and 4803) with high precision and log their location. I took the specimen to Cambridge where the FIB/SEM was used to relocate the same region, mark the region and location of the defects by depositing material on the surface (Pt). Then cutting thin cross sections for imaging in the TEM. Care was taken to ensure that these defects were bisected at a crystalographically appropriate angle for compatibility with the TEM measurements. This process can be seen in Fig.6.10

Remarkably initial images in the TEM seem to be able to identify the same defects I identified in EBIC confirming accurate mapping and sectioning. The TEM measurements allowed for confirmation of the defect type (screw) and now high resolution TEM must be completed to investigate these structures in more detail. It is hoped that this will help explain the black/white contrast of the threading dislocations observed in the EBIC. Preliminary data is shown in Fig. 6.10g–i

An unexpected observation was the relatively flat quantum well and barriers with highly distorted super lattices above. This can be seen in Fig. 6.10h. How this affects the performance of the device is currently unknown, but it could have impact on the vertical carrier transport through the device.

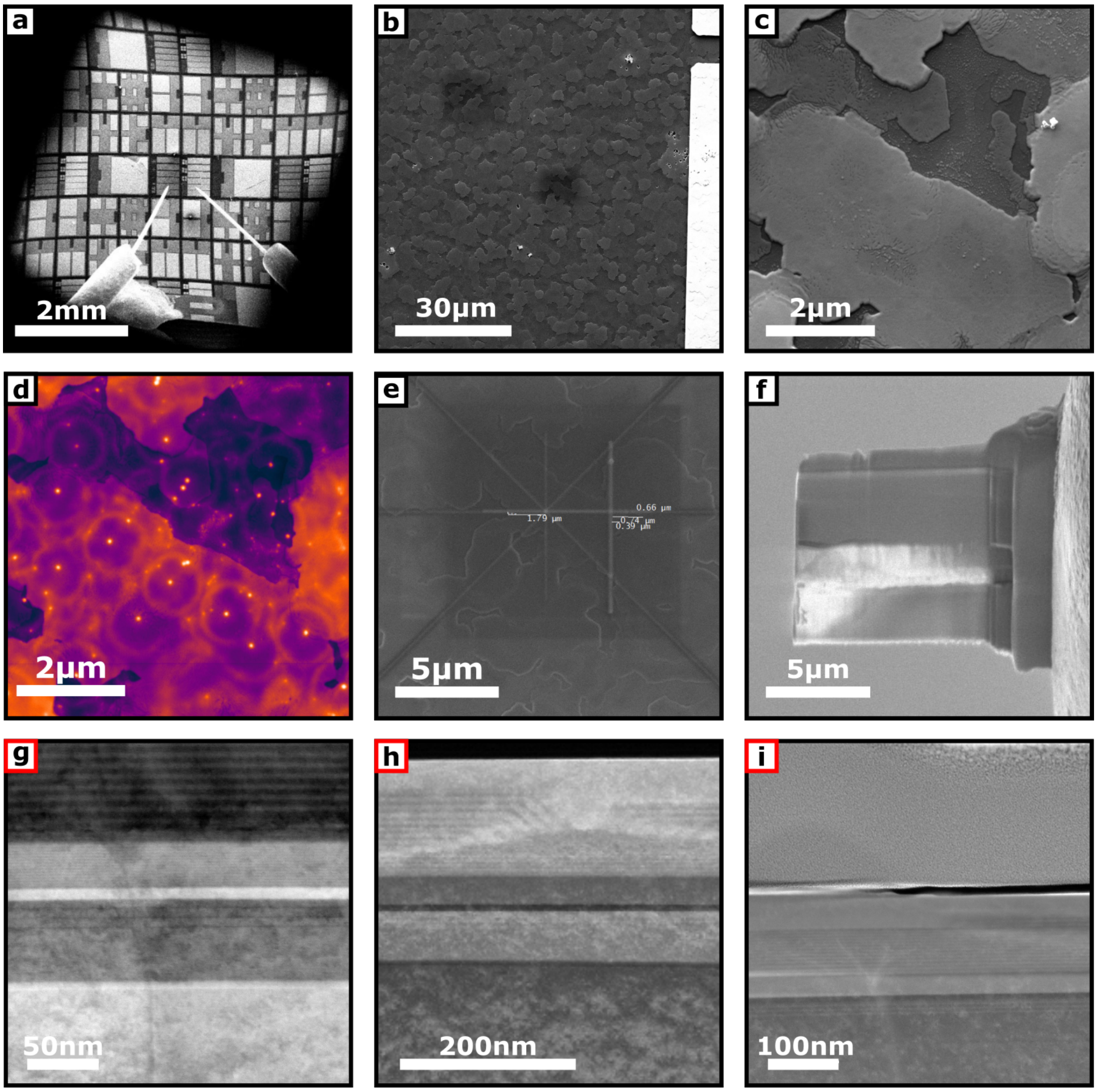

Figure 6.10: **The process of TEM lamella for investigating specific extended defects identified by EBIC within sample 4803.** This was repeated for both samples studied via TEM. **a,** Low magnification image of area of interest for reference. **b,** Increased magnification image to help in finding the location in the FIB-SEM. **c** SE image of region with suitable extended defects. **d,** EBIC image of the region shown in (c) with clear TDD. **e,** Image taken with the FIB-SEM showing the same site has been relocated. Metal markers have been deposited to help in the cut/milling. **f,** The final prepared lamella after extraction. **g,** Preliminary TEM image of a screw-type threading dislocation meandering through the epitaxial layers. **h,** Disruption in the super lattice layers. **i,** Threading dislocation appearing to split into two at one of the interfaces.

In the near future I hope to be able to provide a deeper explanation to the phenomena I have observed in EBIC measurements with the samples now prepared for TEM studies.

Chapter 7

Lateral Polarity Heterostructures

As part of the ManuGaN project I worked on characterising two lateral polarity heterostructures grown by Prof. Tao Wang's group at the University of Sheffield. These structures consist of III-nitride stripes alternating in polarity. Controlling polarity and switching it between neighbouring regions could be an important capability for advanced device development. There are potential applications for light emitting devices [287], non linear optics [288] and more novel structures such as superjunctions. [289, 290] Through a combination of scanning electron microscopy techniques I find that although the majority of the structures examined were of the intended polarity, the complex growth has lead to poor crystal quality and unwanted morphological features.

7.1 Introduction

When we discuss the polarity of a III-nitride crystal, we are essentially describing "which way is up". As previously discussed in the introductory chapter the wurtzite phase is non-centrosymmetric and the existence of axial dipoles lead to a spontaneous polarisation. The orientation of these dipoles prescribe the direction of the associated spontaneous field, which will add to or subtract from the other electric fields present in the layer. A nonzero net field can cause the QCSE, lowering recombination efficiency. This can be avoided or lessened by growing QWs on non-polar or semipolar facets, but can also be combatted by flipping the polarity of specific layers to invert their field contribution. [291] Polarisation is not always a hindrance and can be beneficial, for example in forming a 2DEG in a HEMT, and here we can utilize polarity engineering to improve device performance. [292]

Of the two polar forms of GaN, Ga-polar has previously been shown to contain lower defect populations. [293] Incorporation of non-intentional dopants such as oxygen and carbon ($\approx 10^{16}$cm^{-3} [294, 295]) is inevitable to an extent, but in larger concentrations they can be detrimental to the electrical and optical properties of the crystal. For this reason Ga-polar growth is normally used for producing high quality LED material. There is some argument to be made for N-polar LEDs as their superior indium incorporation efficiency can help mitigate some of the difficulties experienced when forming the InN rich alloys required for long wavelength emitters. [296, 297, 298]

GaN is now beginning to be utilized in commercial high power and high frequency electronics thanks to its great material qualities such as high carrier densities and breakdown voltages. [299]

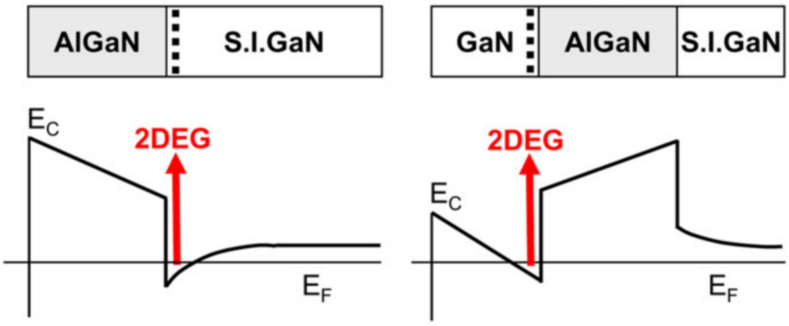

Figure 7.1: **Two examples of HEMT structures.** On left we see a Ga-polar HEMT and on the right a N-polar HEMT. The restructuring of the layers and repositioning of the 2DEG in the N-polar HEMT can improve transconductance, reduce contact resistance and more. Taken from from [298]

It is hoped that significant reductions in global power conversion losses can be made thanks to the high conductivities and the rapid switching possible speeds in GaN devices reducing switching losses. [300] These properties also allow for smaller form factor devices with lower operational temperatures and improved reliabilities to be produced.

Despite the associated higher levels of defect incorporation, N-polar material has been shown to be particularly promising for high electron mobility transistors (HEMTs). [301] In Fig.7.1 two basic HEMT structures are shown. For the N-polar structure the 2DEG is formed above the barrier, and thanks to the natural back barrier has enhanced confinement which improves output resistance and pinch-off characteristics. [302] Due to the repositioning of the 2DEG, the GaN layer lies between the ohmic contacts and the 2DEG giving a smaller bandgap barrier, which can help to reduce contact resistance. [303] Another significant benefit of N-polar GaN is the production of "normally off" or enhancement mode transistors which can simplify circuitry and produce significant energy savings. [304]

It may be desirable to switch the polarity during growth, either to create a complex multipolar heterERostructure or to overcome limitations of the substrate. However, executing such a switch is difficult, with polarity conversion/inversion methods an active area of research. By using interlayers such as $Mg_{x(3)}N_{y(2)}$, (Ga)Al-oxynitride, metallic Al, or doping highly with Mg or Ti during growth, polarity conversion have been observed. [305, 306, 307, 308, 309, 310, 311, 312, 313] However, many of these methods lead to their own issues such as facetted interfaces, dopant maldistribution and defect generation.

7.1.1 Lateral Polarity Heterostructures

By growing the two polarities in parallel we form a periodically poled crystal which can be used for many nonlinear processes such as frequency doubling. Periodically poled (PP) or periodically polarity inversed (PPI) GaN has already been shown to demonstrate second harmonic generation and could potentially be utilized in non-linear optical devices for frequency manipulation. [314]

Structures with bands of PP GaN are commonly referred to as lateral polarity heterostructures (LPHs). [288, 315, 316] The unique reaction of each domain to an applied electric field leads to the possibility of these structures also being used for multicolour electroluminescent devices. In these LPH structures each polarity domain is separated by an inversion domain boundary (IDB) as can be seen in Figure 7.2. The exact form of such IDBs is not strictly defined and may vary from sample to sample, with multiple suggested models that attempt to describe (and predict) their complex electrical and optical properties. [317]

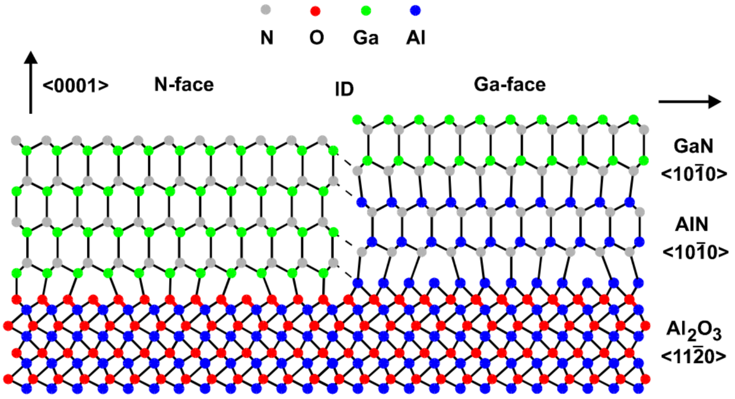

Figure 7.2: **Model crystal structure for a LPH.** Here both Ga-polar and N-polar domains separated by an inversion domain (ID) can be seen. Taken from [315]

7.1.2 Growth

If one was to grow freestanding Ga-polar GaN and flip it over it would then be N-polar GaN. One crude method to achieve this is by removing the substrate post growth, and then flipping the crystal. [318] However, the polarity during growth would determine the growth rate as well as the incorporation rates of defects and dopants.

The samples I will investigate here are grown atop sapphire substrates. The corundum structure is a member of the centrosymmetric space group 167, subsequently allowing for either metal, nitrogen or mixed polarity growth where both are present. [319] Excluding inversion methods, the polarity obtained will be predominantly determined by the growth approach (e.g MOVPE or MBE), substrate choice and the surface treatments prior to growth. [291]

“Epiready” sapphire substrates are oxygen terminated. [315] During MBE growth there is normally a low flux of N. The termination is stable against nitridation, so the first mono layer is likely to be metal. The Ga-N bonds are stronger than the Ga-O bonds and thus the first Ga layer belongs to GaN and so becomes N-polar. If Al is deposited first, the metal monolayer belongs to the substrate since Al-O bonds are stronger than Al-N bonds. For this reason a thin AlN buffer can invert the polarity to metal-polar. In MOVPE growth the N-rich conditions and higher temperatures combined with a nitridation step produce a thin AlN layer hence metal-polar material will typically form. In order to grow nitrogen polar by MOVPE, an initial surface treatment is performed.

7.1.3 Polarity Characterisation

There are multiple methods known to be able to accurately identify the polarity of a III-nitride crystal. I will briefly highlight some of the most common methods below.

Chemical Etch

Due to the unique chemical properties of the surfaces, upon exposure to a wet etch treatment both surfaces will react at differing rates and produce distinct surface morphologies. Chemicals such as phosphoric acid (H_3PO_4) [320], sodium hydroxide (NaOH) [321] and potassium hydroxide (KOH) [322, 323] have all previously been used to reveal the polarity. This method of characterisation is indirect and comes at a cost, as it will destroy the sample in the process.

Transmission Electron Microscopy

In a TEM there is a plethora of methodologies that could be used to investigate the polarity of a crystal; Diffraction based techniques like convergent beam electron diffraction (CBED) [324], spectroscopic approaches such as electron energy loss spectroscopy (EELS) [325] or even the Z-contrast from a scanning TEM (STEM) image could be analysed to reveal the polarity. [326] These TEM based techniques although capable of determining the polarity, all share some common limitations. Describing the polarity over large areas of interest (10s of μm) is not practical due to the small fields of view and the preparation of lamellae is highly destructive.

Atomic Force Microscopy

An AFM technique which can be used to identify the polarity is Kelvin probe force microscopy (KPFM). This method can distinguish between the two different surface potentials displayed by the two polarities in order to identify them. [327] Unfortunately this method is very sensitive to surface oxides as they can dramatically change the surface properties. A second AFM variant known as piezoresponse force microscopy can also be used. [328] This method involves observing the piezoelectric response of a material, i.e how much does the material deform under an applied bias, and can do so with high spatial resolution. However, problems can arise when using scanning probe techniques while working with three dimensional structures such as nanowires or ridges where the tip can easily crash.

7.2 Experimentation

Two samples were provided for investigation. They are both based on GaN, with the difference being the addition of a superlattice (SL) and multi quantum well (MQW) structure atop one. The structure with the MQW structure was produced to try observe the influence of the two polarities on the optical peformance of LEDs.

I will first discuss the simpler of the samples which contains no QWs or SL. The sample was prepared by MOVPE, initially growing a ≈180 nm thick metal polar AlN layer on sapphire. Stripes are then etched through this AlN layer down to the sapphire. Following this a brief surface treatment is carried out, then additional AlN is overgrown on both the remaining nitrogen polarity AlN and directly on the sapphire. This time the AlN directly on the sapphire will be of nitrogen polarity. The growth of these two domains although simultaneous, occur at different rates, resulting in estimated layer thicknesses of 300 nm for the nitrogen polarity and 500 nm for the metal polarity AlN. The final step is the growth of the GaN. The polarity of the GaN grown is determined by that of the substructure, although once again there is a disparity in growth rates between the polarities resulting in the ridged structure seen in Fig. 7.10. The final sample was polished (chemical-mechanical polishing) in an attempt to flatten the surface before being sent to us for characterisation.

I employed the complementary SEM based techniques of cathodoluminescence (CL) and electron backscattered diffraction (EBSD), following the non-destructive method recently demonstrated by Naresh-Kumar and Bruckbauer et al [181] to not only identify the polarity present, but also to explore the relationship between polarity and luminescence.

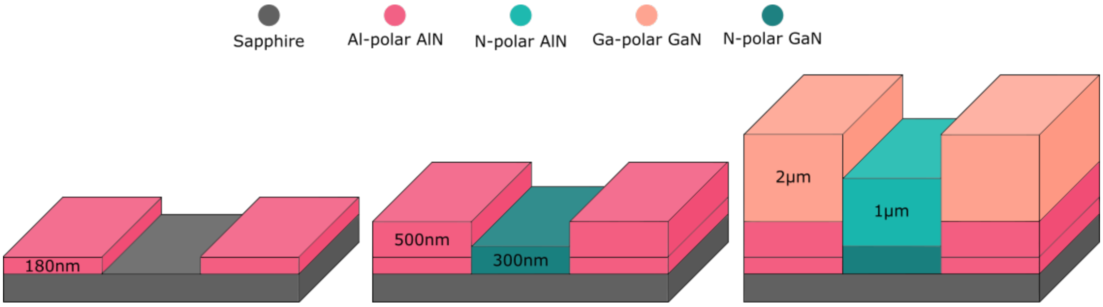

Figure 7.3: **Schematic of LPH growth structure, showing three key growth stages.** First following the growth of a thin AlN layer, stripes are etched down to the sapphire. Further AlN is overgrown following a surface treatment on both the sapphire and the metal polar AlN, resulting in two polarities grown in tandem. Finally the GaN is overgrown and takes on the polarity of the substructure.

7.2.1 Cathodoluminescence

GaN LPH

For these particular CL measurements I installed a 300 lmm^{-1} grating to give a spectral range from the band edge and across the entire visible range as I was unsure what emission energies would be present. I mapped over areas that included regions of both polarities in order to compare luminescence from the two. Although with a perfect crystal one could expect the CL spectra from each polarity to be very similar, changes in defect incorporation lead to distinctive differences as seen in Fig. 7.4.

The hyperspectral cathodoluminescence mapping allowed for some spectroscopy to be done. Averaging over a $\approx 2\times 6\,\mu$m area within each of the two distinctive domains and taking care to avoid the sidewalls of the ridge, I find similar emission peaks, but with differing intensities as can be seen in Fig. 7.4. In the N-polar region I find strong band-edge (BE) luminescence and weak yellow luminescence (YL). The opposite can be said for the Ga-polar region where I observe strong YL and weak band-edge emission.

This rather “simple” observation is actually rather difficult to explain, as the yellow luminescence (YL) in GaN remains an actively debated subject with multiple suggested perpetrators. It can be said that it is caused by some form of point defects and their shallow/deep to deep/shallow transitions. Ion implantation experiments involving up to 35 different elements have shown that most enhanced YL with the explanation that this was due to the implantation forming native defects such as V_{Ga} as opposed to the impurities themselves. [329] The involvement of V_{Ga} was thought to be likely as it is so easily formed in n-type GaN and commonly YL is decreased or even disappears in p-type GaN. Oxygen-V_{Ga} complexes had particularly strong support but more recently a carbon related defect has been found to be both theoretically and experimentally favourable. [330] It is not outwith the realms of possibility that there could in

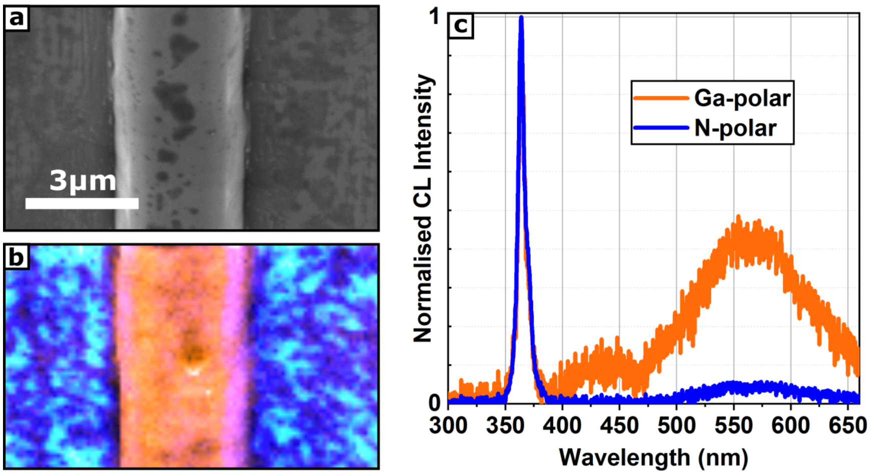

Figure 7.4: **CL investigation of the GaN LPH structure without quantum wells. a,** Shows SE image of a region of polished LPH material, with a Ga-polar ridge in the centre of the frame. **b,** A composite image formed from two components of a CL hyperspectral map, one showing the intensity of the YL between 1.95-2.35eV represented here as orange and the other a map of the band edge luminescence intensity between 3.35-3.47eV represented as blue. **c,** Averaged spectra over $2\times6\mu$m areas in both the N-polar and Ga-polar regions. Here the large differences in YL intensity when normalised to the band-edge can be seen.

fact be multiple indistinguishable contributions to the YL, which are obscured by its broad and structureless appearance.

Contrasting reports of YL/BE ratios in polar GaN are scattered throughout the literature, with some suggesting Ga-polar should have less intense YL due to lower defect incorporation rates. On the other hand, others including ourselves find that the YL is higher in Ga-polar. Many suggest that the YL is lessened in N-polar GaN due to the different point defect populations present. [331, 332] One proposed explanation relates to an increase in unintentional Si incorporation in N-polar GaN, as it has been shown that Si doping can reduce YL. [333, 334] It is theorised the Si atoms would occupy $\mathrm{Si}_{\mathrm{Ga}}$ sites reducing the number of vacancies formed during growth. However conflicting results have shown that Si incorporation can be higher in Ga-polar GaN and that Si doping can increase YL, potentially through V_{Ga}-$\mathrm{Si}_{\mathrm{Ga}}$ complexes. [293, 335].

An alternative explanation stems from work by Zywiets, Neugebauer and Scheffle [336] where they demonstrate that the migration length of Ga-adatoms on N-polar surfaces should be longer due to the particular surface dangling bonds present. On the Ga-polar surface the Ga atom must overcome three Ga-N bonds in order to migrate hence shorter migration lengths are expected which increases the likelihood of V_{Ga} formation. This concept has been used to explain experimental results regarding YL in polar GaN by Sun et al and Wang et al. [337, 338]

Both of these arguments essentially state that with more V_{Ga}'s more YL will be emitted from the sample, due to the formation of V_{Ga}-O complexes or similar allowing for the deep acceptor to shallow donor transitions. I have observed firsthand that oxygen ion implantation can increase YL in GaN in samples discussed in a recently published letter. [50] In this letter we presented evidence that this is unlikely to be related to implantation damage, as we prepared a similar series which were nitrogen implanted and which showed no increase in YL. These samples were also high temperature high pressure annealed to help repair some of the implantation damage. The importance of III-V ratio when forming V_{Ga} defects and related complexes cannot be understated and likely plays a role in the experimental discrepancies. [334]

How this all ties in with the current shift towards hypothesising carbon defects as the source of YL is unclear. [339, 340, 341, 342] The incorporation levels of carbon and the appearance of YL with regards to polarity seems not yet to have been studied in detail, although the SIMS data from Fichtenbaum shows higher C concentrations in their Ga-polar material. [295]

Many studies investigating the luminescent differences in Ga and N-polar GaN also observe a shift in the band edge emission energies (approx 28meV (3 nm)). [181] The addition of donors such as Si or O, could raise the Fermi level and cause the Moss-Burstein effect. Strain relaxation due to the different growth modes could also blue shift the emission. Unfortunately, in our measurements shown here, the resolution is not high enough for us to accurately observe such a small shift.

In the spectra shown in Fig.7.4c I note the significant contribution from an additional defect band in the blue. It has been suggested that this is caused by an acceptor of some form (Mg, Zn or Si likely). It is interesting to note that in similar LPH samples discussed by Kirste et al [343] they observed the blue luminescence to be even larger than the YL in N-polar material.

LPH with Quantum Wells and Superlattice

The second LPH structure I studied was similar to the first, but was topped with a superlattice (SL) containing 7.5nm of GaN and 3.5nm of InGaN for fifteen periods and seven QWs with 13.5nm GaN barriers and 3nm InGaN. The InGaN composition was unknown but it is likely around 20% from the CL data (b=1.43 [344]). The intention was to see if there was any clear effect on the luminescence due to the underlying LPH. Unlike the first sample, there was no polishing so as to preserve the MQW which allowed the natural surface morphologies of the two regions to be better observed. The surface here is extremely rough as seen in Fig. 7.5, although this could have been affected by the SL and MQW growth. The surface morphology in both polar domains can be seen to be far less than ideal and the angled sidewalls between the two complicate matters. On the Ga-polar mesa, a honeycomb like texture appears to form which could be related to the QW growth temperature. This interesting morphology is almost identical to that observed by Thaku [345] and Hiramatsu [108]. At low growth temperatures and high nitrogen fluxes, the limited mobility of the Ga adatoms combined with defect related diffusion barriers leads to the build up of GaN in nanowall networks. For effective In incorporation, low growth temperatures are required and could be partially to blame for the nanowall formation. [346] The N-polar region shows some hillocks which can be expected, as previously the formation of hexagonal hillocks has been seen. [343] Further explanation for our N-polar surface will be discussed with the EBSD data for reasons that will become apparent.

Across the length of the sample, there is a large evolution in surface morphologies as can be seen in Fig. 7.5. First a crack appears in the center of the N-polar region. Interestingly even when no crack is visible in the SE images, the CL maps still show a slight variation in luminescence where the crevasse would be. As we move across the sample the crevasse appears to widen to reveal another layer. Material then appears to cluster, form new nanowalls and trenches. Yet further along, a coalesced and “flat” surface materialises with large pits indicating where the domain boundaries should be. The entirety of this coalesced surface remains pitted and its luminescence is poor. None of this is is intentional. This display of competing growth modes shows some of the challenges faced when producing LPH structures. The variation could be caused by a temperature gradient across the wafer during growth or inhomogeneity in the initial AlN stripe etching.

When discussing the luminescence from this sample I will only discuss the better quality regions as outwith these areas the CL becomes highly convoluted with many emission peaks at various energies and no obvious trend. These regions corresponds to those with similar appearance to regions such as Fig. 7.5a.

I mapped the area shown in Fig. 7.6 and the corresponding panchromatic CL intensity can be seen in the overlay. I find bright spots in the N-polar region, likely related to the many strange nodules on the surface.

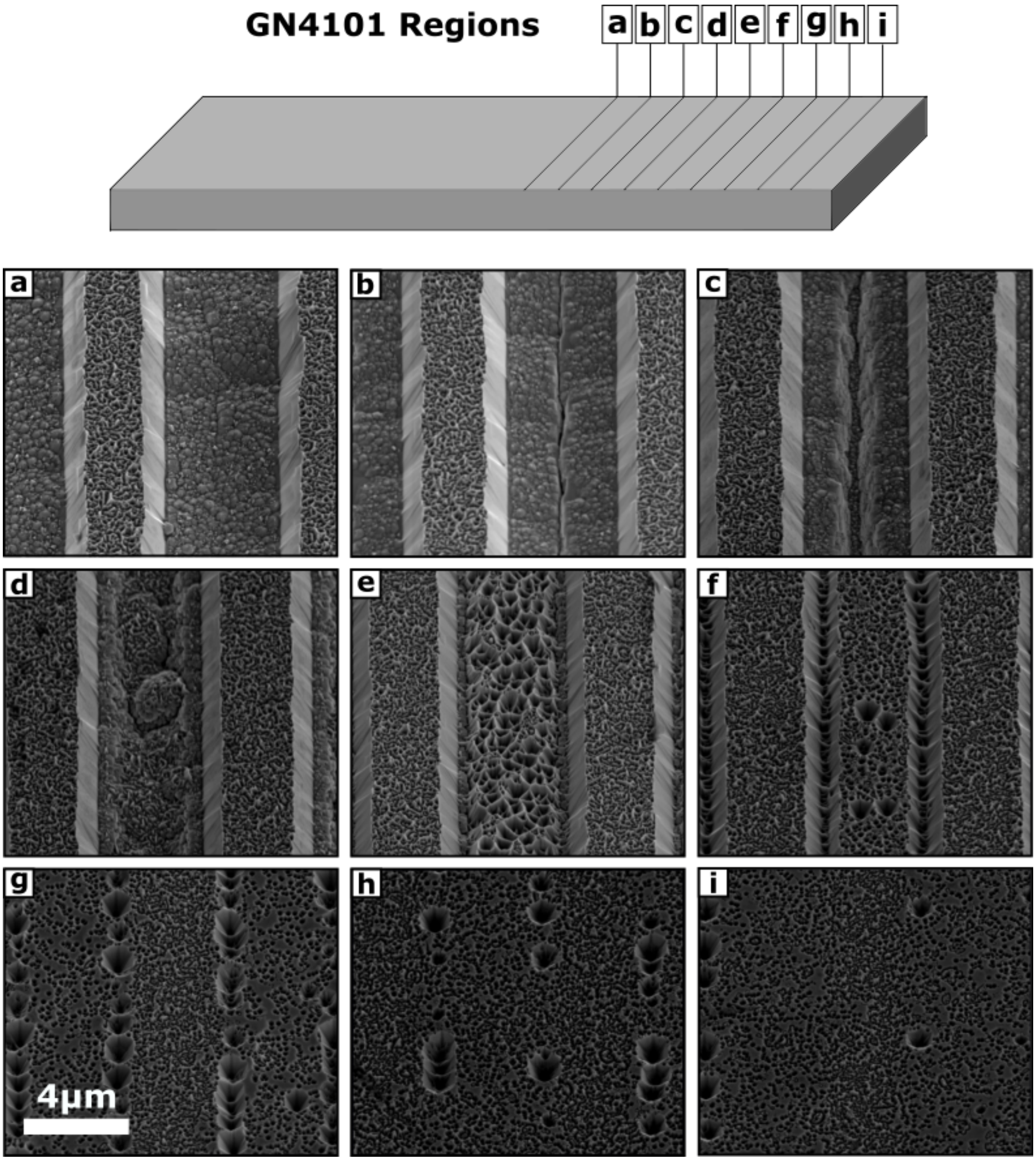

Figure 7.5: **Surface morphologies observed across the sample.** At the top of the figure a map of the sample detailing where each of the images were acquired can be found. I discovered dramatic changes in morphology and luminescence as I moved further and further along towards the edge of the specimen.

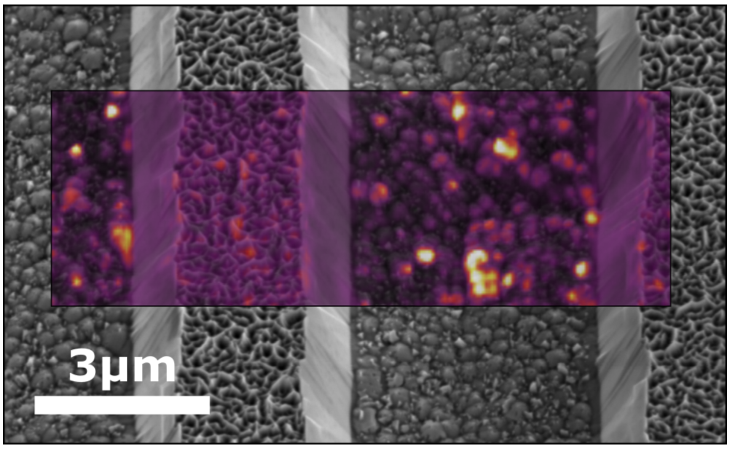

Figure 7.6: **A SE image with overlayed panchromatic CL map.** Similar intensities are seen within the two regions, but with many bright spots in the N-polar region corresponding to nodules on the surface which appear to be more concentrated in the center of the domain.

Examination of the energy centroid reveals two clear domains separated by distinct boundaries as seen in Fig. 7.7. The variation in the centre of the n-polar region as well as Fig. 7.9 alludes to the crack formation seen forming in the center of the N-polar region.

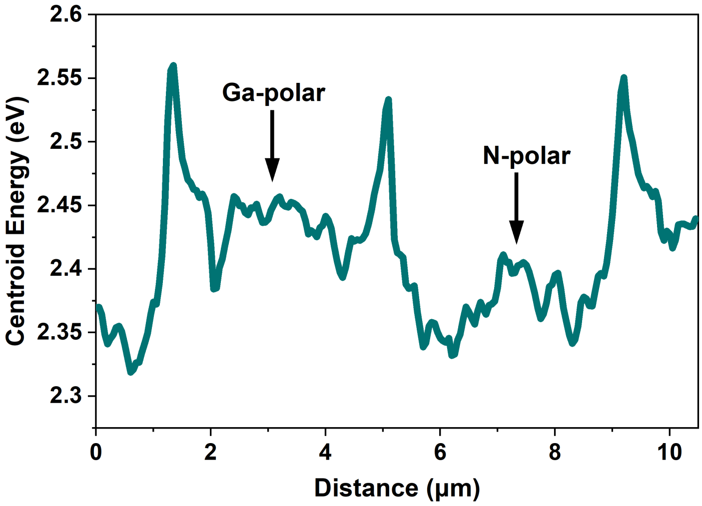

Figure 7.7: **Centroid positions across a 71 pixel line scan.** Extrema in the profile showing strong correlation to key structural points such as the semipolar sidewalls and corners between facets.

I find that the Ga-Polar region shows a single QW emission peak as expected with some slight variations in energy. However, the N-polar region displays multiple peaks as can be seen in Fig. 7.8. The lack of any clear defect or BE emission from the GaN is a positive result showing the majority of recombination is occurring in the wells. The lower intensity of QW emission in the N-polar region is not unexpected as similar inequality has been observed by Masui et al. [296] Through their temperature-dependant PL and EL measurements they find that the electric field effects are not to blame, and propose that it is due to point defects impregnating the active regions reducing the radiative recombination efficiency of the N-polar QWs.

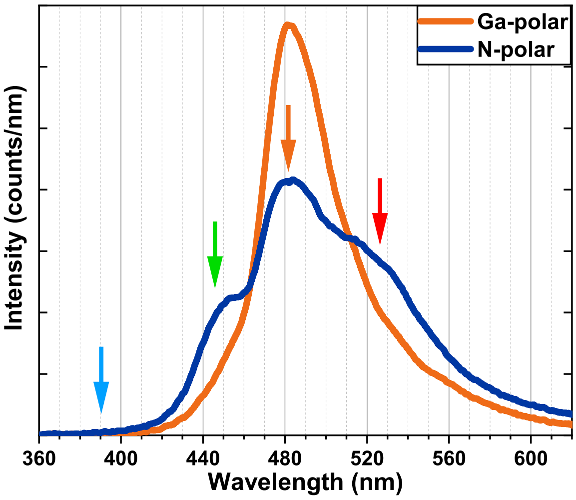

Figure 7.8: **Averaged spectra from 2×6 μm areas within the Ga-polar and N-polar regions showing significant differences in their quantum well emission.** The arrows relate to the following figure and show where the four mapped bands appear in the spectrum.

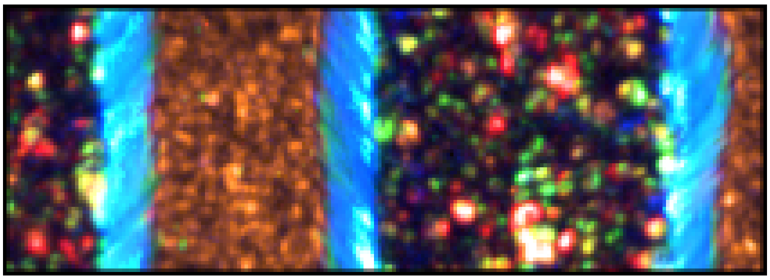

Figure 7.9: **The inhomogeneity of the N-polar regions and distinct emission from the sidewall regions are clearly visible in this four band composite image**. Filters are Blue (384-403 nm) Green (434-457 nm) Orange(469-494 nm) and Red (514-540 nm).

Explaining why there are multiple components in the N-polar region from these CL measurements alone is impossible. There are many potential causes, most of which I relate to the poor structural quality of the layers as seen in Fig. 7.10.

In the SE image shown in Fig. 7.10 clear contrast between AlN and GaN layers allows for the interface morphology to be inspected. Under the mesa structure (Ga-polar) it appears relatively smooth and flat, however under the N-polar region I observe a disturbingly turbulent and rough interface. The rougher surface of N-polar GaN has been previously been noted, although extended nitridation times could improve this. [347] This is something that should be examined to improve future iterations. Changes in well width, composition or strain, due to growth on roughened or multifaceted surfaces must be considered. It is strange that the main emission peaks from both polarities are so similar, when the InN incorporation rates are expected to differ for the two surfaces. [348] Although not performed here, EL could force distinct wavelength emission due to the unique response to the applied field in each region. An interesting observation from these images is the charging at the AlN sapphire interface below the Ga polar material only, visible as an increased brightness in the SE signal.

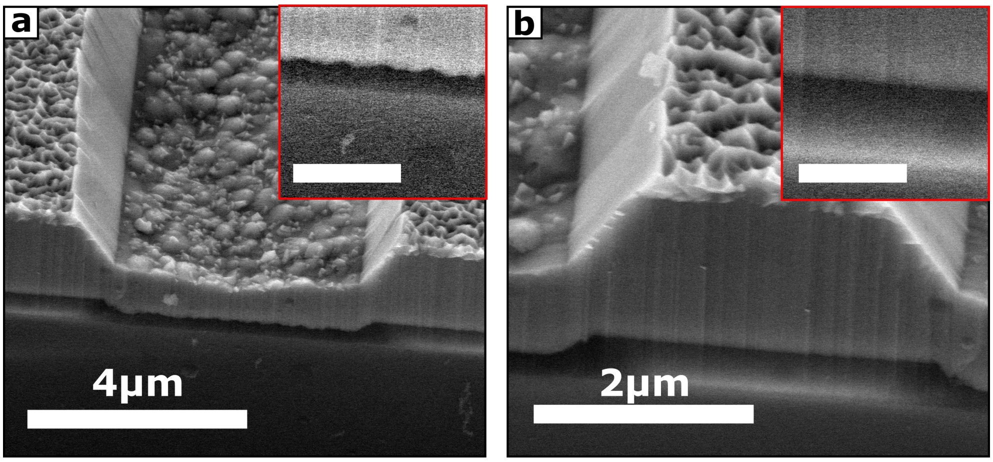

Figure 7.10: **SE images acquired at the cleaved edge of the sample.** **a,** The N-polar region which shows a rough interface between the AlN (dark) and GaN (light). This can be seen with greater clarity in the inset with enhanced contrast (1 μm scale). **b,** The Ga-polar region which appears to have a relatively smooth interface (500 nm scale bar in inset).

7.2.2 Electron Backscattered Diffraction

To confirm the polarity of the regions I turn to electron back scattered diffraction (EBSD) measurements. As previously mentioned when an electron leaves a crystal, it can diffract on its path out. When preforming EBSD measurements we capture diffraction patterns which contain structural information, allowing us to identify phases and orientations and even map them across as surface.

Measuring the polarity of GaN using EBSD has only been recently demonstrated by Naresh-Kumar and Bruckbauer et al. [181] GaN being a noncentrosymmetric system shows an inequality in Bragg reflections adjacent to specific Kikuchi bands. By comparing measured patterns to dynamically simulated patterns and investigating these intensity differences, the positive direction of the c-axis can be be determined. To the naked eye these differences are indiscernible but with computational assistance we can distinguish them. Cross correlation coefficients were compared at several points on both the ridges and valleys of the sample to ensure accuracy.

For the EBSD measurements I was assisted by those with expertise in such matters. Dr. Paul Edwards and myself acquired preliminary point EBSD patterns to show that it was indeed possible to extract patterns from our rough surfaces. EBSD measurements should be very sensitive to surface conditions due to the shallow emission range and for this reason samples are normally polished beforehand. More careful measurements, such as line scans were then taken with the help of Dr. Jochen Bruckbauer who also carried out the analysis of the acquired patterns.

Through cross-correlation of the acquired patterns it was found that the majority of each region was of the intended Ga or N-polarity. However, another interesting observation was made. Throughout the linescans and indeed in the initial point measurements, at seemingly randomly dispersed points, misaligned or even indications of alternative phases could be seen. Such was the oddness of the patterns, they could be identified by eye. These could be sporadically formed clumps of cubic material. The triangular features seen scattered across the surface in Fig 7.12 appear to be likely candidates for such clumps. Their clear morphological, geometrical and contrast difference can support a new phase. The contrast difference is caused by the crystal

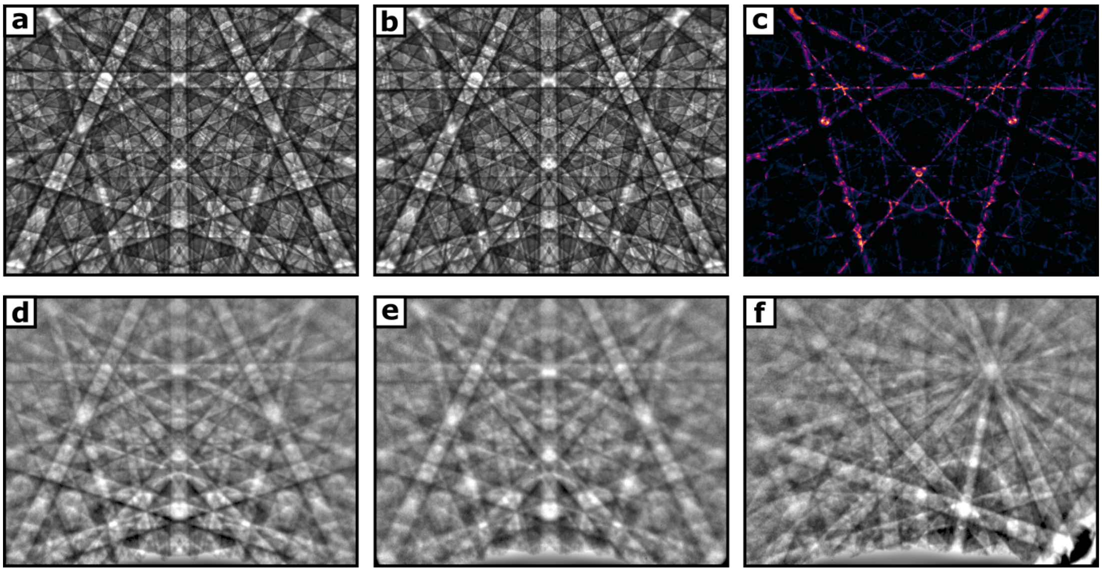

Figure 7.11: **Electron back scattered diffraction patterns (EBSP). a,** Simulated Ga polar EBSP. **b,** Simulated N-polar EBSP. **c,** Difference map of the two simulations to show the differences within the patterns. **d,** Measured EBSP from the ridge region which matches strongly to the Ga polar pattern. **e,** Measured EBSP from the valley region which matches strongly to the N polar pattern. **f,** Distinct pattern measured in the valley region showing possible misorientation.

reacting differently to the beam exposure (i.e. charge build up or lack of). Of course the contrast difference could also be caused by compositional differences, I did perform EDX mappings on these samples but no significant changes in indium concentrations could be measured due to the weak signal. The polishing of the QW free sample is unfortunate as a fair comparison of surface morphologies would have been informative. However, the lack of obvious cubic clusters in the QW free sample, suggests that this 3rd phase formation could be related the SL and MQW growth stages having detrimental effects on any subsequent crystal growth.

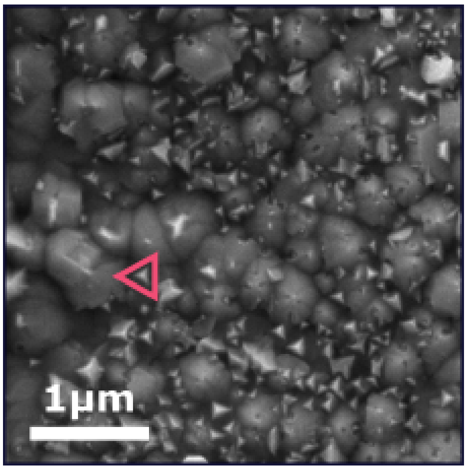

Figure 7.12: **A close up SE image of the "floor" region of the LPH.** This was determined to be mainly N-polar but certain points showing indications of a different phase. I suggest that these triangular features visible on the surface may be formations of cubic material due to their unique morphology, SE contrast and the EBSD data

7.3 Conclusion/Summary

During my investigation of these LPH samples I have observed multiple interesting behaviours. I have found that the YL is far more prominent in the Ga-polar GaN, contrary to a portion of the current literature. I explain the potential reasons for this such as C or V_{Ga} incorporation, but without further measurements we cannot be certain. With the addition of QW and SL structures I find the Ga-polar's luminescence performance is superior, showing a single strong and relatively consistent emission peak. The N-polar region shows multiple emission peaks which I suggest could be caused by the roughened interface between the AlN buffer and the GaN layer. In the N-polar region I could also find evidence of polymorphism within domain. Over the entirety of the sample I find complex growth mechanics lead to destructive effects in LPHs.

The lack of a systematic sample series renders it hard to suggest improvements on the growth of this structure. Further investigation into the cause of the large variations in morphology could be helpful. However the ridged structure with slanted sidewalls appears to be inevitable due to the growth modes present. These complex mechanics have lead to suspension of such work until better methodologies can be found or imagined.

Appendix A

Appendix 1. Tip Manufacture

One of the most important tools in nanoprobing experiments are the probe tips themselves, commonly referred to as needles. The tip diameters can vary from tens of nanometres to some microns. They are used to make local electrical contacts enabling measurement of the electron beam induced current, I-V relationship and the electroluminescence of semiconductor samples. They also allow us to apply forces to nanostructures and mechanically manipulate them. In order to do so effectively, we require the tips to be of the appropriate dimensions and composition. For electrical procedures the tip must be highly conductive, hard and well formed, however for mechanical applications these stipulations can be somewhat relaxed. Although commercial products are available, high quality small diameter needles can be costly considering their consumable nature. Making my own tips could also allow me to explore the possibility of using different materials to make tailored contacts to different surfaces. For these reasons, I explored the idea of self-manufacture and found it to be a viable option.

The needles required for probing are similar to those used in scanning tunnelling microscopy (STM [349]) and in the field emission guns of SEMs. This means that there is already an abundance of publications dealing with the production of such needles with methods including chemical and electrochemical polishing, electron beam deposition, cutting and pulling, whisker growth and ion milling techniques such as focused ion beam (FIB). [350]

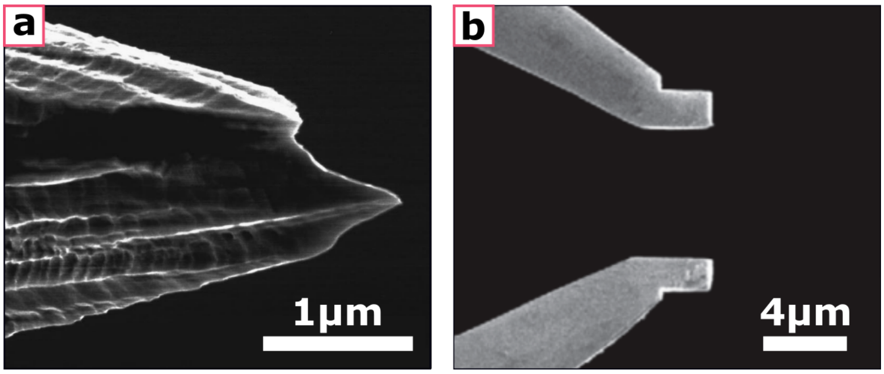

Figure A.1: **SE images of tips produced using two different methods. a,** Tip produced by Lindahl et al [351] using the cutting and pulling method for STM. It should be said that the tip seen in is not ideal for STM either as its second "peak" could act as a secondary tunnelling site causing two images to be formed simultaneously. **b,** Nanogripper produced by FIB by Kleindiek. For clarity these images are not my own.

Some of these techniques produce needles unsuitable for my uses. Cutting and pulling using clippers held at 45° produce a tip as seen in Fig. A.1a is common practice for STM. [351] The sharp asperities formed by fracturing can act as tunnelling sites enabling STM to be performed. Such tips would be highly unsuitable for my own nanoprobing experiments, as reproducing multiple similar tips is impossible due to the inherent randomness of the process.

Specialist tips such as microgrippers seen in Fig.A.1b are fabricated using FIB milling which although effective, requires specialist and costly tools. This is fine for manufacturing a one-off tool such as the gripper (such designs are available commercially) but is impractical for single consumable tips.

There are two methods of electrochemical etching/polishing commonly used and both rely on a "drop-off" mechanism (when using direct current). First there are floating layer techniques [352], which involve a thin layer of electrolyte floating atop a denser volume of inert liquid as seen in Fig. A.2b. The exact chemicals depend on the material you wish to etch. [353] This thin layer localises the etching processes to prevent the main shafts being eaten. For materials such as tungsten the floating layer technique is unnecessary, however for some elements or alloys the chemistry may be such that it is the only option. A simpler approach is to use only an electrolyte and allow natural fluid dynamics to localise the etching process. This can be seen in Fig. A.2a. I employ this second method as it avoids using harmful chemicals such as CCl_4 [352] and it is relatively simple to utilize.

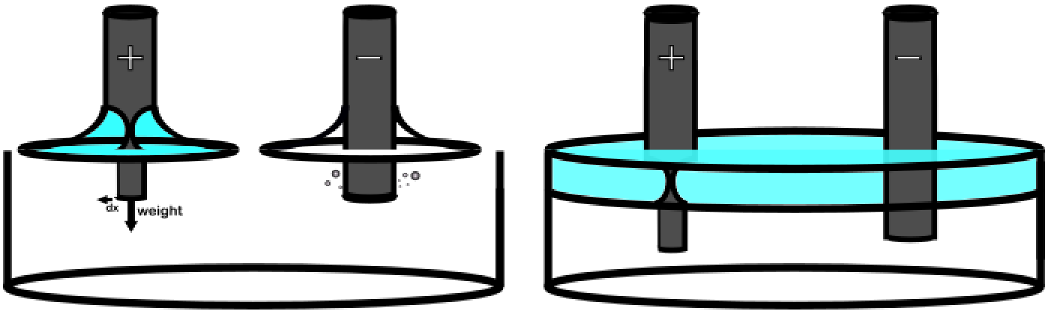

Figure A.2: **Two kinds of electrochemical etching processes, with the regions of active etching shown in blue. a,** The natural formation of a vortex thanks to the chemistry of the process enhances the etching at the meniscus. **b,** Floating a thin active layer atop another dense inactive liquid to localise the etching.

A.1 Material Properties

The material from which I craft the needles could have a large impact on the properties of the system, thus is of critical importance. Commercially available solutions include; tungsten (W), platinum-iridium (Pt-Ir) and nickel (Ni), from companies such as Mesoscope, Picoprobe, Smaract and Unisoku. To produce the best possible tools, I now review a few basic parameters to assess the suitability of metals.

Hardness

My experiments require contact between tip and samples. If the tip is too soft it will deform upon landing and result in variations in repeat electrical measurements. However, a tip that is very brittle may snap when performing force-measurements.

Melting Point

There are two reasons melting point is important. Firstly, the electron beam can cause highly localised heating. Secondly when performing electrical measurements thermoelectric effects can cause heating. Since I do not wish the tip to melt onto the sample (unintentionally) when performing experiments, a relatively high melting point is desirable. This renders materials such as Tin (with a melting point of 232°C) unsuitable. This may also be important for oxide removal as discussed later.

Conductivity

Perhaps a slightly obvious condition for electrical measurements is having a conductive tip. However, it is also important for the common electrochemical etching processes used for their manufacture.

Work Function

When considering the semiconductor metal interface, the work function of the metal is an important parameter. Metal-semiconductor contacts can fall under two categories, ohmic or Schottky. The Schottky model, however, can describe both. [354] In this model the contact barrier height is defined as:

$$\phi_B = \phi_m - \chi \tag{A.1}$$

where ϕ_m is the work function of the metal and χ is the electron affinity of the semiconductor.

From this it would be apparent that by choosing a metal with an optimal work function we could shrink the barrier, improve flow and create a more ohmic contact. In reality the relationship between barrier height and work function of the contact metal has proved to be far more complex. It is suggested that the large amounts of dangling bonds, defects and exotic states at the semiconductor surface are the root cause of Fermi level pinning. This was first described by Bardeen [355] in 1947 but is still an active area of research.

Cost

Although not exactly a stipulation from the scientific point of view, in practice the price of the materials must be reasonable enough to be considered. These items are consumable and will be exchanged and discarded frequently after being contaminated or damaged.

Chemical Stability

Nonintentional oxide layers on both metal and semiconductor surfaces can be a blight to accurate electrical characterisation. I can somewhat combat this by applying an excess of force to the tip to punch through the layers, but this is suboptimal. Certain metals are more prone to developing oxide layers at rapid rates, so avoiding these could be beneficial. For example, the alloy Pt-Ir is commonly used in STM experiments because the Pt has a very slow rate of oxide layer growth while Ir provides structural strength. However, using such alloys can complicate the required processing and add cost to the process.

A.2 Tungsten Direct Current Etching Process

The strong hardness, high melting point, decent conductivity, fair oxidation rate and cost all factored into the decision to use tungsten for producing my initial nanoprobing tips. Another more practical reason is that there is a large body of literature already describing the production of sharp tungsten needles for STM using a multitude of techniques. Pt-Ir was strongly considered but is far harder to manufacture, requiring AC sparking and a two-step process. [356]

There are three key steps in the manufacturing of tungsten tips; polishing, cleaning and storage. I begin with coils of 0.25 mm diameter 99.95% pure tungsten wire from Sigma Aldrich. This diameter is used as it fits the low current measurement kits (LCMK) on our system. I cut two roughly 4 cm lengths of wire for the etching process, with one to act as the cathode and the other the anode. Although the wire will only be submerged by a few mm, I require a longer strand in order to have clearance over the beaker rim. Any excess wire is easily trimmed before mounting in the SEM. Note that the wire installed as the cathode can be reused. Before etching I clean these wires first in methanol and then isopropyl alcohol (IPA) to try remove any dirt before mounting them in my probe-etching station. Points of contamination on the wire can disrupt the isotropy of the etching by locally increasing or decreasing etch speeds. The station enables easy dunking and electrical connections. These connections lead to the power supply and automated switch-off electronics which will be discussed in detail later in this appendix.

Before the full polishing step, I submerge the wire to a depth slightly above where the final etching will occur. Wire surfaces can initially be rough and cause similar problems to dirt, so an initial polishing step is required.

For the main polishing step a constant bias is applied until the lower section of the tip drops. At this stage I turn off the applied bias and the upper section which should now be sharp can be removed from the liquid. Latterly as the process was refined, a comparator system was introduced for automated switch off.

The electrolyte solution used for the actual etching step was 2mol/l NaOH which was prepared by dissolving 20g of NaOH pellets in 250ml of milliQ water, although KOH can alternatively be used. In a much-simplified picture, as described by Ibe et al [357], the tungsten is said to be etched by the hydroxide ions in the following reactions.

$$\text{Cathode}: 6\mathrm{H_2O} + 6e^- \longrightarrow 3\mathrm{H_2}(g) + 6\mathrm{OH^-} \tag{A.2}$$

$$\text{Anode}: \mathrm{W(s)} + 8\mathrm{OH^-} \longrightarrow \mathrm{WO_4^{2-}} + 4\mathrm{H_2O} + 6e^- \tag{A.3}$$

$$\text{Overall}: \mathrm{W(s)} + 2\mathrm{OH^-} + 2\mathrm{H_2O} \longrightarrow \mathrm{WO_4^{2-}} + 3\mathrm{H_2}(g) \tag{A.4}$$

At the anode dense $\mathrm{WO_4^{2-}}$ ions sink through the water and $\mathrm{OH^-}$ ions rise to create a vortex at the meniscus. The high hydroxide concentrations in this region accelerates the etching here. The heavy ions also act to partially insulate the main part of the lower shaft from the etchant ions. As the wire at the meniscus thins, the weight of the bottom component draws the needle even thinner before “break-off” occurs. This forms the characteristic parabolic tip shape seen in DC etching procedures. Ideally etching would cease immediately upon break-off, preserving the tip. In practice the tip remains in the etching solution under a bias slightly longer so

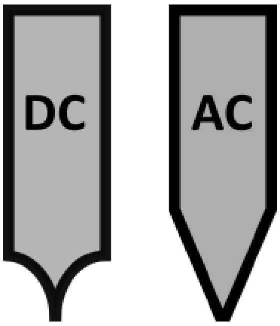

Figure A.3: **The defining profiles of AC etched tips vs DC etched tips.**

“etch-back” will occur. This is why it is important to immediately switch off the applied bias upon break-off. I automate this switch-off process using a comparator circuit discussed later. During the entirety of the polishing process, the lower section which itself has the potential to be used as a tip, is slowly eaten away. Alternative setups include a capillary tube to retrieve this section. [358] The lower segment will likely have a sharper tip than the top as it is immediately cut off from the circuit upon drop-off. The problem is that due to its continuous exposure to the solution during the polishing, its shaft diameter will be far smaller than the 0.25mm required for a tight fit in the LCMK, so I discard this segment. The loss in diameter can be avoiding using a loop method [359, 360], but when we consider the “submersion depths” involved (a few mm) it would likely be too difficult to bend these shorter tips for mounting in the SEM anyway. The diameter loss could alternatively be avoided using the floating layer method previously discussed.

A.2.1 Processing Parameters

Applied Bias

The electrochemical equations indicate that a minimum bias of 1.43V is required for polishing to occur. [360] Although in practice the value will likely exceed this. Some experimental setups utilize a natural difference in potential, such as an indium wire loop around the tungsten wire which is a difference in work function of around 800 mV. [360] However, this does not allow for an easy switch on/switch off process. I use two tungsten wires for both as cathode and anode so there is no intrinsic potential difference. Results by Chang et al [361] display the advantages of using higher bias in terms of achieving a smooth surface. However, too high a bias and the etching will be too quick, and the wire will not go through a successful drawing mechanism forcing a blunt final product. Ibe et al [357] suggest that lower biases could be used to prevent the undesirable oxide layer forming on the needle. Although if an effective post processing cleaning step is used this layer should not be an issue. This is likely a goldilocks situation where the “perfect” conditions are somewhere in the middle. To avoid etch-back one can try using a pulsed voltage setup and a check for drop-off after each pulse. Although not an avenue pursued, AC etching results in a far gentler approach to the apex. For this reason, I assume that commercially available products are produced using this method. It is also easier to mass produce tips using the AC methods which is likely why industry uses this. I did not pursue the AC etching method as obtaining the optimum processing parameters is said to be more challenging. [356]

Electrolyte Concentration

The electrolyte used in our case was NaOH, although KOH would fulfil the same purpose. Most literature recommends 1-3mol/l solutions and for this reason initial work was performed in 2mol/l solutions. A weaker concentration will result in a slower etch. Prolonged exposure to the etchant may possibly result in a porous and explain the rough tip surface as seen in Fig. A.4a.

Etching too quickly however can lead to the breakoff occurring before the tungsten has had a chance to be drawn into a sharp tip, similar to high voltage cases. The high concentration etchant will also dull the tip following break off more rapidly, which can cause issues even with automatic switch-off circuits.

Immersion Depth

The submersion depth can be controlled dynamically or statically. My current approach involves static tips and fluid levels. If the tip is placed too deep in the solution the excess weight can cause premature break off. The excessive force can cause the tip to recoil and bend. This can be seen in Fig. A.4b. The tips can also form small spheres on their ends Fig. A.4f, suggested to be caused by highly localised heating incurred by the pulling processes. [357]

If the wire is too shallow, there will not be enough weight below the meniscus to pull the tip. Therefore there will be no drop off and the entire submersed shaft will be slowly eaten by the solution. To obtain a correct height I mark the beaker with elastic bands for a liquid height and a tip depth. An ideal submersion depth of near 3mm was found through experimental trial and error. This height however can vary depending on the other parameters. Some experimental setups involve dynamic depth control to ensure the meniscus stays constant. Either the tip height is controlled with a piezo while observing the liquid-metal interface in a microscope, or the volume of liquid is adjusted to the same effect. [362] Without this, the process can produce meniscus stepping effects as seen in Fig. A.4c and d. The effect that these steps could have on my measurements is not clear.

Etch Time

The etch time is a function of multiple parameters and is a good indicator of how consistent your processing is. If the etch time is longer than expected this could indicate that the NaOH solution requires refreshing. For this reason, I added a timer function to the Arduino microcontroller of my system which is discussed in more detail later.

Cathode Shape and Material

Previous works have recommended stainless steel, iridium or carbon cathodes in various forms such as rings. I see no reason why simply using another piece of tungsten wire will not suffice. No obvious detrimental effects were observed as a result of this.

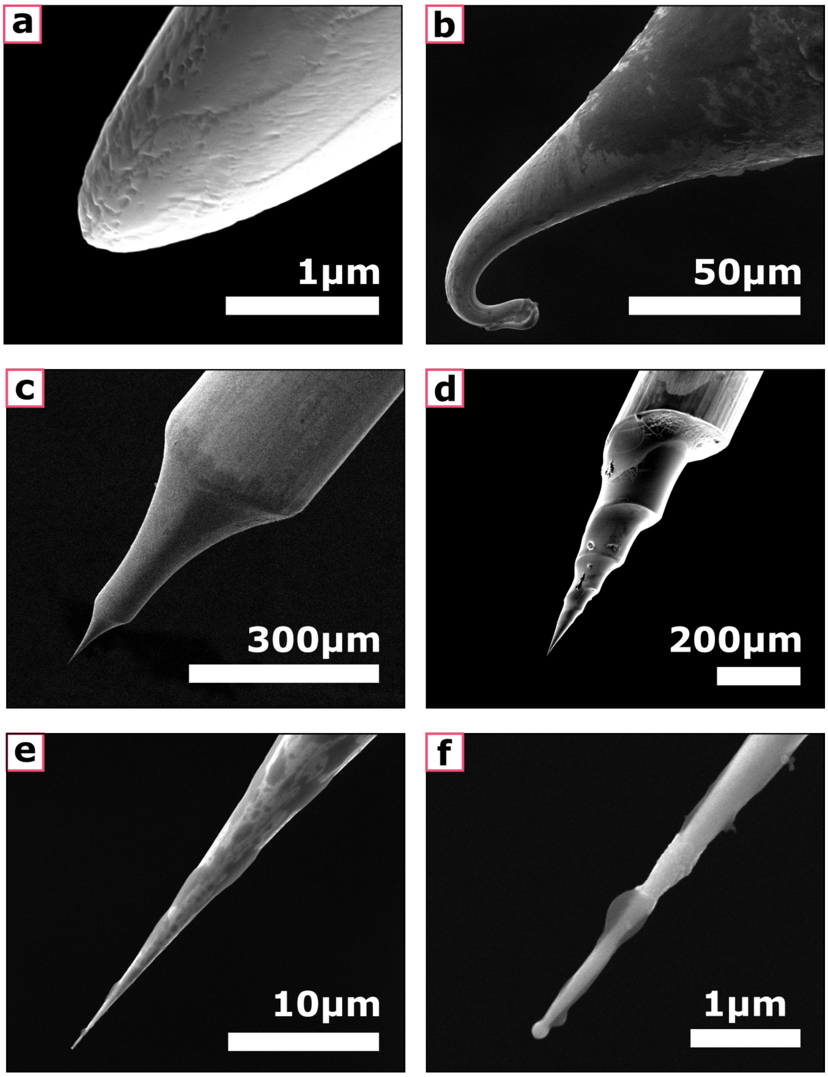

Figure A.4: **SE images showing multiple tips I have produced with various flaws. a,** Porous surface due to long etching tip and exposure to the electrolyte solution. **b,** Tip which has curled due to recoil from a harsh break off. **c,** Two step meniscus drop during etch results in this tiered effect. **d,** Example of a multi step meniscus drop. **e,** Tip which appears perfectly sharp upon first inspection. **f,** Examination of the fine tip reveals a small spherical formation due to local heating during the etch.

Switch Off Speed

If the polishing is not halted immediately after drop-off, then "etch-back" will occur blunting the tip and increasing the radius of the tip. Human reaction is not fast enough to provide an effective stop. As the needle is polished and the tip drawn, the wire becomes thinner and thinner, increasing the resistance of the circuit. This results in an increase in voltage. After drop-off, the tip can continue to be etched as the circuit has not been completely broken. In order to combat this, a rapid comparator circuit was built to sense the drop off by monitoring the bias and to cut off the power as soon as drop-off occurs. Previously other groups have found success by not just cutting off power but instead inverting the polarity to combat etching. [360] I replicated the circuits displayed in Refs [363, 357] on a breadboard, producing the circuit shown in Fig.A.5.

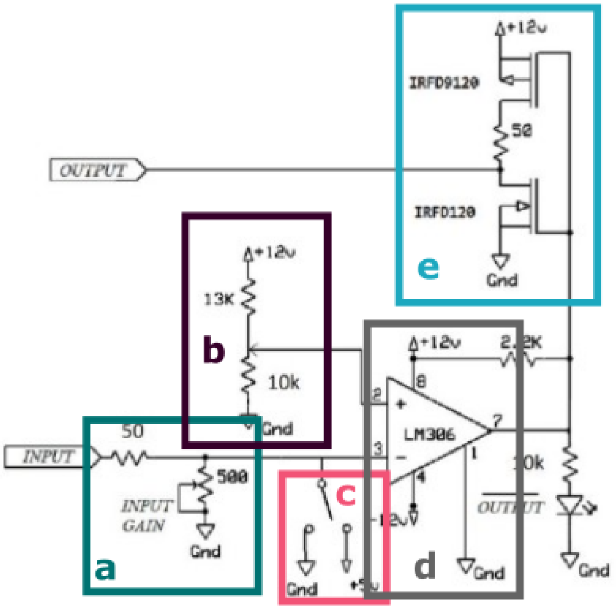

Figure A.5: **Diagram of the circuit reproduced from [363] with components labelled.** **a,** Potentiometer to control overall etching bias. **b,** Variable resistor and 12V input to create comparison voltage. **c,** 5V Kickstart switch **d,** Comparator with pull up resistor. **e,** Totem pole MOSFETs.

Arduino

After initial trials it became apparent that the system could be improved to include real time monitoring of some experimental parameters. I added an “Arduino nano every” microcontroller with an LCD screen and buzzer in order to do so. The Arduino was programmed to display the voltages at two key points in the circuit as well as the total etch time which is then saved. Once the comparator kicks in the buzzer will be triggered to alert the operator to remove the tip from the NaOH solution and dip it in a rinsing agent such as IPA or methanol. With this setup in future I hope to record the parameters used for each tip, then produce a plot of tip diameter as a function of these parameters. Utilizing this I could consistently produce tips on demand with a size appropriate for the task at hand.

A.3 Post Processing and Storage

During the electrochemical etch discussed previously I will inadvertently coat the tip in various forms of tungsten oxides. These oxide layers thicken over time with exposure to air. Therefore following the polishing, the tips should be stored in WD40/IPA [356] to minimize any further oxidation while they await SEM inspection. Upon inspection the radius of curvature and cone angles can be documented allowing for tip size binning.

To remove an oxide layer I could use a wet chemical treatment such as hydrofluoric acid (HF), however this a very dangerous compound which I would like to avoid using despite its effectiveness. [364] Alternatively I could use a hydrogen plasma, but this requires costly equipment. [365, 366] It has also been suggested that applying a bias (4-6V) over crossed tips such as in Fig. A.6b will cause removal of the oxide layer through heating and spallation. [367, 368]

My initial experiments were performed with picoprobe “100nm” radius tips. These consist of a 0.5mm tinned copper shaft with a soldered tungsten whisker tip. They arrive vacuum sealed and upon initial inspection look rather clean and smooth. After leaving exposed to the air in a plastic case for three months, the tips look far different. Fig. A.6a is an SE image showing an example of the effects of improper storage of these tips. This fluffy texture is likely the growth of a thick oxide layer, rendering this tip no longer suitable for electrical characterisation. This stresses the importance of proper storage and cleaning.

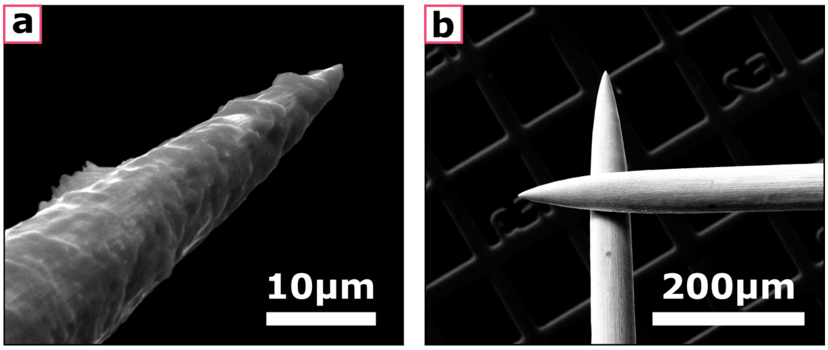

Figure A.6: **SE images showing the effect of improper tip storage and how to possibly redeem them. a,** Tip with a thick oxide layer making the surface appear fluffy. **b,** Crossed tips in contact with each other, allowing a bias to be applied and potentially remove contamination

I have not yet found a successful and simple method for recovering such tips consistently. In some cases it may be important to not only consider the cleaning of the tips, but also of various semiconductor samples I may encounter, which could be key to achieving accurate electrical measurements.

High temperature conditions are used to remove carbon and oxygen on GaAs but unfortunately this is not as effective with GaN. Dilute HCl appears to be useful for cleaning nitride surfaces. [369] Boiled HCl even more so [370]. When using HCl or HF, halogen ions will be left on the dangling bonds to prevent reoxidation. H-plasma removes these along with hydrocarbons but does not remove the oxide. [371] However, these halogen ions can be useful in helping to shift the Fermi level to create smaller barrier heights allowing for lower resistance contacts. [372] Annealing at 800° in NH_3 has been shown to produce clean surfaces.

A.4 Summary

In summary I have built an electrochemical etching station capable of manufacturing nanoprobe tips made of tungsten. Producing tips with specific diameters on demand will require further experimentation with the system to record the necessary recipes.

The polishing process involved does naturally coat the tip in a thin oxide layer which will need to be removed for electrical measurements. This can be done with hazardous chemicals, but alternatives should be explored in future. Crossing the tips may prove to be sufficient, but further measurements are required to confirm this.

Bibliography

[1] Hiroshi Amano, Y Baines, E Beam, Matteo Borga, T Bouchet, Paul R Chalker, M Charles, Kevin J Chen, Nadim Chowdhury, Rongming Chu, et al. The 2018 GaN power electronics roadmap. *Journal of Physics D: Applied Physics*, 51(16):163001, 2018. 1

[2] Cambridge Electronics article describing global power conversion losses and the role gan may play in reducing these. Accessed: 21-02-22. 1

[3] Michael Kneissl, Tae-Yeon Seong, Jung Han, and Hiroshi Amano. The emergence and prospects of deep-ultraviolet light-emitting diode technologies. *Nature Photonics*, 13(4):233–244, 2019. 1, 36

[4] MA Würtele, T Kolbe, M Lipsz, A Külberg, M Weyers, M Kneissl, and MJWR Jekel. Application of GaN-based ultraviolet-C light emitting diodes–UV LEDs–for water disinfection. *Water research*, 45(3):1481–1489, 2011. 1, 36

[5] Fedor M Kochetkov, Vladimir Neplokh, Viktoria A Mastalieva, Sungat Mukhangali, Aleksandr A Vorob'ev, Aleksandr V Uvarov, Filipp E Komissarenko, Dmitry M Mitin, Akanksha Kapoor, Joel Eymery, et al. Stretchable Transparent Light-Emitting Diodes Based on InGaN/GaN Quantum Well Microwires and Carbon Nanotube Films. *Nanomaterials*, 11(6):1503, 2021. 1

[6] Muhammad Ali Johar, Mostafa Afifi Hassan, Aadil Waseem, Jun-Seok Ha, June Key Lee, and Sang-Wan Ryu. Stable and high piezoelectric output of GaN nanowire-based lead-free piezoelectric nanogenerator by suppression of internal screening. *Nanomaterials*, 8(6):437, 2018. 1

[7] Warren C Johnson, JB Parson, and MC Crew. Nitrogen compounds of gallium. iii. *The journal of physical chemistry*, 36(10):2651–2654, 1932. 2

[8] Robert Juza and Harry Hahn. Über die kristallstrukturen von Cu_3N, GaN und InN metallamide und metallnitride. *Zeitschrift für anorganische und allgemeine Chemie*, 239(3):282–287, 1938. 2

[9] E. Fred Schubert. *Light-Emitting Diodes*. Cambridge University Press, 2 edition, 2006. 2

[10] Hiroshi Amano, Masahiro Kito, Kazumasa Hiramatsu, and Isamu Akasaki. P-type conduction in Mg-doped GaN treated with low-energy electron beam irradiation (LEEBI). *Japanese journal of applied physics*, 28(12A):L2112, 1989. 2, 6, 27

[11] Isamu Akasaki. GaN-based UV/blue light emitting devices. In *Inst. Phys. Conf. Ser.*, pages 851–856, 1992. 2

[12] Shuji Nakamura, Takashi Mukai, Masayuki Senoh, and Naruhito Iwasa. Thermal annealing effects on p-type Mg-doped GaN films. *Japanese Journal of Applied Physics*, 31(2B):L139, 1992. 2, 6

[13] Rolf E Hummel. *Electronic properties of materials*. Springer Science & Business Media, 2011. 3

[14] David B Holt and Ben G Yacobi. *Extended defects in semiconductors: electronic properties, device effects and structures*. Cambridge University Press, 2007. 3, 9, 13

[15] Masataka Higashiwaki, Robert Kaplar, Julien Pernot, and Hongping Zhao. Ultrawide bandgap semiconductors, 2021. 3

[16] MV Kurik. Urbach rule. *physica status solidi (a)*, 8(1):9–45, 1971. 3

[17] J Tauc. Absorption edge and internal electric fields in amorphous semiconductors. *Materials Research Bulletin*, 5(8):721–729, 1970. 3

[18] Hadis Morkoç. *Nitride semiconductors and devices*, volume 32. Springer Science & Business Media, 2013. 3, 4, 13

[19] Gyu-Chul Yi. *Semiconductor nanostructures for optoelectronic devices: Processing, characterization and applications*. Springer Science & Business Media, 2012. 3

[20] Joginder Singh Galsin. *Solid State Physics: An Introduction to Theory*. Academic Press, 2019. 3

[21] O Ambacher, J Smart, JR Shealy, NG Weimann, K Chu, M Murphy, WJ Schaff, LF Eastman, R Dimitrov, L Wittmer, et al. Two-dimensional electron gases induced by spontaneous and piezoelectric polarization charges in N-and Ga-face AlGaN/GaN heterostructures. *Journal of applied physics*, 85(6):3222–3233, 1999. 4

[22] F. Tuomisto, K. Saarinen, B. Lucznik, I. Grzegory, H. Teisseyre, T. Suski, S. Porowski, P. R. Hageman, and J. Likonen. Effect of growth polarity on vacancy defect and impurity incorporation in dislocation-free GaN. *Applied Physics Letters*, 86(3):1–3, 2005. 4

[23] T. Onuma, A. Uedono, H. Asamizu, H. Sato, J. F. Kaeding, M. Iza, S. P. Denbaars, S. Nakamura, and S. F. Chichibu. Photoluminescence and positron annihilation studies on Mg-doped nitrogen-polarity semipolar (1011) GaN heteroepitaxial layers grown by metalorganic vapor phase epitaxy. *Applied Physics Letters*, 96(9):8–11, 2010. 4

[24] Morteza Monavarian, Arman Rashidi, and Daniel Feezell. A Decade of Nonpolar and Semipolar III-Nitrides: A Review of Successes and Challenges. *physica status solidi (a)*, 216(1):1800628, 2019. 4

[25] Daisuke Ueda. Properties and advantages of gallium nitride. In *Power GaN Devices*, pages 1–26. Springer, 2017. 5

[26] Richard C Cramer, Erin CH Kyle, and James S Speck. Band gap bowing for high In content InAlN films. *Journal of Applied Physics*, 126(3):035703, 2019. 5, 13

[27] K Beladjal, A Kadri, K Zitouni, and K Mimouni. Bandgap bowing parameters of III-nitrides semiconductors alloys. *Superlattices and Microstructures*, 155:106901, 2021. 5

[28] Stefan Schulz, Miguel A Caro, Lay-Theng Tan, Peter J Parbrook, Robert W Martin, and Eoin P O'Reilly. Composition-dependent band gap and band-edge bowing in AlInN: A combined theoretical and experimental study. *Applied Physics Express*, 6(12):121001, 2013. 5

[29] James E Bernard and Alex Zunger. Electronic structure of ZnS, ZnSe, ZnTe, and their pseudobinary alloys. *Physical Review B*, 36(6):3199, 1987. 5

[30] Mrad Mrad, Yann Mazel, Joel Kanyandekwe, Romain Bouveyron, Guy Feuillet, and Matthew Charles. Solving the problem of gallium contamination problem in InAlN layers in close coupled showerhead reactors. *Applied Physics Express*, 12(4):045504, 2019. 5

[31] A Pandey, J Gim, R Hovden, and Z Mi. Electron overflow of AlGaN deep ultraviolet light emitting diodes. *Applied Physics Letters*, 118(24):241109, 2021. 6

[32] X Hai, RT Rashid, SM Sadaf, Z Mi, and S Zhao. Effect of low hole mobility on the efficiency droop of AlGaN nanowire deep ultraviolet light emitting diodes. *Applied Physics Letters*, 114(10):101104, 2019. 6, 36

[33] Mark J Holmes, M Arita, and Y Arakawa. III-nitride quantum dots as single photon emitters. *Semiconductor Science and Technology*, 34(3):033001, 2019. 6

[34] Xu Wang, Lei Xu, Yun Jiang, Zhouyang Yin, Christopher CS Chan, Chaoyong Deng, and Robert A Taylor. III–V compounds as single photon emitters. *Journal of Semiconductors*, 40(7):071906, 2019. 6

[35] Sebastian Tamariz, Gordon Callsen, Johann Stachurski, Kanako Shojiki, Raphaël Butté, and Nicolas Grandjean. Toward bright and pure single photon emitters at 300 K based on GaN quantum dots on silicon. *Acs Photonics*, 7(6):1515–1522, 2020. 6

[36] Shuji Nakamura, Naruhito Iwasa, Masayuki Senoh, and Takashi Mukai. Hole compensation mechanism of p-type GaN films. *Japanese Journal of Applied Physics*, 31(5R):1258, 1992. 6

[37] Hideki Sakurai, Masato Omori, Shinji Yamada, Yukihiro Furukawa, Hideo Suzuki, Tetsuo Narita, Keita Kataoka, Masahiro Horita, Michal Bockowski, Jun Suda, et al. Highly effective activation of Mg-implanted p-type GaN by ultra-high-pressure annealing. *Applied Physics Letters*, 115(14):142104, 2019. 6

[38] H Obloh, KH Bachem, U Kaufmann, M Kunzer, M Maier, A Ramakrishnan, and P Schlotter. Self-compensation in Mg doped p-type GaN grown by MOCVD. *Journal of Crystal Growth*, 195(1-4):270–273, 1998. 6

[39] Joshua S Harris, Jonathon N Baker, Benjamin E Gaddy, Isaac Bryan, Zachary Bryan, Kelsey J Mirrielees, Pramod Reddy, Ramón Collazo, Zlatko Sitar, and Douglas L Irving. On compensation in Si-doped AlN. *Applied Physics Letters*, 112(15):152101, 2018. 7

[40] T Mattila and Risto M Nieminen. Ab initio study of oxygen point defects in GaAs, GaN, and AlN. *Physical Review B*, 54(23):16676, 1996. 7

[41] T Mattila and Risto M Nieminen. Point-defect complexes and broadband luminescence in GaN and AlN. *Physical Review B*, 55(15):9571, 1997. 7

[42] Zachary Bryan, Marc Hoffmann, James Tweedie, Ronny Kirste, Gordon Callsen, Isaac Bryan, Anthony Rice, Milena Bobea, Seiji Mita, Jinqiao Xie, et al. Fermi level Control of point defects during growth of Mg-doped GaN. *Journal of electronic materials*, 42(5):815–819, 2013. 7

[43] Yu Zhou, Ziyu Wang, Abdullah Rasmita, Sejeong Kim, Amanuel Berhane, Zoltán Bodrog, Giorgio Adamo, Adam Gali, Igor Aharonovich, and Wei-bo Gao. Room temperature solid-state quantum emitters in the telecom range. *Science advances*, 4(3):eaar3580, 2018. 7

[44] Yongzhou Xue, Hui Wang, Nan Xie, Qian Yang, Fujun Xu, Bo Shen, Jun-jie Shi, Desheng Jiang, Xiuming Dou, Tongjun Yu, et al. Single-photon emission from point defects in aluminum nitride films. *The Journal of Physical Chemistry Letters*, 11(7):2689–2694, 2020. 7

[45] Gang Zhang, Yuan Cheng, Jyh-Pin Chou, and Adam Gali. Material platforms for defect qubits and single-photon emitters. *Applied Physics Reviews*, 7(3):031308, 2020. 7

[46] JB Varley, A Janotti, and CG Van de Walle. Defects in AlN as candidates for solid-state qubits. *Physical Review B*, 93(16):161201, 2016. 7

[47] Khang Hoang. Tuning the valence and concentration of europium and luminescence centers in GaN through co-doping and defect association. *Physical Review Materials*, 5(3):034601, 2021. 7, 8

[48] Michael A Reshchikov and Hadis Morkoç. Luminescence properties of defects in GaN. *Journal of applied physics*, 97(6):5–19, 2005. 8

[49] Kevin Peter O'Donnell and Volkmar Dierolf. *Rare-earth doped III-nitrides for optoelectronic and spintronic applications*, volume 124. Springer Science & Business Media, 2010. 8

[50] D Cameron, KP O'Donnell, PR Edwards, M Peres, K Lorenz, MJ Kappers, and M Boćkowski. Acceptor state anchoring in gallium nitride. *Applied Physics Letters*, 116(10):102105, 2020. 8, 74

[51] Benjamin Car, Lucile Veissier, Anne Louchet-Chauvet, J-L Le Gouët, and Thierry Chanelière. Selective optical addressing of nuclear spins through superhyperfine interaction in rare-earth doped solids. *Physical review letters*, 120(19):197401, 2018. 8

[52] EB Yakimov, PS Vergeles, AY Polyakov, In-Hwan Lee, and SJ Pearton. Movement of basal plane dislocations in GaN during electron beam irradiation. *Applied Physics Letters*, 106(13):132101, 2015. 8, 27

[53] Francesco Montalenti, Fabrizio Rovaris, Roberto Bergamaschini, Leo Miglio, Marco Salvalaglio, Giovanni Isella, Fabio Isa, and Hans Von Känel. Dislocation-Free SiGe/Si Heterostructures. *Crystals*, 8(6):257, 2018. 8

[54] Christophe A Hurni, Aurelien David, Michael J Cich, Rafael I Aldaz, Bryan Ellis, Kevin Huang, Anurag Tyagi, Remi A DeLille, Michael D Craven, Frank M Steranka, et al. Bulk GaN flip-chip violet light-emitting diodes with optimized efficiency for high-power operation. *Applied Physics Letters*, 106(3):031101, 2015. 8

[55] Joseph Kioseoglou, Efterpi Kalesaki, Imad Belabbas, Jun Chen, Gerard Nouet, Holm Kirmse, Wolfgang Neumann, Ph Komninou, and Th Karakostas. Screw threading dislocations in AlN: Structural and electronic properties of In and O doped material. *Journal of Applied Physics*, 110(5):053715, 2011. 9, 64, 65

[56] Fabien CP Massabuau, Sneha L Rhode, Matthew K Horton, Thomas J O'Hanlon, András Kovács, Marcin S Zielinski, Menno J Kappers, Rafal E Dunin-Borkowski, Colin J Humphreys, and Rachel A Oliver. Dislocations in AlGaN: Core structure, atom segregation, and optical properties. *Nano letters*, 17(8):4846–4852, 2017. 9

[57] Jonas Lähnemann, Uwe Jahn, Oliver Brandt, Timur Flissikowski, Pinar Dogan, and Holger T Grahn. Luminescence associated with stacking faults in GaN. *Journal of Physics D: Applied Physics*, 47(42):423001, 2014. 9

[58] Oana Cojocaru-Mirédin, Mohit Raghuwanshi, Roland Wuerz, and Sascha Sadewasser. Grain Boundaries in Cu (In, Ga) Se2: A Review of Composition–Electronic Property Relationships by Atom Probe Tomography and Correlative Microscopy. *Advanced Functional Materials*, 31(41):2103119, 2021. 9

[59] Ian Rousseau, Gordon Callsen, Gwénolé Jacopin, Jean-François Carlin, Raphaël Butté, and Nicolas Grandjean. Optical absorption and oxygen passivation of surface states in III-nitride photonic devices. *Journal of Applied Physics*, 123(11):113103, 2018. 9

[60] Raymond T Tung. The physics and chemistry of the Schottky barrier height. *Applied Physics Reviews*, 1(1):011304, 2014. 9

[61] SJ Pearton, JC Zolper, RJ Shul, and F Ren. GaN: Processing, defects, and devices. *Journal of applied physics*, 86(1):1–78, 1999. 10

[62] Hajime Fujikura, Takehiro Yoshida, Masatomo Shibata, and Yohei Otoki. Recent progress of high-quality GaN substrates by HVPE method. In *Gallium Nitride Materials and Devices XII*, volume 10104, page 1010403. International Society for Optics and Photonics, 2017. 10

[63] M Bockowski, M Iwinska, M Amilusik, M Fijalkowski, B Lucznik, and T Sochacki. Challenges and future perspectives in HVPE-GaN growth on ammonothermal GaN seeds. *Semiconductor Science and Technology*, 31(9):093002, 2016. 10

[64] Rodney Pelzel. A comparison of MOVPE and MBE growth technologies for III-V epitaxial structures. In *CS MANTECH Conference*, pages 105–108. New Orleans Louisiana, USA, 2013. 10

[65] Jia Guo, Guowang Li, Faiza Faria, Yu Cao, Ronghua Wang, Jai Verma, Xiang Gao, Shiping Guo, Edward Beam, Andrew Ketterson, et al. MBE-Regrown Ohmics in InAlN HEMTs With a Regrowth Interface Resistance of 0.05mm. *IEEE Electron device letters*, 33(4):525–527, 2012. 10

[66] Bogdan-Florin Spiridon, Miles Toon, Alexander Hinz, Saptarsi Ghosh, SM Fairclough, BJE Guilhabert, MJ Strain, IM Watson, Martin D Dawson, DJ Wallis, et al. Method for inferring the mechanical strain of GaN-on-Si epitaxial layers using optical profilometry and finite element analysis. *Optical Materials Express*, 11(6):1643–1655, 2021. 10

[67] Hiroshi Amano. Nobel Lecture: Growth of GaN on sapphire via low-temperature deposited buffer layer and realization of p-type GaN by Mg doping followed by low-energy electron beam irradiation. *Reviews of Modern Physics*, 87(4):1133, 2015. 10

[68] Hiroshi Amano, N Sawaki, I Akasaki, and Y Toyoda. Metalorganic vapor phase epitaxial growth of a high quality GaN film using an AlN buffer layer. *Applied Physics Letters*, 48(5):353–355, 1986. 10

[69] Hiroshi Amano, Isamu Akasaki, Kazumasa Hiramatsu, Norikatsu Koide, and Nobuhiko Sawaki. Effects of the buffer layer in metalorganic vapour phase epitaxy of GaN on sapphire substrate. *Thin Solid Films*, 163:415–420, 1988. 10

[70] G Brendan Cross, Zaheer Ahmad, Daniel Seidlitz, Mark Vernon, Nikolaus Dietz, Daniel Deocampo, Daniel Gebregiorgis, Sidong Lei, and Alexander Kozhanov. Kinetically stabilized high-temperature InN growth. *Journal of Crystal Growth*, 536:125574, 2020. 10

[71] Lok Yi Lee. Cubic zincblende gallium nitride for green-wavelength light-emitting diodes. *Materials Science and Technology*, 33(14):1570–1583, 2017. 10

[72] Shubhra S Pasayat, Chirag Gupta, Matthew S Wong, Yifan Wang, Shuji Nakamura, Steven P Denbaars, Stacia Keller, and Umesh K Mishra. Growth of strain-relaxed InGaN on micrometer-sized patterned compliant GaN pseudo-substrates. *Applied Physics Letters*, 116(11):111101, 2020. 11

[73] Matthias Auf Der Maur, Alessandro Pecchia, Gabriele Penazzi, Walter Rodrigues, and Aldo Di Carlo. Efficiency drop in green InGaN/GaN light emitting diodes: The role of random alloy fluctuations. *Physical review letters*, 116(2):027401, 2016. 11

[74] TM Smeeton, Menno J Kappers, JS Barnard, ME Vickers, and Colin J Humphreys. Electron-beam-induced strain within InGaN quantum wells: False indium “cluster” detection in the transmission electron microscope. *Applied Physics Letters*, 83(26):5419–5421, 2003. 11, 27

[75] Bastien Bonef, Massimo Catalano, Cory Lund, Steven P Denbaars, Shuji Nakamura, Umesh K Mishra, Moon J Kim, and Stacia Keller. Indium segregation in N-polar InGaN quantum wells evidenced by energy dispersive X-ray spectroscopy and atom probe tomography. *Applied Physics Letters*, 110(14):143101, 2017. 11

[76] Tongtong Zhu, David Gachet, Fengzai Tang, Wai Yuen Fu, Fabrice Oehler, Menno J Kappers, Phil Dawson, Colin J Humphreys, and Rachel A Oliver. Local carrier recombination and associated dynamics in m-plane InGaN/GaN quantum wells probed by picosecond cathodoluminescence. *Applied Physics Letters*, 109(23):232103, 2016. 11

[77] Shigefusa F Chichibu, Akira Uedono, Takeyoshi Onuma, Benjamin A Haskell, Arpan Chakraborty, Takahiro Koyama, Paul T Fini, Stacia Keller, Steven P Denbaars, James S Speck, et al. Origin of defect-insensitive emission probability in In-containing (Al, In, Ga) N alloy semiconductors. *Nature materials*, 5(10):810–816, 2006. 11

[78] K Hiramatsu, Y Kawaguchi, M Shimizu, N Sawaki, T Zheleva, Robert F Davis, H Tsuda, W Taki, N Kuwano, and K Oki. The composition pulling effect in MOVPE grown InGaN

on GaN and AlGaN and its TEM characterization. *Materials Research Society Internet Journal of Nitride Semiconductor Research*, 2, 1997. 11

[79] S Pereira, MR Correia, E Pereira, KP O'donnell, C Trager-Cowan, F Sweeney, and E Alves. Compositional pulling effects in $\text{In}_x\text{Ga}_{1-x}\text{N}$/GaN layers: A combined depth-resolved cathodoluminescence and Rutherford backscattering/channeling study. *Physical Review B*, 64(20):205311, 2001. 11

[80] T Detchprohm, Xiaohang Li, S-C Shen, PD Yoder, and RD Dupuis. III-N wide bandgap deep-ultraviolet lasers and photodetectors. In *Semiconductors and Semimetals*, volume 96, pages 121–166. Elsevier, 2017. 11, 58

[81] Jing Li, Ki-Bum Nam, Mim Lal Nakarmi, Joung-Yol Lin, HX Jiang, Pierre Carrier, and Su-Huai Wei. Band structure and fundamental optical transitions in wurtzite AlN. *Applied Physics Letters*, 83(25):5163–5165, 2003. 11, 13

[82] Tim Kolbe, Arne Knauer, Chris Chua, Zhihong Yang, Sven Einfeldt, Patrick Vogt, Noble M Johnson, Markus Weyers, and Michael Kneissl. Optical polarization characteristics of ultraviolet (In)(Al) GaN multiple quantum well light emitting diodes. *Applied Physics Letters*, 97(17):171105, 2010. 11

[83] RG Banal, M Funato, and Y Kawakami. Optical anisotropy in [0001]-oriented $\text{Al}_x\text{Ga}_{1-x}\text{N}$/AlN quantum wells (x¿ 0.69). *Physical Review B*, 79(12):121308, 2009. 11

[84] Hideki Hirayama, Noritoshi Maeda, Sachie Fujikawa, Shiro Toyoda, and Norihiko Kamata. Recent progress and future prospects of AlGaN-based high-efficiency deep-ultraviolet light-emitting diodes. *Japanese Journal of Applied Physics*, 53(10):100209, 2014. 11

[85] Gunnar Kusch, Johannes Enslin, Lucia Spasevski, Tolga Teke, Tim Wernicke, Paul R Edwards, Michael Kneissl, and Robert W Martin. Influence of InN and AlN concentration on the compositional inhomogeneity and formation of InN-rich regions in In x Al y Ga1-x- y N. *Japanese Journal of Applied Physics*, 58(SC):SCCB18, 2019. 11

[86] Tz-Jun Kuo, Chi-Liang Kuo, Chun-Hong Kuo, and Michael H Huang. Growth of core-shell Ga- GaN nanostructures via a conventional reflux method and the formation of hollow GaN spheres. *The Journal of Physical Chemistry C*, 113(9):3625–3630, 2009. 11

[87] Irene Manglano Clavero, Christoph Margenfeld, Jonas Quatuor, Hendrik Spende, Lukas Peters, Ulrich T Schwarz, and Andreas Waag. Gradients in Three-Dimensional Core–Shell GaN/InGaN Structures: Optimization and Physical Limitations. *ACS Applied Materials & Interfaces*, 2022. 11

[88] KH Li, X Liu, Q Wang, S Zhao, and Z Mi. Ultralow-threshold electrically injected AlGaN nanowire ultraviolet lasers on Si operating at low temperature. *Nature Nanotechnology*, 10(2):140–144, 2015. 11

[89] Rachel A Oliver, G Andrew D Briggs, Menno J Kappers, Colin J Humphreys, Shazia Yasin, James H Rice, Jonathon D Smith, and Robert A Taylor. InGaN quantum dots grown by metalorganic vapor phase epitaxy employing a post-growth nitrogen anneal. *Applied Physics Letters*, 83(4):755–757, 2003. 11

[90] Thobeka Kente and Sabelo Dalton Mhlanga. Gallium nitride nanostructures: Synthesis, characterization and applications. *Journal of Crystal Growth*, 444:55–72, 2016. 11

[91] Stephen D Hersee, Xinyu Sun, and Xin Wang. The controlled growth of GaN nanowires. *Nano letters*, 6(8):1808–1811, 2006. 11

[92] Tevye R Kuykendall, M Virginia P Altoe, D Frank Ogletree, and Shaul Aloni. Catalyst-directed crystallographic orientation control of GaN nanowire growth. *Nano letters*, 14(12):6767–6773, 2014. 11

[93] Jing-Yang Chung, Zhang Li, Sarah A Goodman, Jinkyu So, Govindo J Syaranamual, Tara P Mishra, Eugene A Fitzgerald, Michel Bosman, Kenneth Lee, Stephen J Pennycook, et al. Light-Emitting V-Pits: An Alternative Approach toward Luminescent Indium-Rich InGaN Quantum Dots. *ACS Photonics*, 8(10):2853–2860, 2021. 11

[94] Tim J Puchtler, Tong Wang, Christopher X Ren, Fengzai Tang, Rachel A Oliver, Robert A Taylor, and Tongtong Zhu. Ultrafast, polarized, single-photon emission from m-plane InGaN quantum dots on GaN nanowires. *Nano letters*, 16(12):7779–7785, 2016. 11

[95] C Tessarek, M Heilmann, E Butzen, A Haab, H Hardtdegen, C Dieker, E Spiecker, and S Christiansen. The role of Si during the growth of GaN micro-and nanorods. *Crystal growth & design*, 14(3):1486–1492, 2014. 11

[96] Ratan Debnath, Jong-Yoon Ha, Baomei Wen, Dipak Paramanik, Abhishek Motayed, Matthew R King, and Albert V Davydov. Top-down fabrication of large-area GaN micro-and nanopillars. *Journal of Vacuum Science & Technology B, Nanotechnology and Microelectronics: Materials, Processing, Measurement, and Phenomena*, 32(2):021204, 2014. 11

[97] Pierre-Marie Coulon, Gunnar Kusch, Robert W Martin, and Philip A Shields. Deep UV emission from highly ordered AlGaN/AlN core–shell nanorods. *ACS applied materials & interfaces*, 10(39):33441–33449, 2018. 12, 37, 38, 43

[98] Kevin J Chen, Oliver Häberlen, Alex Lidow, Chun lin Tsai, Tetsuzo Ueda, Yasuhiro Uemoto, and Yifeng Wu. GaN-on-Si power technology: Devices and applications. *IEEE Transactions on Electron Devices*, 64(3):779–795, 2017. 12

[99] Michel Khoury, Olivier Tottereau, Guy Feuillet, Philippe Vennéguès, and Jesus Zúñiga-Pérez. Evolution and prevention of meltback etching: Case study of semipolar GaN growth on patterned silicon substrates. *Journal of Applied Physics*, 122(10):105108, 2017. 12

[100] J-H Ryou. *Gallium nitride (GaN) on sapphire substrates for visible LEDs*. Elsevier, 2014. 12

[101] Wolfspeed article describing the applications of gan on sic. Accessed: 13-01-22. 12

[102] Yan Zhou, Julian Anaya, James Pomeroy, Huarui Sun, Xing Gu, Andy Xie, Edward Beam, Michael Becker, Timothy A Grotjohn, Cathy Lee, and Martin Kuball. Barrier-layer optimization for enhanced GaN-on-diamond device cooling. *ACS applied materials & interfaces*, 9(39):34416–34422, 2017. 12

[103] Andreas Liudi Mulyo, Anjan Mukherjee, Ida Marie Høiaas, Lyubomir Ahtapodov, Tron Arne Nilsen, Havard Hem Toftevaag, Per Erik Vullum, Katsumi Kishino, Helge Weman, and Bjørn-Ove Fimland. Graphene-Based Transparent Conducting Substrates for GaN/AlGaN Nanocolumn Flip-Chip Ultraviolet Light-Emitting Diodes. *ACS Applied Nano Materials*, 4(9):9653–9664, 2021. 12

[104] A Mazid Munshi, Dong-Chul Kim, Carl Philip Heimdal, Martin Heilmann, Silke H Christiansen, Per Erik Vullum, Antonius TJ van Helvoort, and Helge Weman. Selective area growth of AlGaN nanopyramid arrays on graphene by metal-organic vapor phase epitaxy. *Applied Physics Letters*, 113(26):263102, 2018. 12

[105] Claudio R Miskys, Michael K Kelly, Oliver Ambacher, and Martin Stutzmann. Freestanding GaN-substrates and devices. *physica status solidi (c)*, (6):1627–1650, 2003. 12

[106] Hajime Fujikura, Taichiro Konno, Takehiro Yoshida, and Fumimasa Horikiri. Hydride-vapor-phase epitaxial growth of highly pure GaN layers with smooth as-grown surfaces on freestanding GaN substrates. *Japanese Journal of Applied Physics*, 56(8):085503, 2017. 12

[107] Kensaku Motoki Kensaku Motoki, Takuji Okahisa Takuji Okahisa, Naoki Matsumoto Naoki Matsumoto, Masato Matsushima Masato Matsushima, Hiroya Kimura Hiroya Kimura, Hitoshi Kasai Hitoshi Kasai, Kikurou Takemoto Kikurou Takemoto, Koji Uematsu Koji Uematsu, Tetsuya Hirano Tetsuya Hirano, Masahiro Nakayama Masahiro Nakayama, et al. Preparation of large freestanding GaN substrates by hydride vapor phase epitaxy using GaAs as a starting substrate. *Japanese Journal of Applied Physics*, 40(2B):L140, 2001. 12

[108] Kazumasa Hiramatsu, Katsuya Nishiyama, Masaru Onishi, Hiromitsu Mizutani, Mitsuhisa Narukawa, Atsushi Motogaito, Hideto Miyake, Yasushi Iyechika, and Takayoshi Maeda. Fabrication and characterization of low defect density GaN using facet-controlled epitaxial lateral overgrowth (FACELO). *Journal of Crystal Growth*, 221(1-4):316–326, 2000. 12, 75

[109] B Beaumont, Ph Vennégués, and P Gibart. Epitaxial lateral overgrowth of GaN. *physica status solidi (b)*, 227(1):1–43, 2001. 12

[110] Johannes Enslin, Arne Knauer, Anna Mogilatenko, Frank Mehnke, Martin Martens, Christian Kuhn, Tim Wernicke, Markus Weyers, and Michael Kneissl. Determination of Sapphire Off-Cut and Its Influence on the Morphology and Local Defect Distribution in Epitaxially Laterally Overgrown AlN for Optically Pumped UVC Lasers. *physica status solidi (a)*, 216(24):1900682, 2019. 12

[111] Gunnar Kusch, Haoning Li, Paul R Edwards, Jochen Bruckbauer, Thomas C Sadler, Peter J Parbrook, and Robert W Martin. Influence of substrate miscut angle on surface morphology and luminescence properties of AlGaN. *Applied Physics Letters*, 104(9):092114, 2014. 12, 41, 62

[112] U Zeimer, V Kueller, A Knauer, A Mogilatenko, M Weyers, and M Kneissl. High quality AlGaN grown on ELO AlN/sapphire templates. *Journal of Crystal Growth*, 377:32–36, 2013. 12, 62

[113] Anna Mogilatenko, Viola Küller, Arne Knauer, J Jeschke, Ute Zeimer, Markus Weyers, and Günther Tränkle. Defect analysis in AlGaN layers on AlN templates obtained by epitaxial lateral overgrowth. *Journal of Crystal Growth*, 402:222–229, 2014. 13

[114] Sylvia Hagedorn, Sebastian Walde, Arne Knauer, Norman Susilo, Daniel Pacak, Leonardo Cancellara, Carsten Netzel, Anna Mogilatenko, Carsten Hartmann, Tim Wernicke, et al. Status and Prospects of AlN Templates on Sapphire for Ultraviolet Light-Emitting Diodes. *physica status solidi (a)*, 217(14):1901022, 2020. 13

[115] Peng Dong, Jianchang Yan, Junxi Wang, Yun Zhang, Chong Geng, Tongbo Wei, Peipei Cong, Yiyun Zhang, Jianping Zeng, Yingdong Tian, et al. 282-nm AlGaN-based deep ultraviolet light-emitting diodes with improved performance on nano-patterned sapphire substrates. *Applied Physics Letters*, 102(24):241113, 2013. 13

[116] Phillip Manley, Sebastian Walde, Sylvia Hagedorn, Martin Hammerschmidt, Sven Burger, and Christiane Becker. Nanopatterned sapphire substrates in deep-UV LEDs: is there an optical benefit? *Optics express*, 28(3):3619–3635, 2020. 13

[117] Daniel Nilsson, Erik Janzén, and Anelia Kakanakova-Georgieva. Lattice parameters of AlN bulk, homoepitaxial and heteroepitaxial material. *Journal of Physics D: Applied Physics*, 49(17):175108, 2016. 13

[118] WM Yim, EJ Stofko, PJ Zanzucchi, JI Pankove, M Ettenberg, and SL Gilbert. Epitaxially grown AlN and its optical band gap. *Journal of Applied Physics*, 44(1):292–296, 1973. 13

[119] M Leszczynski, Ha Teisseyre, T Suski, I Grzegory, M Bockowski, J Jun, S Porowski, K Pakula, JM Baranowski, CT Foxon, et al. Lattice parameters of gallium nitride. *Applied Physics Letters*, 69(1):73–75, 1996. 13

[120] Vanya Darakchieva, Bo Monemar, and A Usui. On the lattice parameters of GaN. *Applied Physics Letters*, 91(3):031911, 2007. 13

[121] Kai Wang and Robert R Reeber. Thermal expansion and elastic properties of InN. *Applied Physics Letters*, 79(11):1602–1604, 2001. 13

[122] Jl Wu, Wladek Walukiewicz, KM Yu, JW Ager Iii, EE Haller, Hai Lu, William J Schaff, Yoshiki Saito, and Yasushi Nanishi. Unusual properties of the fundamental band gap of InN. *Applied Physics Letters*, 80(21):3967–3969, 2002. 13

[123] V Yu Davydov, AA Klochikhin, VV Emtsev, SV Ivanov, VV Vekshin, F Bechstedt, J Furthmüller, H Harima, AV Mudryi, A Hashimoto, et al. Band Gap of InN and In-Rich InxGa1—xN alloys (0.36¡ x¡ 1). *physica status solidi (b)*, 230(2):R4–R6, 2002. 13

[124] Hartwin Peelaers, Joel B Varley, James S Speck, and Chris G Van de Walle. Structural and electronic properties of Ga2O3-Al2O3 alloys. *Applied Physics Letters*, 112(24):242101, 2018. 13

[125] Anthony Aiello, Yuanpeng Wu, Ayush Pandey, Ping Wang, Woncheol Lee, Dylan Bayerl, Nocona Sanders, Zihao Deng, Jiseok Gim, Kai Sun, et al. Deep ultraviolet luminescence due to extreme confinement in monolayer GaN/Al (Ga) N nanowire and planar heterostructures. *Nano letters*, 19(11):7852–7858, 2019. 14

[126] Vincent Grenier, Sylvain Finot, Gwenolé Jacopin, Catherine Bougerol, Eric Robin, Nicolas Mollard, Bruno Gayral, Eva Monroy, Joël Eymery, and Christophe Durand. UV Emission from GaN Wires with m-Plane Core–Shell GaN/AlGaN Multiple Quantum Wells. *ACS Applied Materials & Interfaces*, 12(39):44007–44016, 2020. 14, 44

[127] KP O'Donnell and X Chen. Temperature dependence of semiconductor band gaps. *Applied Physics Letters*, 58(25):2924–2926, 1991. 14

[128] Yong-Hoon Cho, GH Gainer, AJ Fischer, JJ Song, S Keller, UK Mishra, and SP DenBaars. "S-shaped" temperature-dependent emission shift and carrier dynamics in InGaN/GaN multiple quantum wells. *Applied Physics Letters*, 73(10):1370–1372, 1998. 14

[129] Ryan G Banal, Yoshitaka Taniyasu, and Hideki Yamamoto. Deep-ultraviolet light emission properties of nonpolar M-plane AlGaN quantum wells. *Applied Physics Letters*, 105(5):053104, 2014. 14, 37

[130] Thomas Wunderer, Peter Brückner, Joachim Hertkorn, Ferdinand Scholz, Gareth J Beirne, Michael Jetter, Peter Michler, Martin Feneberg, and Klaus Thonke. Time-and locally resolved photoluminescence of semipolar GaInN/GaN facet light emitting diodes. *Applied physics letters*, 90(17):171123, 2007. 14

[131] Min-Ho Kim, Martin F Schubert, Qi Dai, Jong Kyu Kim, E Fred Schubert, Joachim Piprek, and Yongjo Park. Origin of efficiency droop in GaN-based light-emitting diodes. *Applied Physics Letters*, 91(18):183507, 2007. 15

[132] Giovanni Verzellesi, Davide Saguatti, Matteo Meneghini, Francesco Bertazzi, Michele Goano, Gaudenzio Meneghesso, and Enrico Zanoni. Efficiency droop in InGaN/GaN blue light-emitting diodes: Physical mechanisms and remedies. *Journal of Applied Physics*, 114(7):10_1, 2013. 15

[133] M Shahmohammadi, W Liu, G Rossbach, L Lahourcade, A Dussaigne, Catherine Bougerol, R Butté, N Grandjean, B Deveaud, and G Jacopin. Enhancement of Auger recombination induced by carrier localization in InGaN/GaN quantum wells. *Physical Review B*, 95(12):125314, 2017. 15

[134] Zi-Hui Zhang, Sung-Wen Huang Chen, Chunshuang Chu, Kangkai Tian, Mengqian Fang, Yonghui Zhang, Wengang Bi, and Hao-Chung Kuo. Nearly efficiency-droop-free AlGaN-based ultraviolet light-emitting diodes with a specifically designed superlattice p-type electron blocking layer for high mg doping efficiency. *Nanoscale research letters*, 13(1):1–7, 2018. 15

[135] Yun Yan Zhang and Yi An Yin. Performance enhancement of blue light-emitting diodes with a special designed AlGaN/GaN superlattice electron-blocking layer. *Applied physics letters*, 99(22):221103, 2011. 15

[136] Jean-Yves Duboz. GaN/AlGaN superlattices for p contacts in LEDs. *Semiconductor Science and Technology*, 29(3):035017, 2014. 15

[137] Yao Chen, Camille Haller, Wei Liu, Sergey Yu Karpov, Jean-François Carlin, and Nicolas Grandjean. GaN buffer growth temperature and efficiency of InGaN/GaN quantum

wells: The critical role of nitrogen vacancies at the GaN surface. *Applied Physics Letters*, 118(11):111102, 2021. 15

[138] Thomas FK Weatherley, Wei Liu, Vitaly Osokin, Duncan TL Alexander, Robert A Taylor, Jean-Francois Carlin, Raphaël Butté, and Nicolas Grandjean. Imaging Nonradiative Point Defects Buried in Quantum Wells Using Cathodoluminescence. *Nano Letters*, 21(12):5217–5224, 2021. 15, 29

[139] T Fujii, Y Gao, R Sharma, EL Hu, SP DenBaars, and S Nakamura. Increase in the extraction efficiency of GaN-based light-emitting diodes via surface roughening. *Applied Physics Letters*, 84(6):855–857, 2004. 15

[140] Helmholtz and H. Fripp. On the Limits of the Optical Capacity of the Microscope. *The Monthly Microscopical Journal*, 16(1):15–39, 1876. 16

[141] Agnes Bogner, P-H Jouneau, Gilbert Thollet, D Basset, and Catherine Gauthier. A history of scanning electron microscopy developments: Towards "wet-STEM" imaging. *Micron*, 38(4):390–401, 2007. 17, 18

[142] D McMullan. Scanning electron microscopy 1928–1965. *Scanning*, 17(3):175–185, 1995. 17

[143] Manfred von Ardenne. On the history of scanning electron microscopy, of the electron microprobe, and of early contributions to transmission electron microscopy. In *The Beginnings of Electron Microscopy*, volume 16, pages 1–21. Academic Press Orlando, 1985. 17

[144] Thomas E Everhart and RFM Thornley. Wide-band detector for micro-microampere low-energy electron currents. *Journal of scientific instruments*, 37(7):246, 1960. 17, 21

[145] Charles W Oatley. The early history of the scanning electron microscope. *Journal of Applied Physics*, 53(2):R1–R13, 1982. 17

[146] Han Zhang, Jie Tang, Jinshi Yuan, Yasushi Yamauchi, Taku T Suzuki, Norio Shinya, Kiyomi Nakajima, and Lu-Chang Qin. An ultrabright and monochromatic electron point source made of a LaB 6 nanowire. *Nature Nanotechnology*, 11(3):273–279, 2016. 17

[147] Ludwig Reimer. Scanning electron microscopy: physics of image formation and microanalysis, 2000. 18

[148] AV Crewe, DN Eggenberger, J Wall, and LM Welter. Electron gun using a field emission source. *Review of Scientific Instruments*, 39(4):576–583, 1968. 18

[149] C Trager-Cowan, F Sweeney, PW Trimby, AP Day, A Gholinia, N-H Schmidt, PJ Parbrook, Angus J Wilkinson, and IM Watson. Electron backscatter diffraction and electron channeling contrast imaging of tilt and dislocations in nitride thin films. *Physical Review B*, 75(8):085301, 2007. 19

[150] H Fujioka and K Ura. Electron beam blanking systems. *Scanning*, 5(1):3–13, 1983. 20

[151] LJ Brillson. Applications of depth-resolved cathodoluminescence spectroscopy. *Journal of Physics D: Applied Physics*, 45(18):183001, 2012. 20

[152] Wolfgang S.M. Werner, Francesc Salvat-Pujol, Werner Smekal, Rahila Khalid, Friedrich Aumayr, Herbert Störi, Alessandro Ruocco, and Giovanni Stefani. Contribution of surface plasmon decay to secondary electron emission from an Al surface. *Applied Physics Letters*, 99(18):14–17, 2011. 21

[153] H Seiler. Secondary electron emission in the scanning electron microscope. *Journal of Applied Physics*, 54(11):R1–R18, 1983. 21

[154] Kouji Suemori, Yuichi Watanabe, Nobuko Fukuda, and Sei Uemura. Voltage Contrast in Scanning Electron Microscopy to Distinguish Conducting Ag Nanowire Networks from Nonconducting Ag Nanowire Networks. *ACS omega*, 5(22):12692–12697, 2020. 21

[155] Pierre Tchoulfian, Fabrice Donatini, François Levy, Amélie Dussaigne, Pierre Ferret, and Julien Pernot. Direct imaging of p-n junction in core-shell GaN wires. *Nano Letters*, 14(6):3491–3498, 2014. 21

[156] F. Donatini, Andres De Luna Bugallo, Pierre Tchoulfian, Gauthier Chicot, Corinne Sartel, Vincent Sallet, and Julien Pernot. Comparison of Three E-Beam Techniques for Electric Field Imaging and Carrier Diffusion Length Measurement on the Same Nanowires. *Nano Letters*, 16(5):2938–2944, 2016. 21

[157] Jacques Cazaux. Material contrast in SEM: Fermi energy and work function effects. *Ultramicroscopy*, 110(3):242–253, 2010. 21

[158] Patrick Echlin, CE Fiori, Joseph Goldstein, David C Joy, and Dale E Newbury. *Advanced scanning electron microscopy and X-ray microanalysis*. Springer Science & Business Media, 1986. 21

[159] G Naresh-Kumar, A Alasmari, G Kusch, PR Edwards, RW Martin, KP Mingard, and C Trager-Cowan. Metrology of crystal defects through intensity variations in secondary electrons from the diffraction of primary electrons in a scanning electron microscope. *Ultramicroscopy*, 213:112977, 2020. 22

[160] Joanna K Kowalska, Frederico A Lima, Christopher J Pollock, Julian A Rees, and Serena DeBeer. A practical guide to high-resolution x-ray spectroscopic measurements and their applications in bioinorganic chemistry. *Israel Journal of Chemistry*, 56(9-10):803–815, 2016. 22

[161] Henry GJ Moseley. LXXX. The high-frequency spectra of the elements. Part II. *The London, Edinburgh, and Dublin Philosophical Magazine and Journal of Science*, 27(160):703–713, 1914. 22

[162] Günter H Zschornack. *Handbook of X-ray Data*. Springer Science & Business Media, 2007. 22

[163] Oxford Instruments NanoAnalysis. An introduction to energy-dispersive and wavelength-dispersive x-ray microanalysis. *Microscopy and Analysis X-Ray Supplement (Euro)*, 102:S5–S8, 2006. 23

[164] Dale E Newbury and Nicholas WM Ritchie. Is scanning electron microscopy/energy dispersive X-ray spectrometry (SEM/EDS) quantitative? *Scanning*, 35(3):141–168, 2013. 23

[165] Patric Zimmermann, Sergey Peredkov, Paula Macarena Abdala, Serena DeBeer, Moniek Tromp, Christoph Müller, and Jeroen A van Bokhoven. Modern X-ray spectroscopy: XAS and XES in the laboratory. *Coordination Chemistry Reviews*, 423:213466, 2020. 23

[166] Lucia Spasevski, Gunnar Kusch, Pietro Pampili, Vitaly Z. Zubialevich, Duc V. Dinh, Jochen Bruckbauer, Paul R. Edwards, Peter J. Parbrook, and Robert W. Martin. A systematic comparison of polar and semipolar Si-doped AlGaN alloys with high AlN content. *Journal of Physics D: Applied Physics*, 54(3), 2021. 24, 62

[167] Romano Rinaldi and Xavier Llovet. Electron Probe Microanalysis: A Review of the Past, Present, and Future. *Microscopy and Microanalysis*, 21(5):1053–1069, 2015. 24

[168] BG Yacobi and DB Holt. Cathodoluminescence scanning electron microscopy of semiconductors. *Journal of Applied Physics*, 59(4):R1–R24, 1986. 24

[169] T Coenen and NM Haegel. Cathodoluminescence for the 21st century: Learning more from light. *Applied Physics Reviews*, 4(3):031103, 2017. 24

[170] Samuel Wei, Soonhuat Lim, Mohammad Zulkifli, Dnyan Khatri, et al. Optimization and application of Electron Beam Absorbed Current technique. In *2015 IEEE 22nd International Symposium on the Physical and Failure Analysis of Integrated Circuits*, pages 250–254. IEEE, 2015. 24

[171] BH Nall, AN Jette, and CB Bargeron. Diffraction Patterns in the Specimen-Current Image of a Single Crystal at Low Beam Energies. *Physical Review Letters*, 48(13):882, 1982. 24

[172] David Basil Holt and David C Joy. *SEM microcharacterization of semiconductors*. Academic Press, 1989. 25, 64

[173] EI Cole. Resistive contrast imaging applied to multilevel interconnection failure analysis. In *Proceedings., Sixth International IEEE VLSI Multilevel Interconnection Conference*, pages 176–182. IEEE, 1989. 25

[174] DB Holt, B Raza, and A Wojcik. EBIC studies of grain boundaries. *Materials Science and Engineering: B*, 42(1-3):14–23, 1996. 25, 64

[175] Gregory M. Johnson, Baohua Niu, Ted Lundquist, Andreas Rummel, and Matthias Kemmler. Distinguishing between electron-beam signals in probing of SRAM modules for yield management. *Advanced Semiconductor Manufacturing Conference Proceedings*, 2019-May:425–430, 2019. 25

[176] HJ Leamy. Charge collection scanning electron microscopy. *Journal of Applied Physics*, 53(6):R51–R80, 1982. 25

[177] Takeshi Nokuo and Hitoshi Furuya. Fault site localization technique by imaging with nanoprobes. *Electronic Device Failure Analysis*, 11(2):16–22, 2009. 25

[178] C Munakata. Scanning electron micrograph using beta-conductive signal. *Journal of Physics E: Scientific Instruments*, 2(8):738, 1969. 25

[179] Stephan Kleindiek, Klaus Schock, Andreas Rummel, Michael Zschornack, Pascal Limbecker, Andreas Meyer, and Matthias Kemmler. Current imaging, EBIC/EBAC, and electrical probing combined for fast and reliable in situ electrical fault isolation. *Microelectronics Reliability*, 64:313–316, 2016. 26

[180] Carol Trager-Cowan, Aeshah Alasmari, William Avis, Jochen Bruckbauer, Paul R Edwards, Gergely Ferenczi, Benjamin Hourahine, Almpes Kotzai, Simon Kraeusel, Gunnar Kusch, et al. Structural and luminescence imaging and characterisation of semiconductors in the scanning electron microscope. *Semiconductor Science and Technology*, 35(5):054001, 2020. 26

[181] G. Naresh-Kumar, J. Bruckbauer, A. Winkelmann, X. Yu, B. Hourahine, P. R. Edwards, T. Wang, C. Trager-Cowan, and R. W. Martin. Determining GaN Nanowire Polarity and its Influence on Light Emission in the Scanning Electron Microscope. *Nano Letters*, 19(6):3863–3870, 2019. 26, 73, 75, 79

[182] C Trager-Cowan, F Sweeney, Aimo Winkelmann, Angus J Wilkinson, PW Trimby, AP Day, A Gholinia, NH Schmidt, PJ Parbrook, and IM Watson. Characterisation of nitride thin films by electron backscatter diffraction and electron channelling contrast imaging. *Materials Science and Technology*, 22(11):1352–1358, 2006. 26

[183] G. Naresh-Kumar, B. Hourahine, P. R. Edwards, A. P. Day, A. Winkelmann, A. J. Wilkinson, P. J. Parbrook, G. England, and C. Trager-Cowan. Rapid nondestructive analysis of threading dislocations in wurtzite materials using the scanning electron microscope. *Physical Review Letters*, 108:135503, 2012. 26

[184] Marziale Milani, Claudio Savoia, and Davide Bigoni. Electron mirroring: Control of electron transport and understanding of physical processes from sem images. In *Proceedings of*, volume 2, 2009. 27

[185] J-S Kim, Alexei M Tyryshkin, and Stephen A Lyon. face traps in electron-beam irradiated high-mobility metal-oxide-silicon transistors. *Applied Physics Letters*, 110(12):123505, 2017. 27

[186] Dominique Drouin, Alexandre Réal Couture, Dany Joly, Xavier Tastet, Vincent Aimez, and Raynald Gauvin. CASINO V2.42 - A fast and easy-to-use modeling tool for scanning electron microscopy and microanalysis users. *Scanning*, 29(3):92–101, 2007. 29, 52, 53

[187] Hendrix Demers, Nicolas Poirier-Demers, Alexandre Réal Couture, Dany Joly, Marc Guilmain, Niels De Jonge, and Dominique Drouin. Three-dimensional electron microscopy simulation with the CASINO Monte Carlo software. *Scanning*, 33(3):135–146, 2011. 29, 52, 53

[188] Uwe Jahn, Vladimir M Kaganer, Karl K Sabelfeld, Anastasya E Kireeva, Jonas Lähnemann, Carsten Pfüller, Timur Flissikowski, Caroline Chèze, Klaus Biermann, Raffaella Calarco, et al. Carrier Diffusion in GaN: A Cathodoluminescence Study. I. Temperature-Dependent Generation Volume. *Physical Review Applied*, 17(2):024017, 2022. 29

[189] Oliver Brandt, Vladimir M Kaganer, Jonas Lähnemann, Timur Flissikowski, Carsten Pfüller, Karl K Sabelfeld, Anastasya E Kireeva, Caroline Chèze, Raffaella Calarco, Holger T Grahn, et al. Carrier Diffusion in Ga N: A Cathodoluminescence Study. II. Ambipolar versus Exciton Diffusion. *Physical Review Applied*, 17(2):024018, 2022. 29

[190] Jonas Lähnemann, Vladimir M Kaganer, Karl K Sabelfeld, Anastasya E Kireeva, Uwe Jahn, Caroline Chèze, Raffaella Calarco, and Oliver Brandt. Carrier Diffusion in Ga N: A Cathodoluminescence Study. III. Nature of Nonradiative Recombination at Threading Dislocations. *Physical Review Applied*, 17(2):024019, 2022. 29, 59

[191] Hans-Michael Solowan, Julia Danhof, and Ulrich T Schwarz. Direct observation of charge carrier diffusion and localization in an InGaN multi quantum well. *Japanese Journal of Applied Physics*, 52(8S):08JK07, 2013. 29

[192] Paul R Edwards, Lethy Krishnan Jagadamma, Jochen Bruckbauer, Chaowang Liu, Philip Shields, Duncan Allsopp, Tao Wang, and Robert W Martin. High-resolution cathodoluminescence hyperspectral imaging of nitride nanostructures. *Microscopy and Microanalysis*, 18(6):1212–1219, 2012. 30, 42

[193] Paul R Edwards and Robert W Martin. Cathodoluminescence nano-characterization of semiconductors. *Semiconductor Science and Technology*, 26(6):064005, 2011. 30

[194] Paul R Edwards, Robert W Martin, and Martin R Lee. Combined cathodoluminescence hyperspectral imaging and wavelength dispersive X-ray analysis of minerals. *American Mineralogist*, 92(2-3):235–242, 2007. 30

[195] MJ Wallace, PR Edwards, MJ Kappers, MA Hopkins, F Oehler, S Sivaraya, RA Oliver, CJ Humphreys, DWE Allsopp, and RW Martin. Effect of the barrier growth mode on the luminescence and conductivity micron scale uniformity of InGaN light emitting diodes. *Journal of Applied Physics*, 117(11):115705, 2015. 30

[196] Ludwig Reimer. *Transmission electron microscopy: physics of image formation and microanalysis*, volume 36. Springer, 2013. 31

[197] R. Marassi and F. Nobili. MEASUREMENT METHODS — Structural and Chemical Properties: Transmission Electron Microscopy. 2009. 31

[198] RM Langford and C Clinton. In situ lift-out using a FIB-SEM system. *Micron*, 35(7):607–611, 2004. 31

[199] Lucille A Giannuzzi et al. *Introduction to focused ion beams: instrumentation, theory, techniques and practice*. Springer Science & Business Media, 2004. 31

[200] Markku Tilli, Mervi Paulasto-Krockel, Matthias Petzold, Horst Theuss, Teruaki Motooka, and Veikko Lindroos. *Handbook of silicon based MEMS materials and technologies*. Elsevier, 2020. 31

[201] Changhai Ru, Xinyu Liu, and Yu Sun. *Nanopositioning Technologies*. 2016. 32

[202] J. S. Foster, J. E. Frommer, and P. C. Arnett. Molecular manipulation using a tunnelling microscope. *Nature*, 331(6154):324–326, 1988. 32

[203] Eigler DM and Schweizer EK. Positioning single atoms with scanning tunnelling microscope. *Nature*, 344(April):524, 1990. 32

[204] F. Javier Rubio-Sierra, Wolfgang M. Heckl, and Robert W. Stark. Nanomanipulation by atomic force microscopy. *Advanced Engineering Materials*, 7(4):193–196, 2005. 32

[205] Johannes Ledig, Xue Wang, Sönke Fündling, Henning Schuhmann, Michael Seibt, Uwe Jahn, Hergo-Heinrich Wehmann, and Andreas Waag. Characterization of the internal properties of InGaN/GaN core–shell LEDs. *physica status solidi (a)*, 213(1):11–18, 2016. 32

[206] H. Zhang, V. Piazza, V. Neplokh, N. Guan, F. Bayle, S. Collin, L. Largeau, A. Babichev, F. H. Julien, and M. Tchernycheva. Correlated optical and electrical analyses of inhomogeneous core/shell InGaN/GaN nanowire light emitting diodes. *Nanotechnology*, 32(10), 2020. 32

[207] Kazuki Enomoto, Shintaro Kitakata, Toshiyuki Yasuhara, Naoto Ohtake, Toru Kuzumaki, and Yoshitaka Mitsuda. Measurement of Young's modulus of carbon nanotubes by nanoprobe manipulation in a transmission electron microscope. *Applied Physics Letters*, 88(15):1–4, 2006. 32

[208] Aidan P Conlan, Grigore Moldovan, Lucas Bruas, Eva Monroy, and David Cooper. Electron beam induced current microscopy of silicon p–n junctions in a scanning transmission electron microscope. *Journal of Applied Physics*, 129(13):135701, 2021. 32

[209] Hiroshi Amano, Ramón Collazo, Carlo De Santi, Sven Einfeldt, Mitsuru Funato, Johannes Glaab, Sylvia Hagedorn, Akira Hirano, Hideki Hirayama, Ryota Ishii, et al. The 2020 UV emitter roadmap. *Journal of Physics D: Applied Physics*, 53(50):503001, 2020. 36, 57

[210] Hiroko Inagaki, Akatsuki Saito, Hironobu Sugiyama, Tamaki Okabayashi, and Shouichi Fujimoto. Rapid inactivation of SARS-CoV-2 with deep-UV LED irradiation. *Emerging Microbes & Infections*, 9(1):1744–1747, 2020. 36

[211] Johannes Glaab, Neysha Lobo-Ploch, Hyun Kyong Cho, Thomas Filler, Heiko Gundlach, Martin Guttmann, Sylvia Hagedorn, Silke B Lohan, Frank Mehnke, Johannes Schleusener, et al. Skin tolerant inactivation of multiresistant pathogens using far-UVC LEDs. *Scientific reports*, 11(1):1–11, 2021. 36

[212] Kelechi C Anyaogu, Andrey A Ermoshkin, Douglas C Neckers, Alex Mejiritski, Oleg Grinevich, and Andrei V Fedorov. Performance of the light emitting diodes versus conventional light sources in the UV light cured formulations. *Journal of applied polymer science*, 105(2):803–808, 2007. 36

[213] P Waltereit, O Brandt, A Trampert, HT Grahn, J Menniger, M Ramsteiner, M Reiche, and KH Ploog. Nitride semiconductors free of electrostatic fields for efficient white light-emitting diodes. *Nature*, 406(6798):865–868, 2000. 36

[214] Robert Koester, Jun-Seok Hwang, Damien Salomon, Xiaojun Chen, Catherine Bougerol, Jean-Paul Barnes, Daniel Le Si Dang, Lorenzo Rigutti, Andres de Luna Bugallo, Gwénolé Jacopin, et al. M-plane core–shell InGaN/GaN multiple-quantum-wells on GaN wires for electroluminescent devices. *Nano letters*, 11(11):4839–4845, 2011. 36

[215] Fang Qian, Yat Li, Silvija Gradecak, Deli Wang, Carl J Barrelet, and Charles M Lieber. Gallium nitride-based nanowire radial heterostructures for nanophotonics. *Nano letters*, 4(10):1975–1979, 2004. 36

[216] Bilal Janjua, Haiding Sun, Chao Zhao, Dalaver H Anjum, Davide Priante, Abdullah A Alhamoud, Feng Wu, Xiaohang Li, Abdulrahman M Albadri, Ahmed Y Alyamani, et al. Droop-free $\mathrm{Al}_x\mathrm{Ga}_{1-x}\mathrm{N}/\mathrm{Al}_y\mathrm{Ga}_{1-y}\mathrm{N}$ quantum-disks-in-nanowires ultraviolet LED emitting at 337 nm on metal/silicon substrates. *Optics Express*, 25(2):1381–1390, 2017. 36

[217] Xue Wang, Uwe Jahn, Martin Mandl, Tilman Schimpke, Jana Hartmann, Johannes Ledig, Martin Straßburg, Hergo-H Wehmann, and Andreas Waag. Growth and characterization of mixed polar GaN columns and core–shell LEDs. *physica status solidi (a)*, 212(4):727–731, 2015. 36

[218] Christophe Durand, Catherine Bougerol, Jean-François Carlin, Georg Rossbach, Florian Godel, Joël Eymery, Pierre-Henri Jouneau, Anna Mukhtarova, Raphaël Butté, and Nicolas Grandjean. M-Plane GaN/InAlN multiple quantum wells in core–shell wire structure for UV emission. *ACS photonics*, 1(1):38–46, 2014. 36

[219] S Zhao, AT Connie, MHT Dastjerdi, XH Kong, Q Wang, M Djavid, S Sadaf, XD Liu, I Shih, H Guo, et al. Aluminum nitride nanowire light emitting diodes: Breaking the fundamental bottleneck of deep ultraviolet light sources. *Scientific reports*, 5(1):1–5, 2015. 37

[220] Zhihua Fang, Eric Robin, Elena Rozas-Jiménez, Ana Cros, Fabrice Donatini, Nicolas Mollard, Julien Pernot, and Bruno Daudin. Si donor incorporation in GaN nanowires. *Nano letters*, 15(10):6794–6801, 2015. 37

[221] Alexandra-Madalina Siladie, Lynda Amichi, Nicolas Mollard, Isabelle Mouton, Bastien Bonef, Catherine Bougerol, Adeline Grenier, Eric Robin, Pierre-Henri Jouneau, Nuria Garro, et al. Dopant radial inhomogeneity in Mg-doped GaN nanowires. *Nanotechnology*, 29(25):255706, 2018. 37

[222] John E Northrup. Hydrogen and magnesium incorporation on c-plane and m-plane GaN surfaces. *Physical Review B*, 77(4):045313, 2008. 37

[223] Dong Liu, Sang June Cho, Huilong Zhang, Corey R Carlos, Akhil RK Kalapala, Jeongpil Park, Jisoo Kim, Rafael Dalmau, Jiarui Gong, Baxter Moody, et al. Influences of screw dislocations on electroluminescence of AlGaN/AlN-based UVC LEDs. *AIP Advances*, 9(8):085128, 2019. 37, 62, 67

[224] Katsumi Kishino and Shunsuke Ishizawa. Selective-area growth of GaN nanocolumns on Si (111) substrates for application to nanocolumn emitters with systematic analysis of dislocation filtering effect of nanocolumns. *Nanotechnology*, 26(22):225602, 2015. 37

[225] George T Wang, Qiming Li, Jonathan J Wierer, Daniel D Koleske, and Jeffrey J Figiel. Top–down fabrication and characterization of axial and radial III-nitride nanowire LEDs. *physica status solidi (a)*, 211(4):748–751, 2014. 37

[226] Pierre-Marie Coulon, Blandine Alloing, Virginie Brändli, Philippe Vennéguès, Mathieu Leroux, and Jesús Zúñiga-Pérez. Dislocation filtering and polarity in the selective area growth of GaN nanowires by continuous-flow metal organic vapor phase epitaxy. *Applied Physics Express*, 9(1):015502, 2015. 37

[227] Songrui Zhao, Hieu PT Nguyen, Md G Kibria, and Zetian Mi. III-Nitride nanowire optoelectronics. *Progress in Quantum Electronics*, 44:14–68, 2015. 37

[228] Shunfeng Li and Andreas Waag. GaN based nanorods for solid state lighting. *Journal of Applied Physics*, 111(7):5, 2012. 37

[229] W Bergbauer, M Strassburg, Ch Kölper, N Linder, C Roder, J Lähnemann, A Trampert, S Fündling, SF Li, HH Wehmann, et al. Continuous-flux MOVPE growth of position-controlled N-face GaN nanorods and embedded InGaN quantum wells. *Nanotechnology*, 21(30):305201, 2010. 37

[230] Mehrdad Djavid and Zetian Mi. Enhancing the light extraction efficiency of AlGaN deep ultraviolet light emitting diodes by using nanowire structures. *Applied Physics Letters*, 108(5):051102, 2016. 37

[231] Pengwei Du and Zhiyuan Cheng. Enhancing light extraction efficiency of vertical emission of AlGaN nanowire light emitting diodes with photonic crystal. *IEEE Photonics Journal*, 11(3):1–9, 2019. 37

[232] Marcus Müller, Peter Veit, Florian F Krause, Tilman Schimpke, Sebastian Metzner, Frank Bertram, Thorsten Mehrtens, Knut Mül-Caspary, Adrian Avramescu, and Martin Strassburg. Nanoscopic insights into InGaN/GaN core–shell nanorods: structure, composition, and luminescence. 37

[233] M Tchernycheva, P Lavenus, H Zhang, AV Babichev, G Jacopin, M Shahmohammadi, FH Julien, R Ciechonski, G Vescovi, and O Kryliouk. InGaN/GaN core–shell single nanowire light emitting diodes with graphene-based p-contact. *Nano letters*, 14(5):2456–2465, 2014. 37

[234] ED Le Boulbar, Ionut Girgel, CJ Lewins, PR Edwards, RW Martin, A Šatka, DWE Allsopp, and PA Shields. Facet recovery and light emission from GaN/InGaN/GaN core-shell structures grown by metal organic vapour phase epitaxy on etched GaN nanorod arrays. *Journal of Applied Physics*, 114(9):094302, 2013. 37

[235] Pierre-Marie Coulon, Gunnar Kusch, Philip Fletcher, Pierre Chausse, Robert W Martin, and Philip A Shields. Hybrid top-down/bottom-up fabrication of a highly uniform and organized faceted AlN nanorod scaffold. *Materials*, 11(7):1140, 2018. 37, 38

[236] B Neuschl, K Thonke, M Feneberg, R Goldhahn, T Wunderer, Z Yang, NM Johnson, J Xie, S Mita, A Rice, et al. Direct determination of the silicon donor ionization energy in homoepitaxial AlN from photoluminescence two-electron transitions. *Applied Physics Letters*, 103(12):122105, 2013. 37

[237] Q Wang, HPT Nguyen, K Cui, and Z Mi. High efficiency ultraviolet emission from $\mathrm{Al}_x\mathrm{Ga}1-x\mathrm{N}$ core-shell nanowire heterostructures grown on Si (111) by molecular beam epitaxy. *Applied Physics Letters*, 101(4):043115, 2012. 38

[238] Valerio Piazza, Andrey V Babichev, Lorenzo Mancini, Martina Morassi, Patrick Quach, Fabien Bayle, Ludovic Largeau, François H Julien, Pierre Rale, Stéphane Collin, et al. Investigation of GaN nanowires containing AlN/GaN multiple quantum discs by EBIC and CL techniques. *Nanotechnology*, 30(21):214006, 2019. 38

[239] Harun H Solak, Christian Dais, and Francis Clube. Displacement Talbot lithography: a new method for high-resolution patterning of large areas. *Optics express*, 19(11):10686–10691, 2011. 38

[240] PJP Chausse, ED Le Boulbar, SD Lis, and PA Shields. Understanding resolution limit of displacement Talbot lithography. *Optics Express*, 27(5):5918–5930, 2019. 38

[241] Pierre-Marie Coulon, Benjamin Damilano, Blandine Alloing, Pierre Chausse, Sebastian Walde, Johannes Enslin, Robert Armstrong, Stéphane Vézian, Sylvia Hagedorn, Tim Wernicke, et al. Displacement Talbot lithography for nano-engineering of III-nitride materials. *Microsystems & nanoengineering*, 5(1):1–12, 2019. 38

[242] Gordon Schmidt, Marcus Müller, Peter Veit, Sebastian Metzner, Frank Bertram, Jana Hartmann, Hao Zhou, Hergo-Heinrich Wehmann, Andreas Waag, and Jürgen Christen. Direct imaging of Indium-rich triangular nanoprisms self-organized formed at the edges of InGaN/GaN core-shell nanorods. *Scientific reports*, 8(1):1–8, 2018. 41

[243] JT Griffiths, CX Ren, P-M Coulon, ED Le Boulbar, CG Bryce, I Girgel, A Howkins, I Boyd, RW Martin, DWE Allsopp, et al. Structural impact on the nanoscale optical properties of InGaN core-shell nanorods. *Applied Physics Letters*, 110(17):172105, 2017. 41, 44

[244] Luca Francaviglia, Gözde Tütüncüoglu, Sara Martí-Sánchez, Enrico Di Russo, Simon Escobar Steinvall, Jaime Segura Ruiz, Heidi Potts, Martin Friedl, Lorenzo Rigutti, Jordi Arbiol, et al. Segregation scheme of indium in AlGaInAs nanowire shells. *Physical Review Materials*, 3(2):023001, 2019. 41

[245] PF Lu, Chao Sun, HW Cao, Han Ye, XX Zhong, ZY Yu, LH Han, and SM Wang. Strain induced composition profile in InGaN/GaN core–shell nanowires. *Solid state communications*, 178:1–6, 2014. 41

[246] Tim Wernicke, Lukas Schade, Carsten Netzel, Jens Rass, Veit Hoffmann, Simon Ploch, Arne Knauer, Markus Weyers, Ulrich Schwarz, and Michael Kneissl. Indium incorporation and emission wavelength of polar, nonpolar and semipolar InGaN quantum wells. *Semiconductor science and technology*, 27(2):024014, 2012. 41

[247] TY Chang, MA Moram, C McAleese, MJ Kappers, and CJ Humphreys. Inclined dislocation arrays in AlGaN/AlGaN quantum well structures emitting at 290 nm. *Journal of Applied Physics*, 108(12):123522, 2010. 41

[248] Pierre-Marie Coulon, Shahrzad Hosseini Vajargah, An Bao, Paul R Edwards, Emmanuel D Le Boulbar, Ionut Girgel, Robert W Martin, Colin J Humphreys, Rachel A Oliver, Duncan WE Allsopp, et al. Evolution of the m-plane quantum well morphology and composition within a GaN/InGaN core–shell structure. *Crystal Growth & Design*, 17(2):474–482, 2017. 42

[249] Duc V Dinh, Pietro Pampili, and Peter J Parbrook. Silicon doping of semipolar (112^{-} 2) $Al_xGa_{1-x}N(0.50 \leq x \leq 0.55)$. *Journal of Crystal Growth*, 451:181–187, 2016. 43

[250] Martin Feneberg, Fátima Romero, Rüdiger Goldhahn, Tim Wernicke, Christoph Reich, Joachim Stellmach, Frank Mehnke, Arne Knauer, Markus Weyers, and Michael Kneissl. Origin of defect luminescence in ultraviolet emitting AlGaN diode structures. *Applied Physics Letters*, 118(20):202101, 2021. 43, 61

[251] KB Nam, ML Nakarmi, JY Lin, and HX Jiang. Deep impurity transitions involving cation vacancies and complexes in AlGaN alloys. *Applied Physics Letters*, 86(22):222108, 2005. 43

[252] Ionut Gîrgel, Paul R Edwards, Emmanuel Le Boulbar, Pierre-Marie Coulon, Suman Lata Sahonta, Duncan WE Allsopp, Robert W Martin, Colin J Humphreys, and Philip A Shields. Investigation of indium gallium nitride facet-dependent nonpolar growth rates and composition for core–shell light-emitting diodes. *Journal of Nanophotonics*, 10(1):016010, 2016. 44, 61

[253] J Mickevičius, G Tamulaitis, E Kuokštis, K Liu, MS Shur, JP Zhang, and R Gaska. Well-width-dependent carrier lifetime in Al Ga N/ Al Ga N quantum wells. *Applied physics letters*, 90(13):131907, 2007. 45

[254] Jochen Bruckbauer, Paul R Edwards, Jie Bai, Tao Wang, and Robert W Martin. Probing light emission from quantum wells within a single nanorod. *Nanotechnology*, 24(36):365704, 2013. 50

[255] Bradley L Thiel, Milos Toth, and John P Craven. Charging processes in low vacuum scanning electron microscopy. *Microscopy and Microanalysis*, 10(6):711–720, 2004. 51

[256] GD Danilatos. Foundations of environmental scanning electron microscopy. In *Advances in electronics and electron physics*, volume 71, pages 109–250. Elsevier, 1988. 51

[257] Sergi Cuesta, Yoann Curé, Fabrice Donatini, Lou Denaix, Edith Bellet-Amalric, Catherine Bougerol, Vincent Grenier, Quang-Minh Thai, Gilles Nogues, Stephen T Purcell, et al. AlGaN/GaN asymmetric graded-index separate confinement heterostructures designed for electron-beam pumped UV lasers. *Optics Express*, 29(9):13084–13093, 2021. 53

[258] Noritoshi Maeda and Hideki Hirayama. Realization of high-efficiency deep-UV LEDs using transparent p-AlGaN contact layer. *physica status solidi (c)*, 10(11):1521–1524, 2013. 57

[259] Martin Guttmann, Frank Mehnke, Bettina Belde, Fynn Wolf, Christoph Reich, Luca Sulmoni, Tim Wernicke, and Michael Kneissl. Optical light polarization and light extraction efficiency of AlGaN-based LEDs emitting between 264 and 220 nm. *Japanese Journal of Applied Physics*, 58(SC):SCCB20, 2019. 57

[260] Norman Susilo, Sylvia Hagedorn, Dominik Jaeger, Hideto Miyake, Ute Zeimer, Christoph Reich, Bettina Neuschulz, Luca Sulmoni, Martin Guttmann, Frank Mehnke, et al. AlGaN-based deep UV LEDs grown on sputtered and high temperature annealed AlN/sapphire. *Applied Physics Letters*, 112(4):041110, 2018. 57

[261] Norman Susilo, Johannes Enslin, Luca Sulmoni, Martin Guttmann, Ute Zeimer, Tim Wernicke, Markus Weyers, and Michael Kneissl. Effect of the GaN: Mg Contact Layer on the Light-Output and Current-Voltage Characteristic of UVB LEDs. *physica status solidi (a)*, 215(10):1700643, 2018. 58

[262] Johannes Glaab, Joscha Haefke, Jan Ruschel, Moritz Brendel, Jens Rass, Tim Kolbe, Arne Knauer, Markus Weyers, Sven Einfeldt, Martin Guttmann, et al. Degradation effects of the active region in UV-C light-emitting diodes. *Journal of Applied Physics*, 123(10):104502, 2018. 59

[263] Lucia Spasevski, Ben Buse, Paul Edwards, Daniel Hunter, Johannes Enslin, Humberto Foronda, Tim Wernicke, Frank Mehnke, Peter J Parbrook, Michael Kneissl, et al. Quantification of trace-level silicon doping in $\mathrm{Al}_x\mathrm{Ga}1-x\mathrm{N}$ films using wavelength-dispersive X-ray microanalysis. *Microscopy and Microanalysis*, 2021. 59

[264] EB Yakimov. Electron-beam-induced-current study of defects in GaN; experiments and simulation. *Journal of Physics: Condensed Matter*, 14(48):13069, 2002. 59

[265] Gunnar Kusch, M Nouf-Allehiani, Frank Mehnke, Christian Kuhn, Paul R Edwards, Tim Wernicke, Arne Knauer, Viola Kueller, G Naresh-Kumar, Markus Weyers, et al. Spatial clustering of defect luminescence centers in Si-doped low resistivity $\mathrm{Al}_0.82\mathrm{Ga}_0.18\mathrm{N}$. *Applied Physics Letters*, 107(7):072103, 2015. 59

[266] S Mita, R Collazo, A Rice, RF Dalmau, and Z Sitar. Influence of gallium supersaturation on the properties of GaN grown by metalorganic chemical vapor deposition. *Journal of Applied Physics*, 104(1):013521, 2008. 59

[267] B Heying, EJ Tarsa, CR Elsass, P Fini, SP DenBaars, and JS Speck. Dislocation mediated surface morphology of GaN. *Journal of Applied Physics*, 85(9):6470–6476, 1999. 59

[268] Moritz Brendel, Markus Helbling, Andrea Knigge, Frank Brunner, and Markus Weyers. Measurement and simulation of top-and bottom-illuminated solar-blind AlGaN metal-semiconductor-metal photodetectors with high external quantum efficiencies. *Journal of Applied Physics*, 118(24):244504, 2015. 60

[269] V Kueller, A Knauer, F Brunner, U Zeimer, H Rodriguez, M Kneissl, and M Weyers. Growth of AlGaN and AlN on patterned AlN/sapphire templates. *Journal of Crystal Growth*, 315(1):200–203, 2011. 61

[270] Z. G Herro, D Zhuang, R Schlesser, and Z Sitar. Growth of AlN single crystalline boules. *Journal of Crystal Growth*, 312(18):2519–2521, 2010. 61

[271] N Nepal, ML Nakarmi, JY Lin, and HX Jiang. Photoluminescence studies of impurity transitions in AlGaN alloys. *Applied Physics Letters*, 89(9):092107, 2006. 61

[272] Tristan Koppe, Hans Hofsäss, and Ulrich Vetter. Overview of band-edge and defect related luminescence in aluminum nitride. *Journal of Luminescence*, 178:267–281, 2016. 61

[273] Martin Guttmann, Anna Susilo, Luca Sulmoni, Norman Susilo, Eviathar Ziffer, Tim Wernicke, and Michael Kneissl. Light extraction efficiency and internal quantum efficiency of fully UVC-transparent AlGaN based LEDs. *Journal of Physics D: Applied Physics*, 54(33):335101, 2021. 62

[274] 1 SJ Rosner, EC Carr, MJ Ludowise, G Girolami, and HI Erikson. Correlation of cathodoluminescence inhomogeneity with microstructural defects in epitaxial GaN grown by metalorganic chemical-vapor deposition. *Applied Physics Letters*, 70(4):420–422, 1997. 62

[275] Gunnar Kusch, Frank Mehnke, Johannes Enslin, Paul R Edwards, Tim Wernicke, Michael Kneissl, and Robert W Martin. Analysis of doping concentration and composition in wide bandgap AlGaN: Si by wavelength dispersive x-ray spectroscopy. *Semiconductor Science and Technology*, 32(3):035020, 2017. 62

[276] Yoshiki Saito, Satoshi Wada, Kengo Nagata, Hiroaki Makino, Shinya Boyama, Hiroshi Miwa, Shinichi Matsui, Keita Kataoka, Tetsuo Narita, and Kayo Horibuchi. Efficiency improvement of AlGaN-based deep-ultraviolet light-emitting diodes and their virus inactivation application. *Japanese Journal of Applied Physics*, 60(8):080501, 2021. 62

[277] Kenjiro Uesugi, Kanako Shojiki, Yuta Tezen, Yusuke Hayashi, and Hideto Miyake. Suppression of dislocation-induced spiral hillocks in MOVPE-grown AlGaN on face-to-face annealed sputter-deposited AlN template. *Applied Physics Letters*, 116(6):062101, 2020. 62

[278] PS Vergeles and EB Yakimov. EBIC investigation of InGaN/GaN multiple quantum well structures irradiated with low energy electrons. In *Journal of Physics: Conference Series*, volume 281, page 012013. IOP Publishing, 2011. 64

[279] AA Greshnov, AE Chernyakov, BY Ber, DV Davydov, AP Kovarskyi, NM Shmidt, FM Snegov, OA Soltanovich, PS Vergeles, EB Yakimov, et al. Comparative study of quantum efficiency of blue LED with different nanostructural arrangement. *physica status solidi c*, 4(8):2981–2985, 2007. 64

[280] Peter R. Wilshaw. *An SEM EBIC Study of the Electronic Properties of Dislocations in Silicon*. PhD thesis, New College, University of Oxford, 1984. 64

[281] C Youtsey, LT Romano, and I Adesida. Gallium nitride whiskers formed by selective photoenhanced wet etching of dislocations. *Applied Physics Letters*, 73(6):797–799, 1998. 64

[282] Li Chang, SK Lai, FR Chen, and JJ Kai. Observations of Al segregation around dislocations in AlGaN. *Applied Physics Letters*, 79(7):928–930, 2001. 64

[283] JS Speck and SJ Rosner. The role of threading dislocations in the physical properties of GaN and its alloys. *Physica B: Condensed Matter*, 273:24–32, 1999. 64

[284] John E Northrup. Screw dislocations in GaN: The Ga-filled core model. *Applied Physics Letters*, 78(16):2288–2290, 2001. 64

[285] C Lewis Reynolds, Judith G Reynolds, Antonio Crespo, James K Gillespie, Kelson D Chabak, and Robert F Davis. Dislocations as quantum wires: Buffer leakage in AlGaN/GaN heterostructures. *Journal of Materials Research*, 28(13):1687–1691, 2013. 64

[286] Jin Wang, Haifan You, Hui Guo, Junjun Xue, Guofeng Yang, Dunjun Chen, Bin Liu, Hai Lu, Rong Zhang, and Youdou Zheng. Do all screw dislocations cause leakage in GaN-based devices? *Applied Physics Letters*, 116(6):062104, 2020. 64

[287] Santino D Carnevale, Thomas F Kent, Patrick J Phillips, ATMG Sarwar, Camelia Selcu, Robert F Klie, and Roberto C Myers. Mixed polarity in polarization-induced p–n junction nanowire light-emitting diodes. *Nano Letters*, 13(7):3029–3035, 2013. 69

[288] J. K. Hite, N. D. Bassim, M. E. Twigg, M. A. Mastro, F. J. Kub, and C. R. Eddy. GaN vertical and lateral polarity heterostructures on GaN substrates. *Journal of Crystal Growth*, 332(1):43–47, 2011. 69, 70

[289] Dolar Khachariya, Dennis Szymanski, Pramod Reddy, Erhard Kohn, Zlatko Sitar, Ramon Collazo, and Spyridon Pavlidis. A Path Toward Vertical GaN Superjunction Devices. *ECS Transactions*, 98(6):69, 2020. 69

[290] Ramon Collazo, Dennis Szymanski, Dolar Khachariya, Mathew Hayden Breckenridge, Yan Guan, Pegah Bagheri, Pramod Reddy, Ronny Kirste, Seiji Mita, Spyridon Pavlidis, et al. Ion Implantation and Polarity Control: Paths Toward a III-Nitride Superjunction. In *ECS Meeting Abstracts*, number 34, page 983. IOP Publishing, 2021. 69

[291] Jesús Zúñiga-Pérez, Vincent Consonni, Liverios Lymperakis, Xiang Kong, Achim Trampert, Sergio Fernández-Garrido, Oliver Brandt, Hubert Renevier, Stacia Keller, Karine Hestroffer, Markus R. Wagner, Juan Sebastián Reparaz, Fatih Akyol, Siddharth Rajan, Stéphanie Rennesson, Tomás Palacios, and Guy Feuillet. Polarity in GaN and ZnO: Theory, measurement, growth, and devices. *Applied Physics Reviews*, 3(4), 2016. 69, 71

[292] O Ambacher, J Smart, JR Shealy, NG Weimann, K Chu, M Murphy, WJ Schaff, LF Eastman, R Dimitrov, L Wittmer, et al. Two-dimensional electron gases induced by spontaneous and piezoelectric polarization charges in N- And Ga-face AIGaN/GaN heterostructures. *Journal of Applied Physics*, 85(6):3222–3233, 1999. 69

[293] M. Sumiya, K. Yoshimura, K. Ohtsuka, and S. Fuke. Dependence of impurity incorporation on the polar direction of GaN film growth. *Applied Physics Letters*, 76(15):2098–2100, 2000. 69, 74

[294] SR Xu, Y Hao, JC Zhang, YR Cao, XW Zhou, LA Yang, XX Ou, K Chen, and W Mao. Polar dependence of impurity incorporation and yellow luminescence in GaN films grown by metal-organic chemical vapor deposition. *Journal of Crystal Growth*, 312(23):3521–3524, 2010. 69

[295] NA Fichtenbaum, TE Mates, S Keller, SP DenBaars, and UK Mishra. Impurity incorporation in heteroepitaxial N-face and Ga-face GaN films grown by metalorganic chemical vapor deposition. *Journal of Crystal Growth*, 310(6):1124–1131, 2008. 69, 75

[296] Hisashi Masui, Stacia Keller, Natalie Fellows, Nicholas A. Fichtenbaum, Motoko Furukawa, Shuji Nakamura, Umesh K. Mishra, and Steven P. DenBaars. Luminescence characteristics of N-polar GaN and InGaN films grown by metal organic chemical vapor deposition. *Japanese Journal of Applied Physics*, 48(7 PART 1), 2009. 69, 77

[297] Kanako Shojiki, Tomoyuki Tanikawa, Jung-Hun Choi, Shigeyuki Kuboya, Takashi Hanada, Ryuji Katayama, and Takashi Matsuoka. Red to blue wavelength emission of N-polar (0001¯) InGaN light-emitting diodes grown by metalorganic vapor phase epitaxy. *Applied Physics Express*, 8(6), 2015. 69

[298] Stacia Keller, Haoran Li, Matthew Laurent, Yanling Hu, Nathan Pfaff, Jing Lu, David F. Brown, Nicholas A. Fichtenbaum, James S. Speck, Steven P. Denbaars, and Umesh K. Mishra. Recent progress in metal-organic chemical vapor deposition of (0001¯) N-polar group-III nitrides. *Semiconductor Science and Technology*, 29(11), 2014. 69, 70

[299] Alexa Rakoski, Sandra Diez, Haoran Li, Stacia Keller, Elaheh Ahmadi, and Çağllyan Kurdak. Electron transport in N-polar GaN-based heterostructures. *Applied Physics Letters*, 114(16), 2019. 69

[300] Daniel J Denninghoff, Sansaptak Dasgupta, Jing Lu, Stacia Keller, Umesh K Mishra, and Terms Gan. Design of High-Aspect-Ratio T-Gates on N-Polar. 33(6):785–787, 2012. 70

[301] Onur S. Koksaldi, Jeffrey Haller, Haoran Li, Brian Romanczyk, Matthew Guidry, Steven Wienecke, Stacia Keller, and Umesh K. Mishra. N-Polar GaN HEMTs exhibiting record breakdown voltage over 2000 v and Low Dynamic On-Resistance. *IEEE Electron Device Letters*, 39(7):1014–1017, 2018. 70

[302] Siddharth Rajan, Alessandro Chini, Man Hoi Wong, James S. Speck, and Umesh K. Mishra. N-polar GaNAlGaNGaN high electron mobility transistors. *Journal of Applied Physics*, 102(4), 2007. 70

[303] Sansaptak Dasgupta, Nidhi, David F. Brown, Feng Wu, Stacia Keller, James S. Speck, and Umesh K. Mishra. Ultralow nonalloyed Ohmic contact resistance to self aligned N-polar GaN high electron mobility transistors by In(Ga)N regrowth. *Applied Physics Letters*, 96(14), 2010. 70

[304] Uttam Singisetti, Man Hoi Wong, Sansaptak Dasgupta, Nidhi, Brian Swenson, Brian J. Thibeault, James S. Speck, and Umesh K. Mishra. Enhancement-mode n-polar GaN MISFETs with self-aligned source/drain regrowth. *IEEE Electron Device Letters*, 32(2):137–139, 2011. 70

[305] Alexandre Concordel, Gwénolé Jacopin, Bruno Gayral, Núria Garro, Ana Cros, Jean Luc Rouvière, and Bruno Daudin. Polarity conversion of GaN nanowires grown by plasma-assisted molecular beam epitaxy. *Applied Physics Letters*, 114(17), 2019. 70

[306] Man Hoi Wong, Feng Wu, Thomas E. Mates, James S. Speck, and Umesh K. Mishra. Polarity inversion of N-face GaN by plasma-assisted molecular beam epitaxy. *Journal of Applied Physics*, 104(9), 2008. 70

[307] Man Hoi Wong, Feng Wu, James S. Speck, and Umesh K. Mishra. Polarity inversion of N-face GaN using an aluminum oxide interlayer. *Journal of Applied Physics*, 108(12), 2010. 70

[308] V. Ramachandran, R. M. Feenstra, W. L. Sarney, L. Salamanca-Riba, J. E. Northrup, L. T. Romano, and D. W. Greve. Inversion of wurtzite GaN(0001) by exposure to magnesium. *Applied Physics Letters*, 75(6):808–810, 1999. 70

[309] N Grandjean, A Dussaigne, S Pezzagna, and P Vennéguès. Control of the polarity of GaN films using an Mg adsorption layer. *Journal of Crystal Growth*, 251(1):460–464, 2003. 70

[310] John E. Northrup. Magnesium incorporation at (0001) inversion domain boundaries in GaN. *Applied Physics Letters*, 82(14):2278–2280, 2003. 70

[311] K. Xu, N. Yano, A. W. Jia, A. Yoshikawa, and K. Takahashi. Kinetic process of polarity selection in GaN growth by RF-MBE. *Physica Status Solidi (B) Basic Research*, 228(2):523–527, 2001. 70

[312] Masayoshi Adachi, Mari Takasugi, Masashi Sugiyama, Junji Iida, Akikazu Tanaka, and Hiroyuki Fukuyama. Polarity inversion and growth mechanism of AlN layer grown on nitrided sapphire substrate using Ga-Al liquid-phase epitaxy. *Physica Status Solidi (B) Basic Research*, 252(4):743–747, 2015. 70

[313] Stefan Mohn, Natalia Stolyarchuk, Toni Markurt, Ronny Kirste, Marc P. Hoffmann, Ramón Collazo, Aimeric Courville, Rosa Di Felice, Zlatko Sitar, Philippe Vennéguès, and Martin Albrecht. Polarity Control in Group-III Nitrides beyond Pragmatism. *Physical Review Applied*, 5(5):1–9, 2016. 70

[314] Aref Chowdhury, Hock M. Ng, Manish Bhardwaj, and Nils G. Weimann. Second-harmonic generation in periodically poled GaN. *Applied Physics Letters*, 83(6):1077–1079, 2003. 70

[315] M Stutzmann, O Ambacher, M Eickhoff, U Karrer, A Lima Pimenta, R Neuberger, J Schalwig, R Dimitrov, PJ Schuck, and RD Grober. Playing with polarity. *physica status solidi (b)*, 228(2):505–512, 2001. 70, 71

[316] B. J. Rodriguez, W. C. Yang, R. J. Nemanich, and A. Gruverman. Scanning probe investigation of surface charge and surface potential of GaN-based heterostructures. *Applied Physics Letters*, 86(11):1–3, 2005. 70

[317] Fude Liu, Ramon Collazo, Seiji Mita, Zlatko Sitar, Gerd Duscher, and Stephen J. Pennycook. The mechanism for polarity inversion of GaN via a thin AlN layer: Direct experimental evidence. *Applied Physics Letters*, 91(20):203115, 2007. 71

[318] Jinwook W. Chung, Edwin L. Piner, and Tomás Palacios. N-face GaN/AlGaN HEMTs fabricated through layer transfer technology. *IEEE Electron Device Letters*, 30(2):113–116, 2009. 71

[319] Marc De Graef and Michael E McHenry. *Structure of materials: an introduction to crystallography, diffraction and symmetry*. Cambridge University Press, 2012. 71

[320] D. Huang, P. Visconti, K. M. Jones, M. A. Reshchikov, F. Yun, A. A. Baski, T. King, and H. Morkoç. Dependence of GaN polarity on the parameters of the buffer layer grown by molecular beam epitaxy. *Applied Physics Letters*, 78(26):4145–4147, 2001. 72

[321] J. L. Rouviere, J. L. Weyher, M. Seelmann-Eggebert, and S. Porowski. Polarity determination for GaN films grown on (0001) sapphire and high-pressure-grown GaN single crystals. *Applied Physics Letters*, 73(5):668–670, 1998. 72

[322] Hock M. Ng, Nils G. Weimann, and Aref Chowdhury. GaN nanotip pyramids formed by anisotropic etching. *Journal of Applied Physics*, 94(1):650–653, 2003. 72

[323] Yan Gao, Tetsuo Fujii, Rajat Sharma, Kenji Fujito, Steven P. Denbaars, Shuji Nakamura, and Evelyn L. Hu. Roughening hexagonal surface morphology on laser lift-off N-face GaN with simple photo-enhanced chemical wet etching. *Japanese Journal of Applied Physics, Part 2: Letters*, 43(5 A), 2004. 72

[324] B. Daudin, J. L. Rouvière, and M. Arlery. Polarity determination of GaN films by ion channeling and convergent beam electron diffraction. *Applied Physics Letters*, 69(17):2480–2482, 1996. 72

[325] X. Kong, J. Ristić, M. A. Sanchez-Garcia, E. Calleja, and A. Trampert. Polarity determination by electron energy-loss spectroscopy: Application to ultra-small III-nitride semiconductor nanocolumns. *Nanotechnology*, 22(41), 2011. 72

[326] KA Mkhoyan, PE Batson, J Cha, WJ Schaff, and J Silcox. Direct determination of local lattice polarity in crystals. *Science*, 312(5778):1354–1354, 2006. 72

[327] J. D. Wei, S. F. Li, A. Atamuratov, H. H. Wehmann, and A. Waag. Photoassisted Kelvin probe force microscopy at GaN surfaces: The role of polarity. *Applied Physics Letters*, 97(17), 2010. 72

[328] Matt D. Brubaker, Igor Levin, Albert V. Davydov, Devin M. Rourke, Norman A. Sanford, Victor M. Bright, and Kris A. Bertness. Effect of AlN buffer layer properties on the morphology and polarity of GaN nanowires grown by molecular beam epitaxy. *Journal of Applied Physics*, 110(5), 2011. 72

[329] Jacque I Pankove and JA Hutchby. Photoluminescence of ion-implanted GaN. *Journal of Applied Physics*, 47(12):5387–5390, 1976. 73

[330] J. L. Lyons, A. Janotti, and C. G. Van De Walle. Carbon impurities and the yellow luminescence in GaN. *Applied Physics Letters*, 97(15):95–98, 2010. 73

[331] P. M. Coulon, M. Mexis, M. Teisseire, M. Jublot, P. Vennéguès, M. Leroux, and J. Zuniga-Perez. Dual-polarity GaN micropillars grown by metalorganic vapour phase epitaxy: Cross-correlation between structural and optical properties. *Journal of Applied Physics*, 115(15), 2014. 74

[332] Da Chao Du, Jin Cheng Zhang, Xin Xiu Ou, Hao Wang, Ke Chen, Jun Shuai Xue, Sheng Rui Xu, and Yue Hao. Investigation of yellow luminescence intensity of N-polar unintentionally doped GaN. *Chinese Physics B*, 20(3), 2011. 74

[333] Damien Salomon, Agnes Messanvi, Joël Eymery, and Gema Martínez-Criado. Silane-Induced N-Polarity in Wires Probed by a Synchrotron Nanobeam. *Nano Letters*, 17(2):946–952, 2017. 74

[334] Shuti Li, Chunlan Mo, Li Wang, Chuanbing Xiong, Xuexin Peng, Fengyi Jiang, Zhenbo Deng, and Dawei Gong. The influence of si-doping to the growth rate and yellow luminescence of gan grown by mocvd. *Journal of luminescence*, 93(4):321–326, 2001. 74, 75

[335] In-Hwan Lee, In-Hoon Choi, Cheul-Ro Lee, Sung-Jin Son, Jae-Young Leem, and Sam Kyu Noh. Mobility enhancement and yellow luminescence in Si-doped GaN grown by metalorganic chemical vapor deposition technique. *Journal of Crystal Growth*, 182(3-4):314–320, 1997. 74

[336] Tosja K. Zywietz, Jörg Neugebauer, and Matthias Scheffler. The adsorption of oxygen at GaN surfaces. *Applied Physics Letters*, 74(12):1695–1697, 1999. 74

[337] Q. Sun, Y. S. Cho, I. H. Lee, J. Han, B. H. Kong, and H. K. Cho. Nitrogen-polar GaN growth evolution on c-plane sapphire. *Applied Physics Letters*, 93(13):88–91, 2008. 74

[338] Xue Wang, Shunfeng Li, Sönke Fündling, Jiandong Wei, Milena Erenburg, Hergo H. Wehmann, Andreas Waag, Werner Bergbauer, Martin Strassburg, Uwe Jahn, and Henning Riechert. Polarity control in 3D GaN structures grown by selective area MOVPE. *Crystal Growth and Design*, 12(5):2552–2556, 2012. 74

[339] J. L. Lyons, A. Janotti, and C. G. Van De Walle. Effects of carbon on the electrical and optical properties of InN, GaN, and AlN. *Physical Review B - Condensed Matter and Materials Physics*, 89(3):1–8, 2014. 75

[340] D. O. Demchenko, I. C. Diallo, and M. A. Reshchikov. Yellow luminescence of gallium nitride generated by carbon defect complexes. *Physical Review Letters*, 110(8):1–5, 2013. 75

[341] M. A. Reshchikov, J. D. McNamara, H. Helava, A. Usikov, and Yu Makarov. Two yellow luminescence bands in undoped GaN. *Scientific Reports*, 8(1):1–11, 2018. 75

[342] M. A. Reshchikov, M. Vorobiov, D. O. Demchenko, Ozgur, H. Morkoç, A. Lesnik, M. P. Hoffmann, F. Hörich, A. Dadgar, and A. Strittmatter. Two charge states of the C N acceptor in GaN: Evidence from photoluminescence. *Physical Review B*, 98(12):125207, 2018. 75

[343] Ronny Kirste, Ramn Collazo, Gordon Callsen, Markus R. Wagner, Thomas Kure, Juan Sebastian Reparaz, Seji Mita, Jinqiao Xie, Anthony Rice, James Tweedie, Zlatko Sitar, and Axel Hoffmann. Temperature dependent photoluminescence of lateral polarity junctions of metal organic chemical vapor deposition grown GaN. *Journal of Applied Physics*, 110(9), 2011. 75

[344] Sheng Horng Yen, Yen Kuang Kuo, Meng Lun Tsai, and Ta Cheng Hsu. Investigation of violet InGaN laser diodes with normal and reversed polarizations. *Applied Physics Letters*, 91(20), 2007. 75

[345] Varun Thakur, Manoj Kesaria, and S. M. Shivaprasad. Enhanced band edge luminescence from stress and defect free GaN nanowall network morphology. *Solid State Communications*, 171:8–13, 2013. 75

[346] Manoj Kesaria and S. M. Shivaprasad. Nitrogen flux induced GaN nanostructure nucleation at misfit dislocations on Al2O3(0001). *Applied Physics Letters*, 99(14):97–100, 2011. 75

[347] R Collazo, S Mita, A Aleksov, R Schlesser, and Z Sitar. Growth of Ga-and N-polar gallium nitride layers by metalorganic vapor phase epitaxy on sapphire wafers. *Journal of Crystal Growth*, 287(2):586–590, 2006. 78

[348] Digbijoy N Nath, Emre Gür, Steven A Ringel, and Siddharth Rajan. Molecular beam epitaxy of N-polar InGaN. *Applied Physics Letters*, 97(7):071903, 2010. 78

[349] Gerd Binnig and Heinrich Rohrer. Scanning tunneling microscopy—from birth to adolescence. *Reviews of Modern Physics*, 59(3):615, 1987. 82

[350] Allan J Melmed. The art and science and other aspects of making sharp tips. *Journal of Vacuum Science & Technology B: Microelectronics and Nanometer Structures Processing, Measurement, and Phenomena*, 9(2):601–608, 1991. 82

[351] J Lindahl, T Takanen, and L Montelius. Easy and reproducible method for making sharp tips of Pt/Ir. *Journal of Vacuum Science & Technology B: Microelectronics and Nanometer Structures Processing, Measurement, and Phenomena*, 16(6):3077–3081, 1998. 82, 83

[352] JP Song, NH Pryds, K Glejbøl, KA Mørch, AR Thölén, and Lars Nygaard Christensen. A development in the preparation of sharp scanning tunneling microscopy tips. *Review of scientific instruments*, 64(4):900–903, 1993. 83

[353] AH Sørensen, U Hvid, MW Mortensen, and KA Mørch. Preparation of platinum/iridium scanning probe microscopy tips. *Review of scientific instruments*, 70(7):3059–3067, 1999. 83

[354] Dieter K Schroder. *Semiconductor material and device characterization*. John Wiley & Sons, 2015. 84

[355] John Bardeen. Surface states and rectification at a metal semi-conductor contact. *Physical Review*, 71(10):717, 1947. 84

[356] Andrew Collins. *Nanotechnology cookbook: practical, reliable and jargon-free experimental procedures*. Elsevier, 2012. 85, 86, 89

[357] John P Ibe, Paul P Bey Jr, Susan L Brandow, Robert A Brizzolara, Nancy A Burnham, Daniel P DiLella, Kok P Lee, Christie RK Marrian, and Richard J Colton. On the electrochemical etching of tips for scanning tunneling microscopy. *Journal of Vacuum Science & Technology A: Vacuum, Surfaces, and Films*, 8(4):3570–3575, 1990. 85, 86, 87, 88

[358] PJ Bryant, HS Kim, YC Zheng, and R Yang. Technique for shaping scanning tunneling microscope tips. *Review of scientific instruments*, 58(6):1115–1115, 1987. 86

[359] Shanli Qin and Hui Deng. Electrochemical etching of tungsten for fabrication of sub-10-nm tips with a long taper and a large shank. *Nanomanufacturing and Metrology*, 2(4):235–240, 2019. 86

[360] Olivier L Guise, Joachim W Ahner, Moon-Chul Jung, Peter C Goughnour, and John T Yates. Reproducible electrochemical etching of tungsten probe tips. *Nano Letters*, 2(3):191–193, 2002. 86, 88

[361] Wei-Tse Chang, Ing-Shouh Hwang, Mu-Tung Chang, Chung-Yueh Lin, Wei-Hao Hsu, and Jin-Long Hou. Method of electrochemical etching of tungsten tips with controllable profiles. *Review of Scientific Instruments*, 83(8):083704, 2012. 86

[362] Bing-Feng Ju, Yuan-Liu Chen, and Yaozheng Ge. The art of electrochemical etching for preparing tungsten probes with controllable tip profile and characteristic parameters. *Review of Scientific Instruments*, 82(1):013707, 2011. 87

[363] Zeljkovic Lab. *Webpage displaying STM tip production methods*, (accessed March 10, 2022). 88, 89, 123

[364] Lisa A Hockett and Stephen E Creager. A convenient method for removing surface oxides from tungsten STM tips. *Review of scientific instruments*, 64(1):263–264, 1993. 89

[365] Jong Kyu Kim, Seok Woo Nam, Sung Il Cho, Myung S Jhon, Kyung Suk Min, Chan Kyu Kim, Ho Bum Jung, and Geun Young Yeom. Study on the oxidation and reduction of tungsten surface for sub-50 nm patterning process. *Journal of Vacuum Science & Technology A: Vacuum, Surfaces, and Films*, 30(6):061305, 2012. 89

[366] Alenka Vesel, Aleksander Drenik, Rok Zaplotnik, Miran Mozetic, and Marianne Balat-Pichelin. Reduction of thin oxide films on tungsten substrate with highly reactive cold hydrogen plasma. *Surface and Interface Analysis*, 42(6-7):1168–1171, 2010. 89

[367] Magnus W Larsson, L Reine Wallenberg, Ann I Persson, and Lars Samuelson. Probing of individual semiconductor nanowhiskers by TEM-STM. *Microscopy and Microanalysis*, 10(1):41–46, 2004. 89

[368] Jehan Saujauddin, Tim Niemi, Ted Lundquist, Baohua Niu, and Michael Cable. Tungsten Probe Tip Cleaning. *Microscopy and Microanalysis*, 26(S2):2708–2709, 2020. 89

[369] LL Smith, SW King, RJ Nemanich, and RF Davis. Cleaning of GaN surfaces. *Journal of electronic materials*, 25(5):805–810, 1996. 90

[370] Hiroshi Okada, Masatohi Shinohara, Yutaka Kondo, Hiroto Sekiguchi, Keisuke Yamane, and Akihiro Wakahara. Investigation of HCl-based surface treatment for GaN devices. In *AIP Conference Proceedings*, volume 1709, page 020011. AIP Publishing LLC, 2016. 90

[371] SW King, JP Barnak, MD Bremser, KM Tracy, C Ronning, RF Davis, and RJ Nemanich. Cleaning of AlN and GaN surfaces. *Journal of Applied Physics*, 84(9):5248–5260, 1998. 90

[372] Jingxi Sun, KA Rickert, JM Redwing, AB Ellis, FJ Himpsel, and TF Kuech. p-GaN surface treatments for metal contacts. *Applied Physics Letters*, 76(4):415–417, 2000. 90

List of Figures